

**ANALYSIS OF TURBULENCE CHARACTERISTICS IN AN  
AXISYMMETRIC NON-CIRCULAR DUCT WITH VARYING HALF  
ANGLES**

**BY**

HIS THESIS HAS BEEN ACCEPTED FOR  
THE DEGREE OF.....*MSc 1996*.....  
AND A COPY MAY BE PLACED IN THE  
UNIVERSITY LIBRARY.

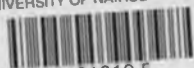
**PERMINUS KARANJA KIBICHO**

A THESIS SUBMITTED IN PARTIAL FULFILLMENT OF THE REQUIREMENTS FOR  
THE AWARD OF THE DEGREE OF MASTER OF SCIENCE IN MECHANICAL  
ENGINEERING OF THE UNIVERSITY OF NAIROBI.

**1996**

**FOR USE IN THE LIBRARY ONLY**

UNIVERSITY OF NAIROBI LIBRARY

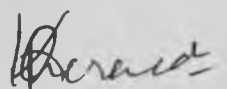


0101619 5

**EAST AFRICANA COLLECTION**

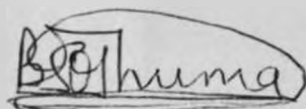
# DECLARATION

I declare that this thesis is my original work. I also affirm that this thesis has not been presented in this or any other university for examination, or for any other purposes.

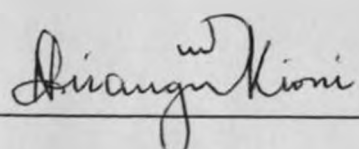
Signed:  \_\_\_\_\_

Perminus Karanja Kibicho

This thesis has been submitted with our authority as the University supervisors.

Signed:  \_\_\_\_\_

Dr. B.H. Ouma

Signed:  \_\_\_\_\_

Dr P.N. Kioni

# Abstract

[Faint, illegible text, likely the abstract content]

Dedicated to my wife, Wangari Karanja and to my father, Wakibicho Njogu.

[Faint, illegible text, likely the main body of the document]

# ABSTRACT

Investigated in this work are the various turbulence characteristics in a non-circular axisymmetric duct of varying half angles.

The turbulence was measured using constant temperature hot-wire anemometry. The voltage signals were linearized through a Kanomax linearizer. The data acquisition was done through an analog to digital converter compatible with the IEEE-488 interface bus which recorded data direct into a NEC personal computer using a software KIBICHO.BAS developed by the author.

Four different half angles were investigated, that is,  $10^{\circ}$ ,  $15^{\circ}$ ,  $17.5^{\circ}$  and  $20^{\circ}$ .

For each half angle, four different planes at distances 0, 100, 200 and 300 mm from the duct's exit plane were investigated. The diverging section of the duct was of length 600 mm. The experimental nodes were in a mesh of 10 x 10 mm.

Preliminary results showed that the turbulence characteristics were independent of the Reynolds number and hence all the experiments were carried out at a constant Reynolds number corresponding to an inverter frequency of 40 Hz. Higher inverter frequencies showed the undesirable effects of vibrations while at low frequencies the turbulence at the test section was not fully developed.

Preliminary data also showed that for angles in excess of  $25^{\circ}$ , separation of the flow occurred at the exit plane and hence the maximum angle for which tests were carried out was  $20^{\circ}$ .

Results indicated that the axial velocity isovels bulged towards the corners which was consistent with the findings of other researchers.

The turbulence intensities increased near the walls and were in the range of between 15% and 45%. They decreased in magnitude further into the duct from the exit plane.

Values of the Reynolds shear stresses varied from 0.01 to 2 N/m<sup>2</sup> while the correlation coefficients had a maximum value of 0.8.

Values of the turbulent kinetic energy varied from 0.2 to 11 m<sup>2</sup>/s<sup>2</sup>. Higher values were always achieved near the walls. Measurements along the centreline revealed that the smallest values of the turbulent kinetic energy occurred at a half angle of 10<sup>0</sup>.

Measurement of the dissipation rate indicated that values increased with increasing traverse distance from the centre and ranged from 0.01 to 0.05 m<sup>2</sup>/s<sup>2</sup> per second.

The Taylor's microscale varied from 0.05mm near the wall to 0.45mm at the centre of the duct.

Other parameters that were measured were the Kolmogoroff's velocity scale whose values were in the range 0.01 to 0.035 mm/s. The lowest values occurred at a half angle of 10<sup>0</sup>.

The Kolmogoroff's time scale gave a maximum value of 0.1 milliseconds.

From the auto-correlation measurements it was observed that the decay times for the axial, horizontal and vertical directions were the same and varied from 18 to 24 milliseconds.

The Eulerian integral time had a constant value of 0.022 seconds.

# ACKNOWLEDGMENT

I wish to acknowledge the help provided by numerous people, in form of material, information, criticism, guidance and encouragement in times of despair.

My most sincere thanks go to my supervisors and academic mentors, Dr. B.H. Ouma and Dr. P.N. Kioni, who besides providing me with guidance without which, I would not have realized my objectives, have also undertaken the difficult task of reading through the whole report, making valuable suggestions and criticisms.

I would also like to thank my sponsors, Japanese International Co-operation Agencies for their continued financial support through Dr. Matsumura, the Japanese Expert, Department of Mechanical Engineering, Jomo Kenyatta University.

Others who made the undertaking of this project successful are: Mr. Owino, welding workshops; Mr. Sitandi, Computer section, Department of Civil Engineering; Mr. Waka, Fluids laboratory, Department of Mechanical Engineering; Mr Tokuda, Computer Science Department; Mr Omondi, drawing office, Department of Mechanical Engineering; (all from Jomo Kenyatta University); and Mr Achapa, Extelcoms, Kenya Posts and Telecommunications.

Special thanks to my wife, Wangari and my sister Wambui for their understanding and encouragement and for making my life tolerable in the house during the entire period of the project.

To all those others, who provided me with any kind of help, I register my deepest gratitude.

# NOMENCLATURE

$a$	Cross-sectional flow area of the test section
$A, B$	King's law constants
$D_h$	Hydraulic diameter
$dP$	Pressure drop along duct's axis
$E_1, E_2$	Anemometer output voltages
$e_1, e_2$	Fluctuating anemometer output voltages
$f$	Friction factor
$k$	Turbulent kinetic energy per unit mass
$L_i$	Eulerian integral length scales
$p$	wetted perimeter
$P$	Static pressure
$P_{atm}$	Atmospheric pressure
$Q$	Total flow rate
$Re$	Reynolds number
$R_i$	Auto-correlation coefficients
$T$	Time
$T_f$	Fluid temperature
$T_{op}$	hot-wire operating temperature
$T_s$	Flow temperature
$U$	Axial velocity
$u$	Axial fluctuating velocity
$U_{bx}$	Bulk velocity

$u_\tau$	Friction velocity
$u^+$	Dimensionless velocity
$V$	Horizontal velocity
$v$	Horizontal fluctuating velocity
$W$	Vertical velocity
$w$	Vertical fluctuating velocity
$y^+$	Dimensionless radial distance from the wall

### Greek symbols

$\alpha$	Separation distance along the axial direction
$\varepsilon$	Dissipation rate
$\eta_k$	Kolmogoroff's length scale
$\lambda$	Taylor's microscale
$\mu$	Dynamic viscosity of air
$\nu$	Kinematic viscosity of air
$\rho$	Density of air
$\tau_k$	Kolmogoroff's time scale
$\tau$	Separation time
$\tau_w$	Wall shear stress
$\vartheta_k$	Kolmogoroff's velocity scale



## Subscripts and superscripts

- ( )<sub>av</sub> Representation of average quantities
- ( )<sup>-</sup> Representation of time averaged values
- ( )' Representation of root mean square values

# CONTENTS

<b>ABSTRACT</b>	<b>i</b>
<b>ACKNOWLEDGMENT</b>	<b>iii</b>
<b>NOMENCLATURE</b>	<b>iv</b>
<b>CONTENTS</b>	<b>vii</b>
<b>LIST OF FIGURES</b>	<b>xi</b>
<b>1. INTRODUCTION</b>	<b>1</b>
<b>2. LITERATURE REVIEW</b>	<b>5</b>
<b>2.1 Introduction</b>	<b>5</b>
<b>2.2 Measurements of turbulence characteristics in rectangular ducts</b>	<b>8</b>
<b>2.3 Measurements of turbulence characteristics in trapezoidal ducts</b>	<b>10</b>
<b>2.4 Measurements of turbulence characteristics in circular axisymmetric diffuser</b>	<b>11</b>
<b>2.5 Measurements by hot-wire anemometer</b>	<b>12</b>
<b>3. THEORETICAL BACKGROUND ON MEASURED PARAMETERS</b>	<b>15</b>
<b>3.1 Hydraulic diameter and bulk quantities</b>	<b>15</b>
<b>3.2 Mean velocity</b>	<b>16</b>
<b>3.3 Velocity field structure</b>	<b>17</b>

3.3.1 Wall region	17
3.3.2 Core region	18
3.4 Turbulence intensity and turbulent kinetic energy	19
3.5 Reynolds shear stresses	20
3.6 Correlation coefficients	22
3.7 Length scales of turbulence	23
3.7.1 Integral length scale	23
3.7.2 The Taylor microscales	24
3.7.3 Local isotropy and Kolmogoroff's hypothesis	26
4. EXPERIMENTAL SET-UP	28
4.1 Existing circular duct	28
4.2 The test flow facility	29
4.2.1 Transition piece	29
4.2.2 Rectangular straight section	30
4.2.3 The test section	30
4.3 Probe traversing mechanism	33
4.4 Hot wire instrumentation	33
4.5 Signal conditioning, discretization and processing	36
5. EXPERIMENTAL PROCEDURE	38
5.1 Mean velocity measurements	38
5.2 Turbulence measurements	39
5.2.1 Calibration of the cross wire	39

5.2.2	Determination of turbulent shear stresses	41
5.3	Computational analysis	42
5.3.1	Mean axial, horizontal and vertical velocities	42
5.3.2	Axial, horizontal and vertical fluctuating velocities	44
5.3.3	The correlation coefficients	44
5.3.4	The turbulent kinetic energy	45
5.3.5	Taylor's microscales	45
5.3.6	The turbulent K.E. dissipation rate and the Kolmogoroff's scales	47
5.3.7	The turbulence intensities	47
5.3.8	The Eulerian integral scales and auto-correlation coefficients	47
5.4	Error analysis for hot wire measurements	48
5.4.1	Temporal resolution	48
5.4.2	Spatial resolution	49
6.	RESULTS AND DISCUSSIONS	50
6.1	Preliminary tests	50
6.2	Velocity measurements	52
6.2.1	Axial mean velocity	52
6.2.2	Secondary flow	54
6.2.3	Turbulence intensities	55
6.3	Reynolds shear stress and correlation coefficients	56
6.4	Turbulent kinetic energy and turbulent kinetic energy dissipation rate.	58
6.5	Scales	59
6.5.1	Taylor's microscales	59
6.5.2	Kolmogoroff's velocity scale	59
6.5.3	Kolmogoroff's time scale	60

<b>6.5.4 Auto-correlation coefficients</b>	<b>60</b>
--	-----------

<b>7. CONCLUSIONS</b>	<b>61</b>
-----------------------	-----------

<b>REFERENCES</b>	<b>119</b>
-------------------	------------

<b>APPENDIX</b>	<b>122</b>
-----------------	------------

# LIST OF FIGURES

<b>Fig. no.</b>	<b>Caption</b>	<b>Page</b>
1.	The flow facility	30
2.	Probe traversing mechanisms	33
3.	Sketch of the cross-wire probe	34
4.	A schematic diagram of the data acquisition and post processing system	36
5.	Test positions and frame of reference	43
6.	Variation of typical atmospheric pressure with time	70
7.	Variation of typical atmospheric temperature with time	70
8.	Inverter calibration curve at the circular duct's exit	71
9.	Inverter calibration curve at the rectangular duct's exit	71
10.	Variation of turbulence intensity with frequency	72
11.	Variation of velocity with time for different inverter frequencies	72
12.	Symmetry test at the circular duct's exit	73
13.	Horizontal symmetry test at the duct's exit for all angles	74
14.	Vertical symmetry at the duct's exit for all angles	75
15.	Mean axial velocity isovel contours for $10^{\circ}$	76
16.	Mean axial velocity isovel contours for $15^{\circ}$	77
17.	Mean axial velocity isovel contours for $17.5^{\circ}$	78
18.	Mean axial velocity isovel contours for $20^{\circ}$	79
19.	Horizontal mean velocity measured along the centreline	80
20.	Horizontal mean velocity measured along a distance 60 mm from the wall	81

21.	Horizontal mean velocity measured along a distance 20 mm from the wall	82
22.	Vertical mean velocity measured along the centreline	83
21.	Vertical mean velocity measured along a distance 60 mm from the wall	84
22.	Vertical mean velocity measured along a distance 20 mm from the wall	85
25.	Axial turbulence intensity measured along the centreline	86
26.	Axial turbulence intensity measured along a distance 60 mm from the wall	87
27.	Axial turbulence intensity measured along a distance 20 mm from the wall	88
28.	Horizontal turbulence intensity measured along the centreline	89
29.	Horizontal turbulence intensity measured along a distance 60 mm from the wall	90
30.	Horizontal turbulence intensity measured along a distance 20 mm from the wall	91
31.	Vertical turbulence intensity measured along the centreline	92
32.	Vertical turbulence intensity measured along a distance 60 mm from the wall	93
33.	Vertical turbulence intensity measured along a distance 20 mm from the wall	94
34.	Reynolds shear stresses $-\overline{\rho uv}$ measured along the centreline	95
35.	Reynolds shear stresses $-\overline{\rho uv}$ measured along a distance 60 mm from the wall	96
36.	Reynolds shear stresses $-\overline{\rho uv}$ measured along a distance 20 mm	

	from the wall	97
37.	Reynolds shear stresses $-\overline{\rho u'w'}$ measured along the centreline	98
38.	Reynolds shear stresses $-\overline{\rho u'w'}$ measured along a distance 60 mm from the wall	99
39.	Reynolds shear stresses $-\overline{\rho u'w'}$ measured along a distance 20 mm from the wall	100
40.	Correlation coefficient $\overline{uv} / u'v'$ measured along the centreline	101
41.	Correlation coefficient $\overline{uv} / u'v'$ measured along a distance 60 mm from the wall	102
42.	Correlation coefficient $\overline{uv} / u'v'$ measured along a distance 20 mm from the wall	103
43.	Correlation coefficient $\overline{uw} / u'w'$ measured along the centreline	104
44.	Correlation coefficient $\overline{uw} / u'w'$ measured along a distance 60 mm from the wall	105
45.	Correlation coefficient $\overline{uw} / u'w'$ measured along a distance 20 mm from the wall	106
46.	Turbulence kinetic energy measured along the centreline	107
47.	Turbulence kinetic energy measured along a distance 60 mm from the wall	108
48.	Turbulence kinetic energy measured along a distance 20 mm from the wall	109
49.	Turbulence kinetic energy dissipation rate measured along the centreline	110



50.	Turbulence kinetic energy dissipation rate measured along a distance 60 mm from the wall	111
51.	Turbulence kinetic energy dissipation rate measured along a distance 20 mm from the wall	112
52.	Taylor's microscale measured along the centreline	113
53.	Taylor's microscale measured along a distance 60 mm from the wall	114
54.	Taylor's microscale measured along a distance 20 mm from the wall	115
55.	Kolmogoroff's velocity scale measured along the centreline	116
56.	Kolmogoroff's velocity scale measured along a distance 60 mm from the wall	117
57.	Kolmogoroff's velocity scale measured along a distance 20 mm from the wall	118
58.	Kolmogoroff's time scale measured along the centreline	119
59.	Kolmogoroff's time scale measured along a distance 60 mm from the wall	120
60.	Kolmogoroff's time scale measured along a distance 20 mm from the wall	121
61.	Auto-correlation coefficients measured on the exit plane at the center position	122
62.	Auto-correlation coefficients measured on the exit plane at the center position, 60 mm from the wall	123
63.	Auto-correlation coefficients measured on the exit plane at the center position, 20 mm from the wall	124

# CHAPTER ONE

## INTRODUCTION

Non-circular conduits (ducts) have many engineering applications. They are mainly used in fluid transportation, for example in airconditioning systems, heat exchangers and others. Prediction and control of flows in these systems is necessary and requires understanding of the three dimensional structure of turbulent flow fields.

In recent years considerable progress has been made in the development of a theory for turbulence. This progress has given a new impetus to both theoretical and experimental investigations.

To solve the problem in the turbulent flow fields, the experimental worker may follow two principal methods of approach to the problem.

The first method of approach is to consider a simple anisotropic turbulent flow field with well-defined boundary conditions and in the light of the existing theories, to try and obtain information on the mechanism of energy transfer from low to the high frequencies on the energy spectrum. Because of the nonisotropic nature of the flow, characteristic quantities such as scale and microscale are no longer well defined and the difficulties of this method are immediately realized.

The second method of approach requires the researcher to establish flow fields which satisfy sufficiently that the flow is isotropic and of high Reynolds number so that the influence of viscosity on the turbulence characteristics is minimum and the effect of turbulence producing mechanism is small. Under these conditions he may measure

quantities such as time averaged turbulence characteristics, correlation functions, scales and microscales that are defined exactly in the flow field and compare his results with those predicted by the theory.

In the present investigation the second method of approach is adopted. There is no doubt that turbulent flow in a duct of non circular cross-section is accompanied by lateral spiral motions. This transverse flow is commonly known as the secondary flow, Brundret and Baines [1964].

Although the magnitude of the secondary flow scarcely amounts to a few percent of bulk flow (typically 1%) and is usually negligible if the motion is induced by a cross-sectional pressure gradient, its presence considerably displaces the lines of constant axial mean velocity (isovels) toward the narrow regions, yielding a comparatively high velocity there.

Prandtl [1927] postulated that the velocity fluctuations tangential to an isovel exceed those perpendicular to it so that a centrifugal acceleration is induced in the region of isovel curvature. Measurements of the secondary flow was therefore necessary but at the time not much effort was directed to its study.

Due to the complex nature of turbulent flows, since an enormous number of degrees of freedom are always excited, it is practically hopeless to attempt to describe the individual particle's time variations in all the generalized coordinates corresponding to the excited degrees of freedom.

The only possibility in the theory of turbulence is a statistical description based on the study of specific statistical laws, inherent in phenomena *en masse*, that is in large ensembles of similar objects.

With the advent of the powerful digital computers, the study of turbulence has been further simplified by the numerical approach. However, since most of these numerical methods, heavily rely on the direct experimental input, it has become impossible to generalize the numerical methods for ducts of arbitrary geometric configurations. Nevertheless, for a particular configuration, a good agreement between the numerical and experimental data needs to be achieved before a generalized modelling technique can be adopted.

The main objectives of the present investigation are to provide direct information about the flow structure of diffuser flows in relation to diffuser half angles and duct's longitudinal axis and to compare the effect of change of the diffuser half angles on the turbulence characteristics.

The experimental work was carried out in three stages. The first stage involved design and fabrication of the flow facility which was required to match the flow conditions and dimensions of an existing circular wind tunnel.

The second stage involved development of a data acquisition software KIBICHO BAS. This program whose listing is given in appendix A was written in BASIC high level language was also used for processing the raw data.

The third stage covered measurements of turbulence parameters. This was done for four duct's half angles. The choice of the angles was arbitrary. A preliminary investigation showed that for the particular dimensions, angles in excess of  $25^{\circ}$  caused separation to occur in the test section and hence the measurements for those angles are not presented. The angles at which measurement were made were  $10^{\circ}$ ,  $15^{\circ}$ ,  $17.5^{\circ}$  and  $20^{\circ}$ . The planes selected for measurements for each half angle were at 0, 100, 200

and 300 mm from the test section's exit plane and an experimental mesh of nodes 10x10 mm was used.

# CHAPTER TWO

## LITERATURE REVIEW

In a turbulent flow within a duct of a non-circular cross-section, a transverse mean flow exists even when the flow is fully developed. This transverse flow, commonly known as the secondary flow brings the fluid into complex lateral spiral motions as superimposed upon the axial mean flow. Thus, the turbulent flow in a non-circular duct is of a three dimensional nature even for the mean flow.

Presented in this chapter are the results and findings of early researches conducted for ducts of various configurations. These are; square and rectangular ducts, trapezoidal ducts and axisymmetric circular diffusers.

### 2.1 Introduction

Reynolds [1883] demonstrated that there are two types of fluid flows. He named the first type, 'laminar flow'. This type of flow is simplified in various flow configurations and is of rare engineering application. The second type he named 'turbulent flow'. Turbulent flows are abundant in engineering applications and provide a complex study.

The principal difficulties in the way of a solution of the problem of turbulent flow arise from the following aspects of its behaviour:

- (a) it has a three dimensional character of the velocity field,
- (b) the equation of motion is non-linear;

(c) it has a random variation of the velocity.

These difficulties occur in an interconnected fashion and are not to be separately overcome. But the history of the research carried out on the problem is largely an account of contributions to each of the three different aspects.

The origin of the subject lies in Taylor's pioneering work in 1935, Brundret and Baines [1964]. Prior to this time, there had been no clear recognition and acceptance of the fact that the velocity of the fluid in turbulent motion is a random continuous function of space and time, and theories of turbulence were based on analogies with the discontinuous collisions between discrete entities that have been studied in the kinetic theory of gases. Taylor broke these primitive concepts and introduced correlation between the velocities at two points as one of the quantities needed to describe the turbulence.

As soon as the statistics of continuous random functions were considered, it became clear that the assumption of statistical homogeneity would greatly simplify the analysis. Taylor went further and considered isotropic turbulence. Thus a clear guide to the opportunities for further theoretical and experimental work was established.

There is ample evidence, Brundret and Baines [1964] that turbulent flow in a non-circular duct is accompanied by lateral spiral motions. This secondary flow convects main flow momentum and energy towards the wall in some regions and away from the wall in other regions.

Nikuradse [1926] discovered that for ducts of non-circular cross-sections, secondary flow actually existed even where the flow was fully developed. He observed that the flows bulged towards the corners of the ducts and away from the

mid-point of the walls. He suggested that these were the result of secondary flows toward the corners which, to satisfy continuity, required a return flow at the mid-point of the walls. It was also postulated that these were the results of turbulent fluctuations along the isovels giving a net flow normal to the isovel wherever a variation in curvature occurred. At that time, measurements of these flows was not easy and his observation was only through visualization.

The observation by Nikuradse sparked off a series of experiments with many researchers trying to provide a description of the nature of the secondary flows.

Speziale et al. [1993] reviewed the prediction of turbulent secondary flows with Reynolds stress models in circular pipes and non-circular ducts. They predicted four fundamental types of secondary flows:

- (1) turbulence-driven secondary flows in straight ducts of non-circular sections.
- (2) turbulent secondary flows in curved circular pipes.
- (3) turbulent secondary flows in curved ducts of non-circular sections.
- (4) turbulent secondary flows in rotating ducts of non-circular sections.



## 2.2 Measurements of turbulence characteristics in rectangular ducts

Hoagland [1960] gave quantitative data of the secondary velocity profile in a square duct. His data in some respects were at variance with the requirements of mass conservation. The difficulty lay in the fact that the secondary velocities were at most a few per cent of the primary velocity (typically 1% of the bulk flow). This meant that any small distortions of the flow pattern caused by the measuring probe could have an appreciable effect on the secondary velocities that were deduced. The accuracy of his data was further diminished by the use of a coarse device for measuring the small angle between the total velocity vector and the duct axis.

Brundret and Baines [1964] gave a fairly detailed description of the secondary flows. They showed that it was gradients in Reynolds shear stresses in the plane of the cross-section that generated streamwise vorticity. They computed all the six components of the Reynolds shear stress and did some investigations on the production and diffusion of vorticity in duct flow. Their only difficulty was how to relate the vorticity  $\Omega_1$  and the secondary flow to the distortion of the main flow. Their data indicated that the basic pattern of secondary flow was independent of Reynolds number, but that with increasing values of Reynolds number the flows penetrated the corners and approached the walls. They also showed that for a rectangular duct, the bisectors separated independent secondary flow circulation zones. Production of vorticity was associated with the region near the bisector. However, there was some evidence that the secondary flow pattern was not so complex as inferred from the distortion of the main longitudinal flow.

Gessner and Jones [1965] conducted similar experiments and reported that the principal axes of Reynolds stress field are not normal or tangent to the isovels. Their measurements indicated, however, that the secondary motion diminished substantially relative to the axial velocity as the Reynolds number was increased by a factor of four. Normalization by the average wall friction velocity substantially diminished the Reynolds number variation

Launder and Ying [1972] conducted an experimental research on turbulence induced secondary flows in a square-sectioned ducts with equally roughened surfaces. The secondary flow was a larger proportion of the axial flow than is the case in smooth-walled ducts. With the secondary velocities normalized by friction velocity, the resultant profiles for smooth and rough surfaces were the same.

Leutheusser [1963] found that in square and rectangular ducts, the inner law (which provides the velocity distribution within the boundary layer) provides a good description of flow in the neighbourhood of the wall but in the centre of the duct the velocity distribution does not follow the outer law formulation. Thus contemporary engineering practice for the prediction of heat transfer and shear distribution in complex-shaped passages was in error because of the assumption of an inner law velocity distribution over the entire cross-section. Even more serious was the neglect of the secondary flows which tended to produce uniform shear and heat transfer around the periphery of the duct.

## 2.3 Measurements of turbulence characteristics in trapezoidal ducts

Rodet [1960] successfully measured the structure of the mean velocity field and the fluctuating velocities in a trapezoidal duct having a mean aspect ratio of 0.82 and corner angles of  $75^\circ$  and  $105^\circ$ . This shape was a small distortion of a square. His results showed that isovels were roughly symmetrical with respect to corner bisectors. Unfortunately his data was in error since the turbulence measurements were made parallel and normal to the top. If all the Reynolds stress tensor components had been measured, the tensor could have been rotated to the coordinate set  $x, y, z$  which would be symmetrical about the bisector.

Prinos et al.[1988] measured turbulence in smooth and rough walled trapezoidal ducts with mean aspect ratio of 3.5 and corner angles of  $64^\circ$  and  $116^\circ$ . Measurements were taken in the fully developed region. They showed the presence of strong secondary currents, which were approximately symmetric about the bisectors of corner angles between two smooth walls as was also found by other investigators of prismatic duct flows. This flow pattern changed dramatically when one wall was roughened and normal stresses doubled while the Reynolds shear stresses tripled by the roughness to the extent that secondary currents in the acute corner between a smooth and a rough wall were strongly suppressed. Their experiments showed that simple gradient transport models for circular pipe flows would be inadequate for modelling of flows in either smooth or partly roughened trapezoidal ducts.

## 2.4 Measurements of turbulence characteristics in circular

### axisymmetric diffuser

In recent years, numerous experimental and theoretical approaches have been developed for turbulence flow in axisymmetric diffusers of circular cross-section.

Weiser et al. [1990] examined the turbulent separated flow passing through a family of axisymmetric diffusers ( $6^\circ \leq \alpha \leq 90^\circ$ ) by experiments as well as numerically. They considered the influence of different boundary conditions such as half angle and Reynolds number on the mean flow field and turbulence structures. Results showed that the mean velocities are described satisfactory by calculations. This applies to the wall friction forces measured by means of a sublayer fence as much as to the pressure distributions. Moreover, it was shown that, when formulating universal flow structures, the reattachment length is of crucial importance.. When accordingly considered, it is possible to represent wall friction and boundary-layer similarity courses in a coherent way independent of diffuser half angles. This similarity behaviour, determined by way of experiment, is also described in a satisfactory way by computation.

Nitsche et al. [1993] conducted an investigation on turbulent transport processes in relaxing diffusers flows. They experimented on turbulent flow quantities such as Reynolds stresses, turbulent kinetic energy, production of turbulence, convection, diffusion and dissipation. They compared their results with the numerical results which had been obtained by employing the standard  $k-\epsilon$  turbulence models and the results agreed well. However, a more detailed analysis of the individual budget terms in the transport equation of turbulent kinetic energy showed some distinct discrepancies

between measurement and computation, mainly in the shear layer downstream of separation region. They also showed, by means of a recently developed probe which, simultaneously senses velocity and pressure fluctuations (X-P probe), that with increasing non-equilibrium of diffuser flows, the pressure diffusion seems to gain importance in the total diffusion term and thus for the turbulence balance in general.

The foregoing literature survey on internal flows indicates lack of both experimental and numerical studies of turbulent flows through axisymmetric diffusers of non-circular cross-section. Even the most basic information such as profiles of mean velocity and turbulence kinetic energy is lacking.

## **2.5 Measurements by hot-wire anemometer**

The hot wire anemometry is one of the most widely used methods of measuring velocities, especially turbulent velocity fluctuations. The hot-wire anemometry relies on the fact that electrical resistance of a metal conductor is a function of its temperature.

The essential part of the hot-wire anemometer, is therefore, a miniature metal element, heated by electrical current and inserted into the flow under investigation. The transfer of heat from the element to the flow increases with increasing velocity in the neighbourhood of the element. The resulting cooling of the element is recorded by a sensitive bridge circuit of which the anemometer forms one of the arms. Preliminary calibration is used to establish the electrical resistance as a function of flow velocity.

There are two types of hot wire anemometry:

- a. constant current anemometry (CCA)
- b. constant temperature anemometry (CTA)

CTA is used in this research. This is because CTA has a high frequency response due to the use of a high gain amplifier in the feedback circuit.

In this type of an anemometer, the resistance is kept constant. This is achieved by using a variable-current feedback loop which ensures that the cooling effect of the flow is compensated and the resistance of the sensitive element remains constant.

The compensating current or voltage is then used as a measure of the flow velocity in the immediate neighbourhood of the sensor.

CTA measures flow velocity through the relationship of the heat transfer rate from a heated wire immersed in the flowing fluid. An expression relating the heat transfer to the fluid velocity and the temperature difference commonly termed as King's law is

$$\frac{Q}{T_{op} - T_f} = A' + B'U^n \quad (2-1)$$

where Q is the heat transfer rate,  $T_{op}$  and  $T_f$  are the operating temperature of the sensor and the fluid temperature respectively, U is the velocity normal to the sensor and A', B' and n are empirical constants.

For a constant  $T_f$ , the King's law can be modified to

$$E^2 = A + BU^n \quad (2-2)$$

where E is the output voltage of a single sensor and U is the perpendicular velocity of the fluid. The constants A, B and n are determined by calibration in a flow of constant temperature  $T_f$ , the temperature and all the transport properties of the calibration fluid should be identical to that of the fluid used in the experiment.

The popularity of the hot wire anemometer is due to the following advantages of such a device

- (i) The sensitive element is small enough not to introduce any disturbance into the flow. The spatial averaging is also minimum,
- (ii) The hot wire anemometer responds almost instantaneously to rapid fluctuations so that high frequency effects can be recorded without distortion,
- (iii) The sensitivity of the hot wire anemometer is high enough for reliable detection of fluctuations amounting to only a few percent of the mean flow velocity,
- (iv) The electrical signal produced by the hot wire anemometer can be readily statistically processed, both by analog and digital systems.

# CHAPTER THREE

## THEORETICAL BACKGROUND ON MEASURED PARAMETERS

Except for the equations of motion and their formal consequences, the theory of turbulence contains many, often crude, approximations. This chapter outlines the mathematical descriptions of the measured turbulence characteristics. Considered are, time averaged mean and fluctuating velocity fields from which parameters like turbulence intensities and turbulent kinetic energy are described. The scales of turbulence, the two-point correlations, Reynolds shear stresses and the auto-correlation coefficients have also been considered.

### 3.1 Hydraulic diameter and bulk quantities

To facilitate simplified study of flow through channels and ducts of non-circular cross-sections, it is common to consider a circular pipe with equivalent flow characteristics. The diameter of such a pipe is called the hydraulic diameter,  $D_h$ . It is usually defined as four times the channels cross-sectional area,  $a$ , divided by its wetted perimeter,  $p$  viz.;

$$D_h = \frac{4a}{p} \quad (3-1)$$

The test section bulk velocity,  $U_{bx}$ , can be defined as

$$U_{bx} = \frac{Q}{a} \quad (3-2)$$



where  $Q$  is the total flow rate through the test section and  $A$  is its cross-sectional area.

For a duct that is not straight 'a' varies along the axis and hence  $U_{bx}$  may only be evaluated for a particular point along the flow axis.  $U_{bx}$  is therefore not constant in the axial direction.

To characterize the flow, the Reynolds number,  $Re_{bx}$ , which is a ratio between the inertial forces and viscous forces is used. It may be obtained as

$$Re_{bt} = \frac{U_{bt} D_h}{\nu} \quad (3-3)$$

where  $\nu$  is the kinematic viscosity of the fluid.

### 3.2 Mean velocity

A statistical mean velocity  $\bar{U}$  in the streamwise direction at any point is defined as the time average of the instantaneous velocity  $U$  at a point. For a stationary turbulent flow

$$\bar{U} = \frac{1}{T} \int_0^T U dt \quad (3-4)$$

where  $T$  is the integral time, which is large enough for the integral to converge.

### 3.3 Velocity field structure

#### 3.3.1 Wall region

Since in this region the local mean velocity depends on local conditions, the distribution may be expressed in its dimensionless form as

$$u^* = f(y^*) \quad (3-5)$$

where

$$u^* = \frac{\bar{U}}{u_\tau} \quad (3-6)$$

$$U_\tau = \sqrt{\frac{\tau_w}{\rho}} \quad (3-7)$$

and 
$$\tau_w = -\mu \left. \frac{\partial \bar{U}}{\partial y} \right|_{y=0} \quad (3-8)$$

where  $\rho$  is the density of the fluid.

and

$$y^* = \frac{u_\tau y}{\nu} \quad (3-9)$$

Equation (3-5) is known as the law of the wall and has been confirmed in many independent experiments.

The wall region is further subdivided into three other subregions, namely; laminar, buffer and inertial sublayers.

In the laminar sublayer viscous shear stresses dominates and  $u^*$  varies linearly with  $y^*$  which extends up to 4, that is,

$$u^* = y^* \quad 0 \leq y^* < 4. \quad (3-10)$$

In the buffer sublayer, the viscous shear stresses are of the same magnitude as the Reynolds stresses with  $y^+$  extending up to 30.

McDGalbraith et al. [1977] postulated that the velocity profile in this region may be approximated by the relation;

$$u^+ = 4.2 - 5.7 \ln y^+ + \frac{5.1}{(\ln y^+)^2} - 0.7(\ln y^+)^3, \quad 4 \leq y^+ < 30 \quad (3-11)$$

The inertial sublayer is dominated by the Reynolds stresses with a logarithmic velocity distribution given as

$$u^+ = A \log_{10} y^+ + B \quad (3-12)$$

Patel [1965] gave the values of A and B as 5.45 and 5.5, respectively.

### 3.3.2 Core region

The velocity distribution depends on the cross-sectional shape of the duct. For a channel, the theoretical analysis is simplified by considering the flow as a turbulent flow between two infinitely long and wide plates, distance  $2h$  apart.

By defining

$$\eta = y/h \quad (3-13)$$

where  $y$  is the distance measured from the wall, then the velocity distribution in the core region is approximated as

$$(U-U_o)/u^+ = F(\eta) \quad (3-14)$$

$U_o$  is the mean velocity at the centre of the channel and  $F$  is some unknown function whose derivative  $\frac{\partial F}{\partial \eta}$  is assumed to be of order one. Equation 3-14 is called the

velocity defect law and is not applicable when  $\eta$  tends to infinity, that is, at the boundary layer.

### 3.4 Turbulence intensity and turbulent kinetic energy

From classical theory, turbulence is defined as an irregular fluid motion in which various quantities (velocity, pressure, concentration, temperature, etc.) show a random variation with time and space coordinates, but in such a way that statistically distinct values can be discerned. Turbulence motion is characterized by the following properties as observed in nature: rotationality, irregularity, three dimensionality, diffusivity, dissipation and high Reynolds number.

Reynolds decomposition procedure provides that on an  $x, y, z$  coordinate system, the velocities can be decomposed as;

$$U = \bar{U} + u, \quad V = \bar{V} + v, \quad \text{and} \quad W = \bar{W} + w \quad (3-15)$$

and

$$\bar{u} = \bar{v} = \bar{w} = 0 \quad (3-16)$$

where overbars denote time averages, lower case letters denote the fluctuating components, and the uppercase letters denote the instantaneous components.

The root mean square values of the velocity fluctuations are defined as

$$u' = \sqrt{\overline{u^2}}, \quad v' = \sqrt{\overline{v^2}} \quad \text{and} \quad w' = \sqrt{\overline{w^2}}. \quad (3-17)$$

In flows with dominant axial velocity  $\bar{U}$ , the local turbulence intensities is given as

$$\frac{\overline{u^2}}{\overline{U}}, \frac{\overline{v^2}}{\overline{U}} \text{ and } \frac{\overline{w^2}}{\overline{U}} \quad (3-18)$$

In the x, y and z directions respectively.

The turbulent kinetic energy per unit mass  $k$  is defined as

$$k = \frac{1}{2}(\overline{u^2} + \overline{v^2} + \overline{w^2}). \quad (3-19)$$

An equation for the total rate of change of kinetic energy (energy budget), Tennekes and Lumley [1972] is given as,

$$\frac{D}{Dt} \left( \frac{1}{2} \overline{u_i u_i} \right) = - \overline{u_i u_j} \frac{\partial \overline{U}_i}{\partial x_j} - \frac{\partial}{\partial x_j} \left[ \overline{u_j \left( \frac{p}{\rho} + \frac{1}{2} u_i u_j \right)} \right] + \overline{\nu u_i \frac{\partial^2 u_j}{\partial x_j \partial x_j}} \quad (3-20)$$

where the total derivative is defined as;

$$\frac{D}{Dt} = \frac{\partial}{\partial t} + U_j \frac{\partial}{\partial x_j} \quad (3-21)$$

The first term of the equation represents the total rate of change of turbulent kinetic energy which is the sum of the temporal and convective rates of change.

The second term which is always positive represents the production of turbulent kinetic energy by the interaction of Reynolds stresses with mean velocity gradients.

The third term represents the work due to pressure fluctuation gradients or alternatively, turbulent diffusion of pressure - velocity correlations.

The last term represents the dissipation (destruction) of turbulent kinetic energy by viscous forces.

### 3.5 Reynolds shear stresses

The contribution of the turbulent motion to the mean stress tensor is facilitated by the Reynolds shear stress.

On a cartesian coordinate system, the Reynolds shear stress tensor is defined as;

$$-\rho \begin{bmatrix} \overline{u^2} & \overline{uv} & \overline{uw} \\ \overline{vu} & \overline{v^2} & \overline{vw} \\ \overline{wu} & \overline{wv} & \overline{w^2} \end{bmatrix} \quad (3-22)$$

Since the Reynolds stress tensor is a symmetric tensor,

$$\overline{uv} = \overline{vu}, \quad \overline{wv} = \overline{vw} \quad \text{and} \quad \overline{uw} = \overline{wu}. \quad (3-23)$$

So that out of the nine components in the Reynolds stress tensor, only six need to be evaluated. The diagonal components are called the normal stresses while the off diagonal components are called shear stresses. The normal stresses contribute little to the transport of momentum while the shear stresses play a dominant role in the theory of mean momentum transfer by turbulent motion.

By looking at the Reynolds momentum equation, Tennekes and Lumley [1972], the total mean stress  $T_{ij}$  is given as;

$$T_{ij} = -P\delta_{ij} + 2\mu S_{ij} - \overline{\rho u_i u_j} \quad (3-24)$$

where the Kronecker delta

$$\delta_{ij} = \begin{cases} 1 & i=j \\ 0 & i \neq j \end{cases}, \quad (3-25)$$

P is the mean pressure

and the strain tensor

$$s_{ij} = \frac{1}{2} \left( \frac{\partial u_i}{\partial x_j} + \frac{\partial u_j}{\partial x_i} \right). \quad (3-26)$$

It can be seen that the term  $-\rho \overline{u_i u_j}$  contribute to the exchange of momentum between the mean and the fluctuating fields.

### 3.6 Correlation coefficients

If we want to describe the evolution of a fluctuating function  $u(t)$ , we need to know how the values of  $u$  at different times are related. This question can be answered by forming a joint density for  $u(t)$  and  $u(t+\tau)$ .

The components of a general two-point correlation tensor in the cartesian coordinate system  $(x_1, x_2, x_3)$  can be defined as

$$R_{ij}(\alpha_1, \alpha_2, \alpha_3, \tau) = \frac{\overline{u_i(x_k; t) u_j(x_k + \alpha_m; t + \tau)}}{\overline{u_i(x_k) u_j(x_k + \alpha_m)}} \quad i, j, k, m = 1, 2, 3. \quad (3-27)$$

Spatial correlations are obtained when  $\tau$  is fixed, temporal correlations when  $\alpha_1, \alpha_2, \alpha_3$  are fixed and space time correlations when  $\tau$  as well as  $\alpha_1, \alpha_2, \alpha_3$  vary.

$R_{ii}$  is called autocorrelation coefficient when  $i=j$  and crosscorrelation when  $i \neq j$

Fixing  $\alpha_1, \alpha_2$  and  $\alpha_3$  we get

$$R_{ij}(\tau) = \frac{\overline{u_i(t) u_j(t + \tau)}}{\overline{u_i u_j}} \quad (3-28)$$

Note that  $u, v$  and  $w$  are equivalent to  $u_1, u_2$  and  $u_3$  respectively.

## 3.7 Length scales of turbulence

Turbulence has different length scales even in the same flow field. These scales could be referred back to either a period or a frequency. Consequently, large eddies have long length scales and time scale (period) and are associated with low frequency whereas small eddies which are associated with high frequency have small length and time scales.

Although no coherent wave pattern exists, measured functions are assumed to be made up of waves of different lengths and periods or frequencies. The spectra are then provided by decompositions of measured random function into its wave components.

The total kinetic energy of the flow is the sum of individual energies of all eddies.

The maximum possible size any eddy can have is determined by the physical dimensions of the duct, while the size of the smallest eddies is determined by the mechanism of dissipation of kinetic energy into heat by molecular motions. There is a continuous transfer of energy between these eddies. The prevailing theory of energy cascades postulates that in a large eddies extract energy from the mean field and transfer it to smaller eddies where it is dissipated into heat.

### 3.7.1 Integral length scale

The characteristic size of the most energetic turbulent eddies is commonly measured by the Eulerian integral length scales, defined as the integrals of corresponding two point spatial correlation coefficient. In flows with a strong axial mean



velocity and relatively low turbulent intensity, it is convenient to define the Eulerian integral time scale as

$$T_y = \int_0^{\infty} R_y(\tau) d\tau \quad (3-29)$$

and by employing the Taylor's 'frozen flow' approximation to determine the Eulerian integral length scales as

$$L_y = \overline{U} T_y \quad (3-30)$$

In practice, integration in equation (3-27) is carried up to the first zero of  $R_y(\tau)$  or to a point where  $R_y(\tau)$  is negligible.

### 3.7.2 The Taylor microscales

The curvature of the two-point correlation coefficient is determined by the small scales of turbulence. The Taylor microscale is a measure of the smallest eddies in which the dissipation of energy into heat occurs.

One can define a characteristic length  $\lambda_u$ , known as the Taylor's microscale, which can be estimated, Hinze [1975], from the variance and spatial derivative of  $u$  as

$$\lambda_u = \left[ \frac{\overline{u^2}}{\left( \frac{\partial u}{\partial x} \right)^2} \right]^{1/2} \quad (3-31)$$

Using Taylor's approximation expressed as

$$\frac{\partial u}{\partial x} = \frac{1}{U} \left( \frac{\partial u}{\partial t} \right) \quad (3-32)$$

the microscales can be estimated as

$$\lambda_u = \bar{U} \left[ \frac{\overline{u^2}}{\left( \frac{\partial u}{\partial t} \right)^2} \right]^{1/2} \quad (3-33)$$

Following a similar procedure, the microscales in y and z directions can be estimated as

$$\lambda_v = \bar{U} \left[ \frac{\overline{v^2}}{\left( \frac{\partial v}{\partial t} \right)^2} \right]^{1/2} \quad (3-34)$$

$$\lambda_w = \bar{U} \left[ \frac{\overline{w^2}}{\left( \frac{\partial w}{\partial t} \right)^2} \right]^{1/2} \quad (3-35)$$

Taylor's microscales are larger than the scales at which the dissipation of kinetic energy into heat mostly occurs. However, they are useful in, among other things, the estimation of the turbulent kinetic energy dissipation rate,  $\epsilon$ , since in isotropic turbulence

$$\epsilon = 15\nu \overline{\left( \frac{\partial u}{\partial x} \right)^2} = 15\nu \frac{\overline{u^2}}{\lambda_u^2} \quad (3-36)$$

### 3.7.3 Local isotropy and Kolmogoroff's hypothesis

The practical application of isotropic turbulence theory, i.e., the assumption that turbulence statistics are independent of the orientation of the coordinate system, appears to be quite limited, since most turbulent flows are not even approximately isotropic.

On the other hand turbulent flows are very diverse and do not permit a single universal description of turbulent phenomena. However, at large enough Reynolds number, the smaller eddies decrease below the critical value and these eddies become stable. At small Reynolds number, viscous forces become dominant and they continuously dissipate kinetic energy into heat. Since small-scale motions tend to have small time scales, one may assume that these motions are statistically independent of the relatively slow large-scale turbulence and of the mean flow. If this assumption makes sense, the small-scale motion should depend only on the rate at which it is supplied with energy by the large-scale motion and on kinematic viscosity. It is reasonable to assume that the rate of energy supply should be equal to the rate of dissipation, because the net rate of change of small-scale energy is related to the time scale of flow as a whole. The net rate of change, therefore, should be small compared to the rate at which energy is dissipated. This is the basis of what is called Kolmogoroff's universal equilibrium theory of the small-scale structure, Tennekes and Lumley [1972].

At large Reynolds number, the characteristic length, velocity and time scales can be uniquely determined by  $\varepsilon$  and  $\nu$ .

By dimensional analysis, these scales can be expressed as;

Kolmogoroff's length scale:  $\eta_k = \left(\frac{\nu^3}{\varepsilon}\right)^{1/4}$

Kolmogoroff's velocity:  $u_k = (\nu\varepsilon)^{1/4}$  (3-37)

Kolmogoroff's time scale:  $\tau_k = \left(\frac{\nu}{\varepsilon}\right)^{1/2}$

The Reynolds number formed with  $\eta$  and  $u$  is equal to one, that is,

$$\eta u / \nu = 1 \quad (3-38)$$

which illustrates that small-scale motion is quite viscous and that the viscous dissipation adjusts itself to the energy supply by adjusting the length scales.

# CHAPTER FOUR

## EXPERIMENTAL SET-UP

This chapter describes the experimental set-up in mainly three sections, namely; the flow facility, the probe traversing mechanism and the data acquisition system. The data acquisition section incorporates the hot-wire instrumentation and the signal conditioning and discretization. The assembly diagram for the flow facility is shown in Figure 1 (a) and (b).

### 4.1 Existing circular duct

The existing wind tunnel, which is made of mild steel, measures 310 mm in diameter and 1940 mm in length. The wind tunnel has an axial fan driven by 1.5 kW induction motor whose speed can be varied through a frequency inverter. Upstream of the fan, there is a mercury-in-glass thermometer for monitoring the temperature of the incoming air. Downstream of the fan a honey comb meant to even out the flow has been fitted. Stainless steel wire meshes of 225 holes per square inch have also been fitted both at the entry and at the exit of the circular duct.

## **4.2 The test flow facility**

The test flow facility is the part which was fitted to the exit of the circular wind tunnel described above so as to achieve the flow conditions required in the experiment. This facility whose design forms part of this work, was fabricated at the Jomo Kenyatta University workshops. The design details are given in Figure 1 (a). The facility consists of three sections: transition piece, rectangular straight section and the test section and are described in detail below.

### **4.2.1 Transition piece**

This is meant to transform the flow cross-section from a circular to a rectangular form. It measures 310 mm in diameter on the circular side and 100 mm by 200 mm on the rectangular side. It was fabricated from 1 mm thick sheet metal.

Both the inlet and the exit to this section are fitted with a stainless steel wire meshes of 225 holes per square inch. Great care was taken during fabrication to make the interior of this section very smooth. Mild steel flanges of 6 mm thickness were used at both ends to enable this section to be bolted to the circular and the rectangular straight section.

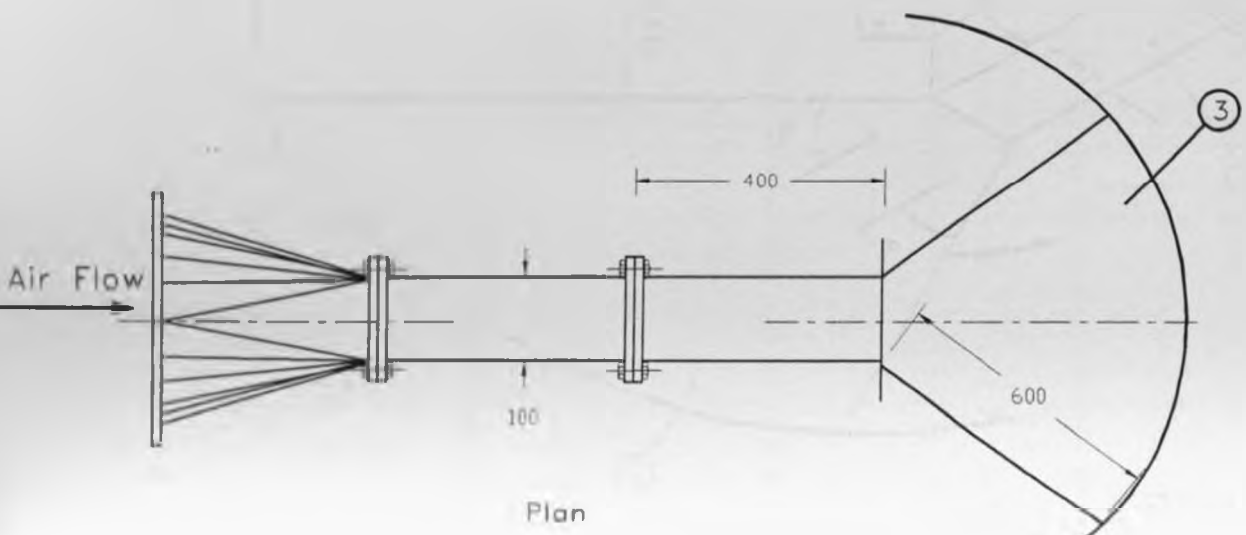
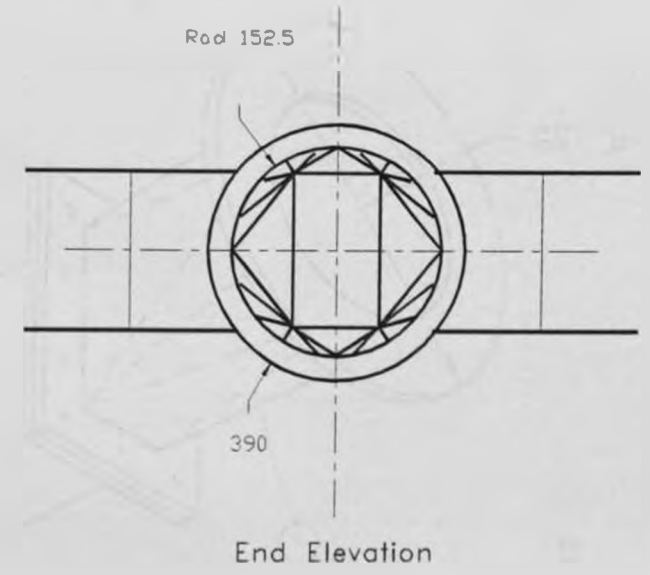
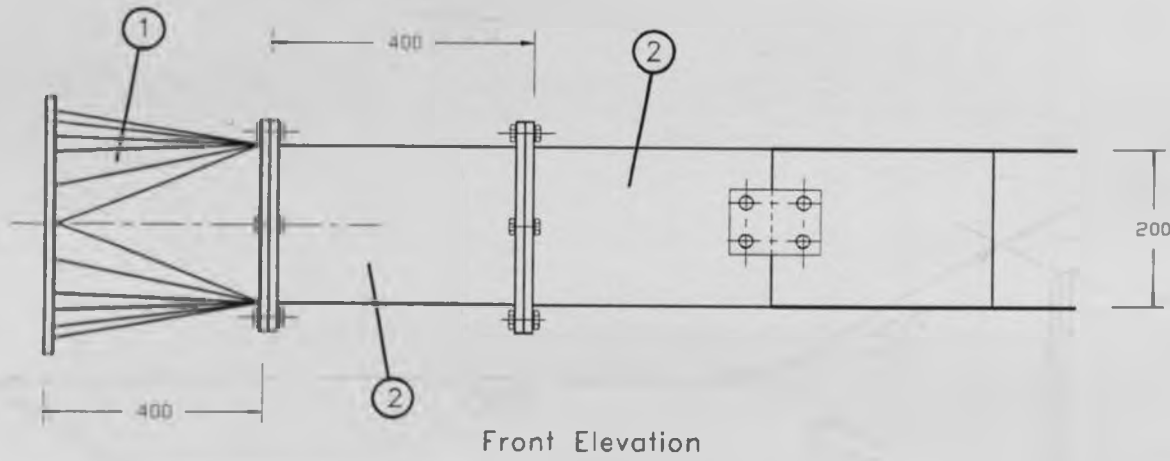
## 4.2.2 Rectangular straight section

This section measures 200x100x800 mm and made from 2 mm and 1.5 mm mild steel plates. It was divided into two sections of lengths 400 mm each to facilitate easy portability and to enable installation of the 225 holes per square inch stainless steel mesh wire. Each section was fitted with flanges, 8 mm thick at both entry and exit ends. During assembly the inlet to the straight section was also fitted with the wire mesh. This section enables the flow to become steady before it is delivered to the test section.

## 4.2.3 The test section

Air was delivered to the test section where the flow cross-section is 200x100 mm. Its length is 600 mm. The side plates were made from 6 mm thick mild steel, while the bottom plate was made from plywood. To allow visibility inside the duct the top plate was made from perspex glass. Pairs of fixed angle plates were fabricated for  $10^{\circ}$ ,  $15^{\circ}$ ,  $17.5^{\circ}$  and  $20^{\circ}$ . Each angle was set and any visible hole or dent was eliminated by use of silicon sealant. All the measurements at a given angle were carried out before the dismantling and set-up for another angle.

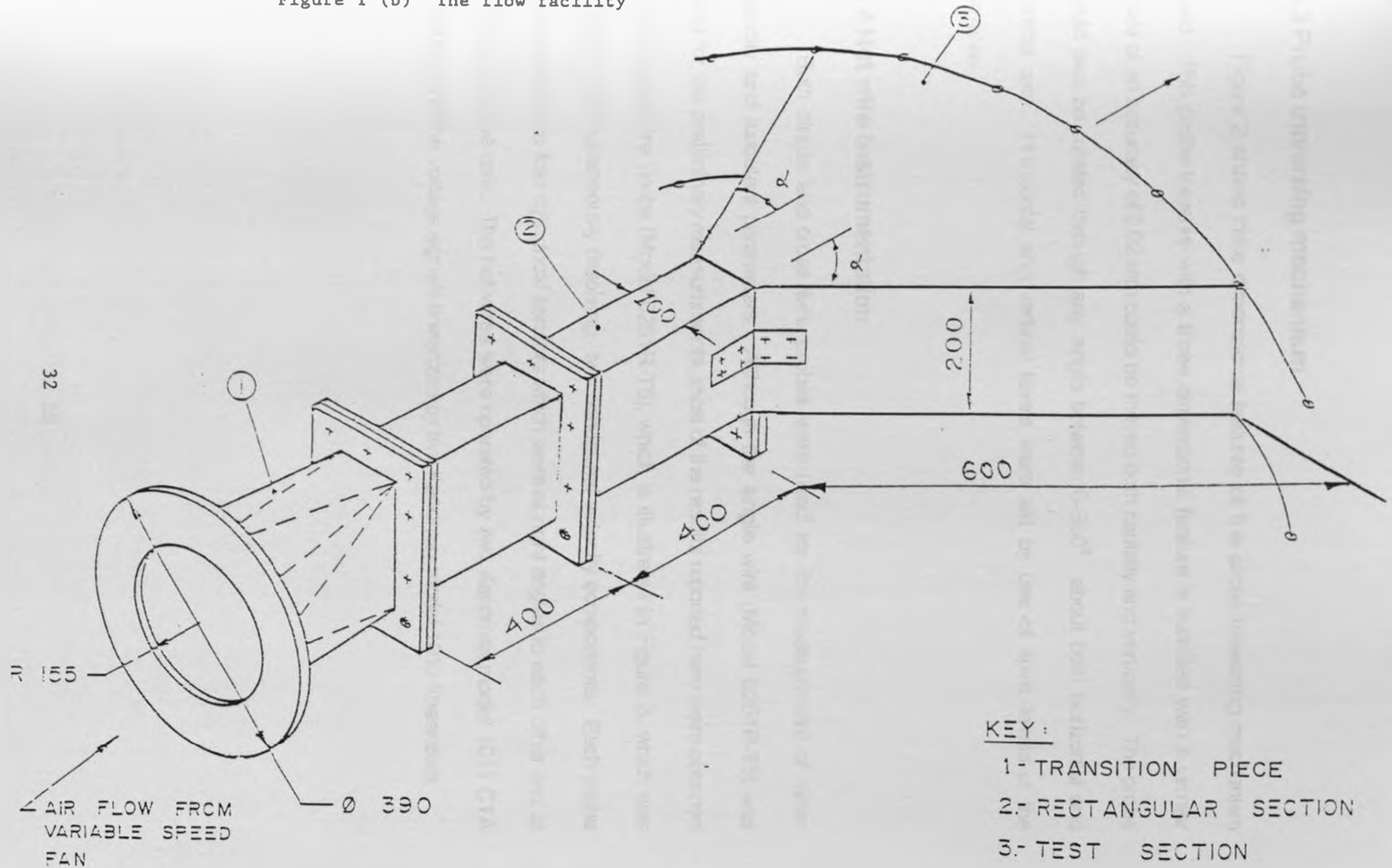
FIGURE 1(a) THE FLOW FACILITY



- Key:
- 1. Transition piece section
  - 2. Rectangular straight section
  - 3. Test section



Figure 1 (b) The flow facility



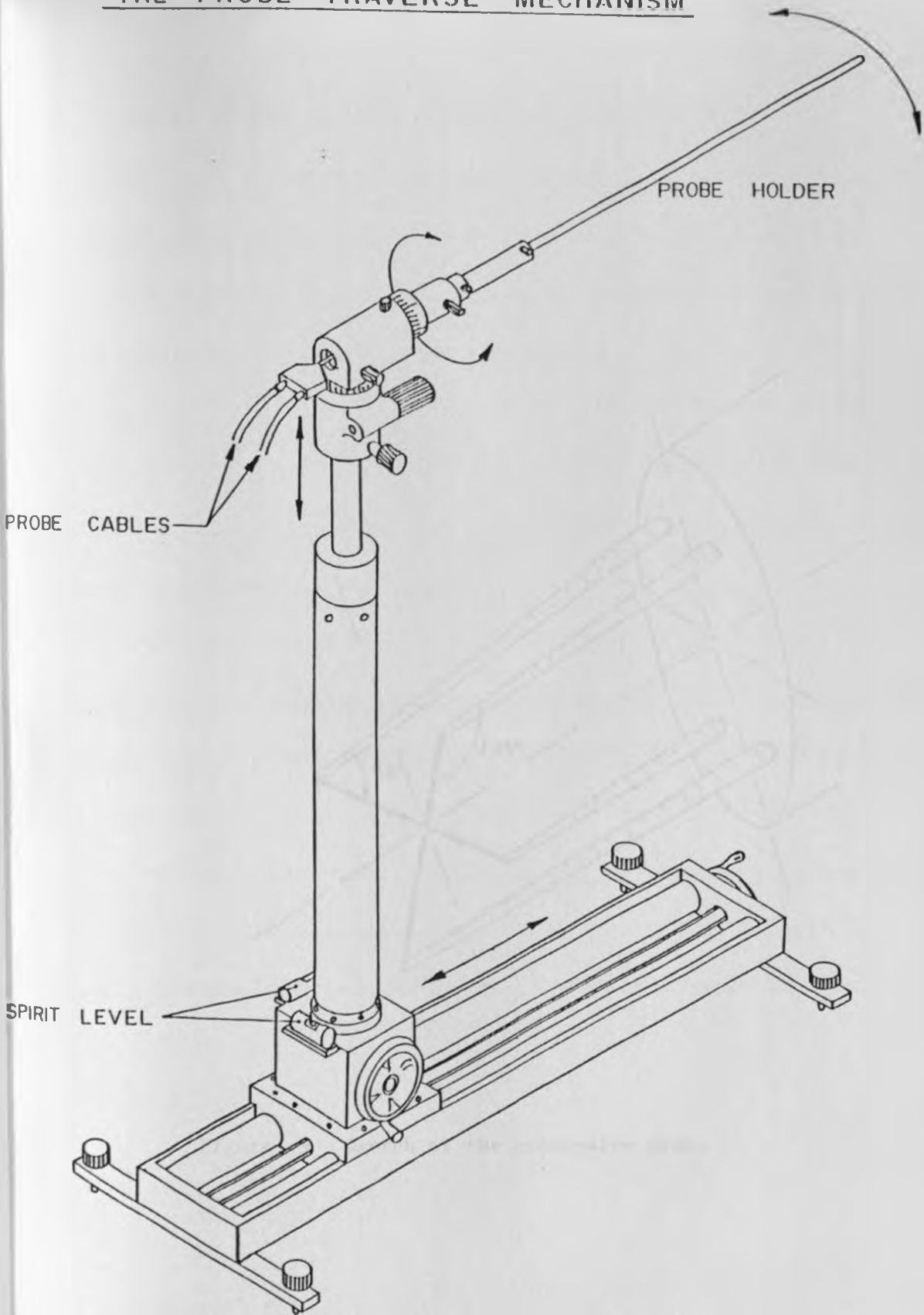
### **4.3 Probe traversing mechanism**

Figure 2 shows three dimensional features of the probe traversing mechanism used. This probe traverse with a three dimensional feature is installed with a vernier scale of an accuracy of 0.02 mm could be moved both radially and vertically. The probe could also be rotated through any angle between 0-360° about both horizontal and vertical axis. Horizontal and vertical levels were set by use of spirit levels of the traverse.

### **4.4 Hot wire instrumentation**

Both single and cross wire probes were used for the measurement of mean velocity and turbulent parameters. Although the single wire (Model 0251R-T5) was used for the preliminary measurements, most of the results reported here were obtained with a cross wire probe (Model 0251R-T5), which is illustrated in Figure 3, which was capable of simultaneously resolving two orthogonal velocity components. Each probe consisted of two thin cylindrical sensors which were at right angles to each other and at 45° to the probe axis. The hot wires were operated by two Kanomax model 1011 CTA modules and the voltage signals linearized by two Kanomax model 1013 linearizers.

# THE PROBE TRAVERSE MECHANISM



NB. ARROWS INDICATE THE DIRECTIONS THAT THE PROBE TRAVERSE MECHANISM CAN MOVE AND ROTATE

Figure 2 The probe traversing mechanism

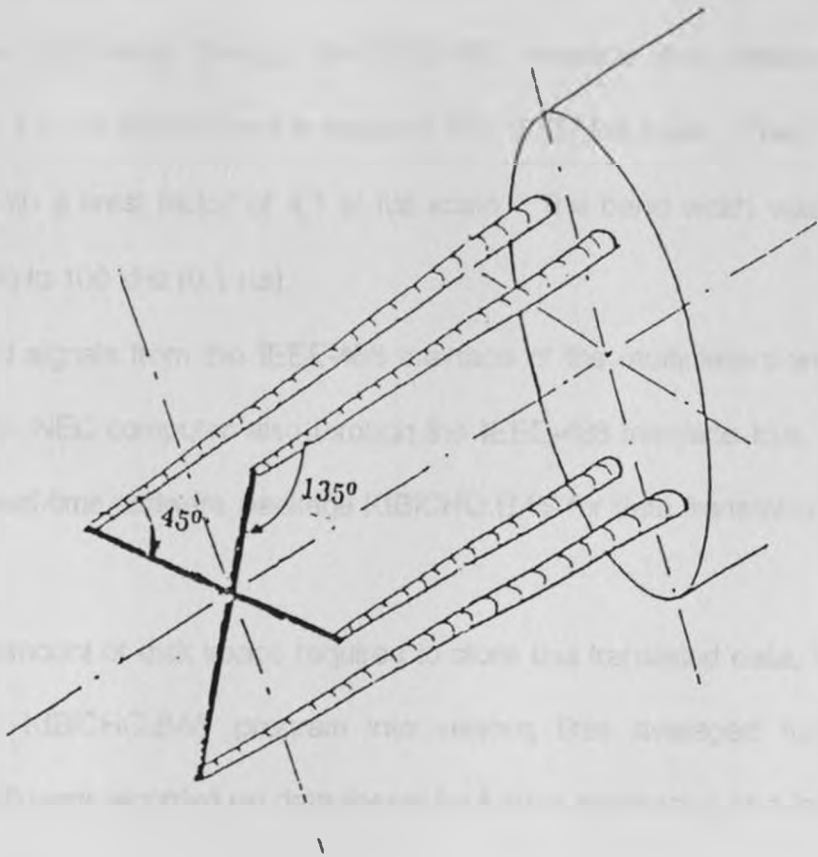


Figure 3 Sketch of the cross-wire probe

#### 4.5 Signal conditioning, discretization and processing

Shown in Figure 4 is a schematic diagram of the data acquisition and post processing system. The anemometer output signals were monitored through a Kenwood model CS-4025 20 MHz oscilloscope. The linearized signals were conditioned by two Hewlett Packard 3478A digital multimeter, with an inbuilt analog to digital (A/D) converter. Thus the outputs of the multimeters through the IEEE-488 interface are digitized. The multimeters have a  $1 \mu\text{V}$  resolution and a range of 0 to 300V full scale. They are true RMS responding with a crest factor of 4:1 at full scale. The band width was in the range 20 Hz (0.05 s) to 100 kHz (0.1  $\mu\text{s}$ ).

The digitized signals from the IEEE-488 interface of the multimeters were then acquired through an NEC computer also through the IEEE-488 interface bus. This is done by use of a real-time software package KIBICHO.BAS for data translations given in appendix A.

Due to the amount of disk space required to store this translated data, the data was computed by KIBICHO.BAS program into various time averaged turbulence characteristics which were recorded on data sheets for further processing at a later time.

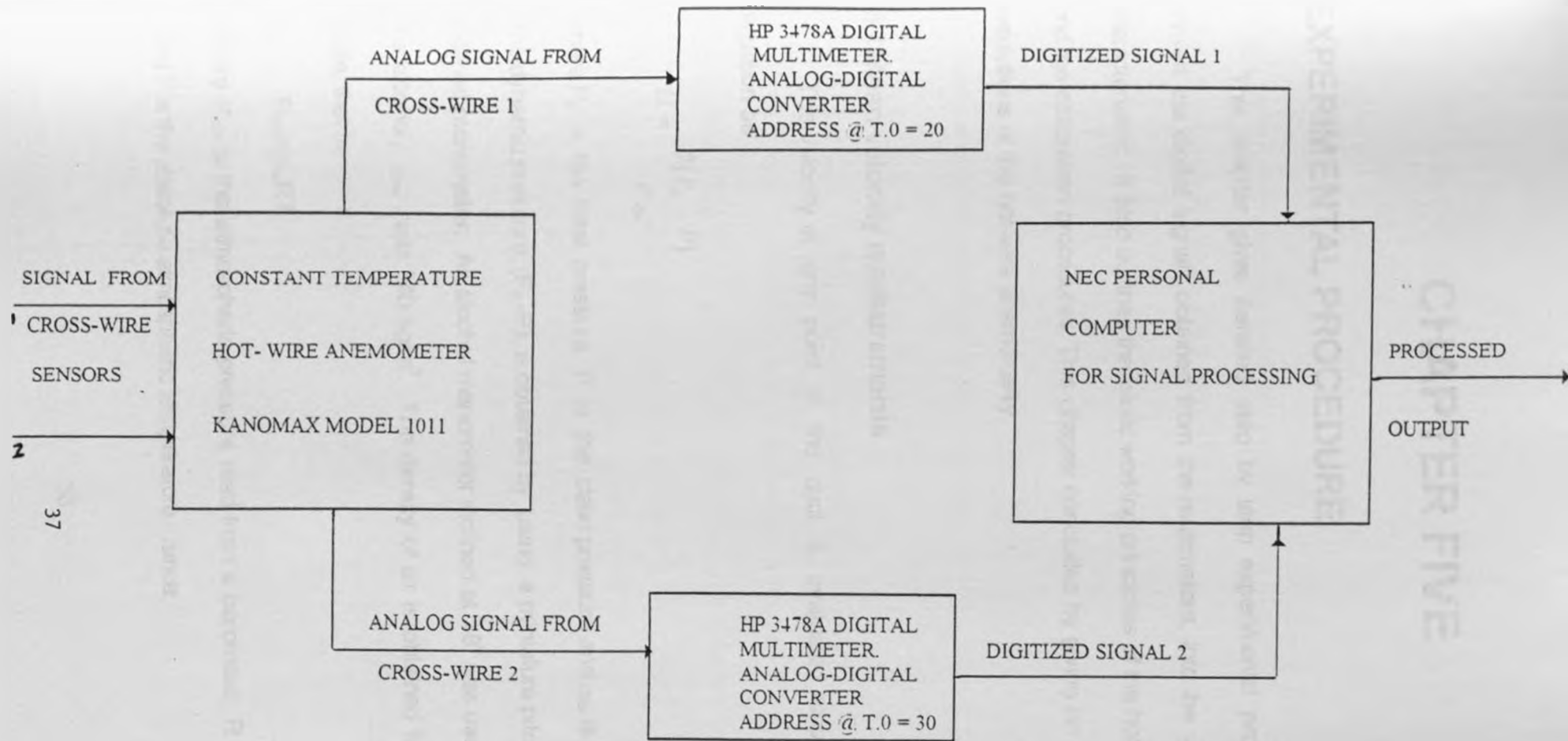


Figure 4 A schematic diagram of the data acquisition and post processing system

# CHAPTER FIVE

## EXPERIMENTAL PROCEDURE

This chapter gives detailed step by step experimental procedures used to convert the digital signals obtained from the multimeters, into the various turbulence characteristics. It also outlines the basic working principles of the hot-wire anemometer and the calibration procedures. This chapter concludes by giving an error analysis and resolutions of the hot-wire anemometry.

### 5.1 Mean velocity measurements

The velocity at any point in the duct is evaluated according to Bernoulli's equation as

$$U = \frac{2(P_0 - P)}{\rho_{Air}} \quad (5-1)$$

where  $P_0$  is the total pressure,  $P$  is the static pressure and  $\rho_{Air}$  is the density of air.

The dynamic pressure,  $(P_0 - P)$ , is obtained by using a miniature pitot static tube and an inclined manometer. An alcohol manometer inclined at  $18^\circ$  was used. The density of the alcohol,  $\rho_{Alc}$  was  $740 \text{ kg/m}^3$ . The density of air is obtained from the equation of state, that is,

$$P_{atm} = \rho_{Air} RT, \quad (5-2)$$

where  $P_{atm}$  is the atmospheric pressure read from a barometer,  $R$  is the gas constant and  $T$  is the absolute atmospheric temperature. Since,

$$P_o - P = \rho_{Alc}gh \quad (5-3)$$

and

$$h = l \sin \theta \quad (5-4)$$

where  $l$  is the manometer reading and  $\theta$  is the angle of inclination

Combining equations 5-1 to 5-4 one obtains

$$U = \sqrt{\frac{2\rho_{Alc}g l R T \sin \theta}{P_{Atm}}} \quad (5-5)$$

## 5.2 Turbulence measurements

### 5.2.1 Calibration of the cross wire

The electric signal obtained in the CTA is theoretically a non-linear function of the flow velocity. A variable exponent type linearizer is used to linearize this signal.

The equation of the signal from the CTA, obtained from the King's law is

$$V_o^2 = (A + BU^{1/m})(T - T_a) \quad (5-6)$$

where

$V_o$  is the output voltage,

$U$  is the flow velocity,

$T$  is the temperature of the sensor,

$T_a$  is the flow temperature, and

$A, B$  are empirical constants.

From equation 5-6, if

$$\frac{V_o^2}{T - T_a} = E_1 \quad (5-7)$$



then equation 5-6 simplifies to

$$E_{lin} = (E_1 - a)^m G = \alpha U \quad (5-8)$$

where

$E_{lin}$  is the output of the linearizer. Therefore the linearizer provides the output directly proportional to the velocity on the basis of equation 5-8.

For the cross wire sensor, each sensor is separately calibrated against a pitot-static tube in a uniform flow produced by a calibration jet. The conversion of the voltages to velocity for the cross wire probe, with two mutually perpendicular sensors set at  $\pm 45^\circ$  to the main flow (Figure 3) is based on the following analysis.

Neglecting convection parallel to the sensors, the effective cooling velocities, that is, the equivalent velocities normal to the two sensors that would produce the same cooling, can be written as

$$U_{eff1} = (U+V)\cos 45^\circ, \quad (5-9)$$

$$U_{eff2} = (U-V)\cos 45^\circ, \quad (5-10)$$

where  $U$  is the instantaneous velocity component of the streamwise direction and  $V$  is the instantaneous transverse velocity component.

The linearizer output  $E_1$  and  $E_2$  are

$$E_1 = k(U+V) \quad (5-11)$$

$$E_2 = k(U-V) \quad (5-12)$$

where  $k$  is a constant determined from the calibration curve (that is  $dE/dU$ ).

$k$  should be the same for both sensors. From equation 5-11 and 5-12

$$U = 1/2k(E_1 + E_2) \quad (5-13)$$

$$V = 1/2k(E_1 - E_2) \quad (5-14)$$

The other velocity component  $W$  is obtained by using equation 5-14 when the probe is rotated through  $90^\circ$ .

## 5.2.2 Determination of turbulent shear stresses

By definition  $U = \bar{U} + u$ ,

$$V = \bar{V} + v \quad \text{and} \quad (5-15)$$

$$W = \bar{W} + w$$

From equations 5-13 and 5-14

$$\bar{U} + u = \frac{1}{2k} (\bar{E}_1 + \bar{E}_2 + e_1 + e_2), \quad (5-16)$$

$$\bar{V} + v = \frac{1}{2k} (\bar{E}_1 - \bar{E}_2 + e_1 - e_2), \quad \text{and} \quad (5-17) \text{ (a)}$$

$$\bar{W} + w = \frac{1}{2k} (\bar{E}_1 - \bar{E}_2 + e_1 - e_2). \quad (5-17) \text{ (b)}$$

Equation 5-17 (a) gives a corresponding expression, equation 5-17 (b) in z-direction when the probe is rotated through  $90^\circ$ .

From equations 5-16 and 5-17 (a) and (b) one obtains

$$\overline{uv} = \left(\frac{1}{2k}\right)^2 \overline{(e_1^2 - e_2^2)} = \left(\frac{1}{2k}\right)^2 (\overline{e_1^2} - \overline{e_2^2}), \quad \text{and} \quad (5-18)$$

$$\overline{vw} = \left(\frac{1}{2k}\right)^2 \overline{(e_1^2 - e_2^2)} = \left(\frac{1}{2k}\right)^2 (\overline{e_1^2} - \overline{e_2^2}). \quad (5-19)$$

## 5.3 Computational analysis

Figure 5 gives the tests positions and the frame of reference adopted in the presentation of the results.

### 5.3.1 Mean axial, horizontal and vertical velocities

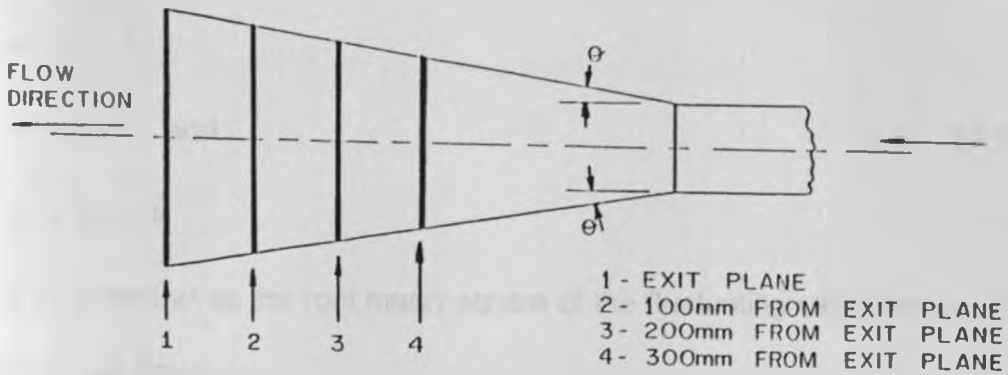
To obtain the mean velocities in axial horizontal and vertical directions, expressions 5-20, 5-21 and 5-22 given below were used. The higher the value of  $x$  the better was the approximation. The value of  $x$  used during the experiments was 5000.

$$\bar{U} = \left( \sum_{i=1}^x U_i \right) / x \quad (5-20)$$

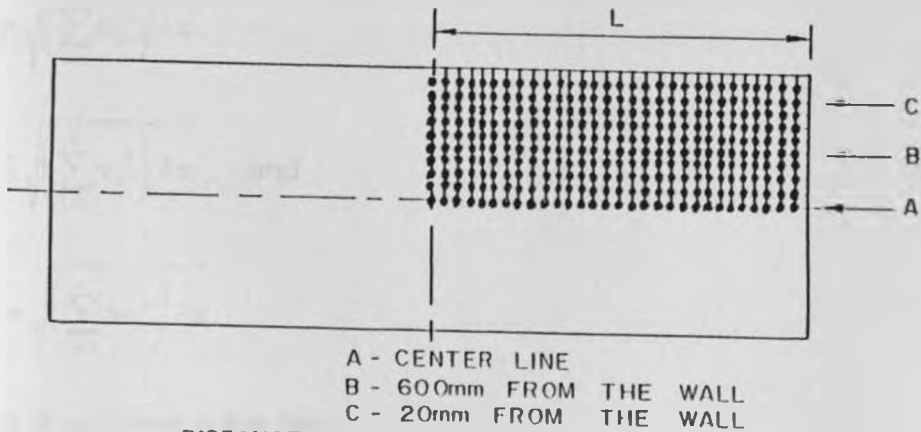
$$\bar{V} = \left( \sum_{i=1}^x V_i \right) / x \quad (5-21)$$

$$\bar{W} = \left( \sum_{i=1}^x W_i \right) / x \quad (5-22)$$

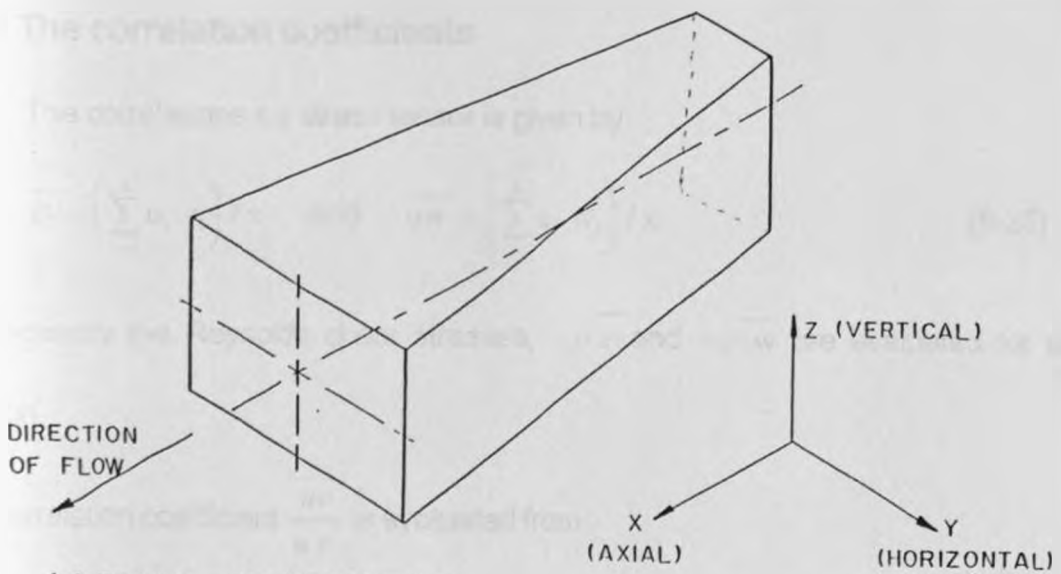
Figure 5 TEST POSITIONS AND FRAME OF REFERENCE



(a) POSITIONS OF THE PLANES OF MEASUREMENT



(b) EXPERIMENTAL NODES ON A TYPICAL MEASUREMENT PLANE



(c) FRAME OF REFERENCE

### 5.3.2 Axial, horizontal and vertical fluctuating velocities

From equations 5-15 one can write the following equations for the fluctuating velocities:

$$\begin{aligned}u_i &= U_i - \bar{U} \\v_i &= V_i - \bar{V} \quad \text{and} \\w_i &= W_i - \bar{W}\end{aligned}\tag{5-23}$$

Defining  $u'$ ,  $v'$  and  $w'$  as the root mean square of the fluctuating velocities  $u_i$ ,  $v_i$  and  $w_i$ , respectively, we have

$$\begin{aligned}u' &= \sqrt{\left(\sum_{i=1}^x u_i^2\right) / x} \\v' &= \sqrt{\left(\sum_{i=1}^x v_i^2\right) / x}, \quad \text{and} \\w' &= \sqrt{\left(\sum_{i=1}^x w_i^2\right) / x}.\end{aligned}\tag{5-24}$$

The means of  $u_i$ ,  $v_i$  and  $w_i$  are zero.

### 5.3.3 The correlation coefficients

The correlations x-y stress tensor is given by

$$\overline{uv} = \left(\sum_{i=1}^x u_i v_i\right) / x \quad \text{and} \quad \overline{uw} = \left(\sum_{i=1}^x u_i w_i\right) / x\tag{5-25}$$

Subsequently the Reynolds shear stresses,  $-\rho \overline{uv}$  and  $-\rho \overline{uw}$  are evaluated for each position.

The correlation coefficient  $\frac{\overline{uv}}{u'v'}$  is evaluated from

$$\frac{\overline{uv}}{\overline{u} \overline{v}} = \frac{\sum_{i=1}^n u_i v_i / x}{\overline{u} \overline{v}} \quad (5-26)$$

Similarly the correlation coefficient  $\frac{\overline{uw}}{\overline{u} \overline{w}}$  may be obtained as;

$$\frac{\overline{uw}}{\overline{u} \overline{w}} = \frac{\sum_{i=1}^n u_i w_i / x}{\overline{u} \overline{w}} \quad (5-27)$$

### 5.3.4 The turbulent kinetic energy

The turbulent kinetic energy,  $k$ , can be evaluated following the equation

$$k = 1/2(u'^2 + v'^2 + w'^2) \quad (5-28)$$

Thus, equations 5-24 are used.

### 5.3.5 Taylor's microscales

By definition the Taylor's microscale  $\lambda_u$  is

$$\lambda_u = \overline{U} \left[ \frac{\overline{u^2}}{\left(\frac{\partial u}{\partial x}\right)^2} \right]^{1/2} \quad (5-29)$$

where

$$\overline{\left(\frac{\partial u}{\partial x}\right)^2} = m \quad (5-30)$$

$m$  is given by

$$m = \frac{1}{t^2} \left[ \frac{\sum_{i=1}^{n-1} (u_{i+1} - u_i)^2}{n-1} \right] \quad (5-31)$$

where  $t$  is the time interval between any two consecutive readings.

Therefore

$$\lambda_u = \bar{U} \left[ \frac{\overline{u^2}}{m} \right]^{1/2} = \frac{\bar{U} \bar{u}'}{\sqrt{m}} \quad (5-32)$$

Similarly  $\lambda_v$  and  $\lambda_w$  are given respectively by

$$\lambda_v = \frac{\bar{U} \bar{v}'}{\sqrt{m}} \quad \text{and} \quad (5-33)$$

$$\lambda_w = \frac{\bar{U} \bar{w}'}{\sqrt{m}} \quad (5-34)$$

Values of  $\lambda_u$ ,  $\lambda_v$ , and  $\lambda_w$  were found to be almost identical and hence only  $\lambda_u$  was presented.

### 5.3.6 The turbulent K.E. dissipation rate and the Kolmogoroff's scales

The turbulent kinetic energy dissipation rate is given by

$$\varepsilon_u = 15\nu \frac{\overline{u^2}}{(\lambda_u)^2} = \frac{15\nu u^2}{(\lambda_u)^2} \quad (5-35)$$

where  $\nu$  is the Kinematic viscosity of air.

The Kolmogoroff length, velocity and time scales were evaluated according to equations 3-37.

### 5.3.7 The turbulence intensities

$$\text{Turbulence intensity in x direction} = \frac{u}{U} \quad (5-36)$$

$$\text{Turbulence intensity in y direction} = \frac{v}{U} \quad (5-37)$$

$$\text{Turbulence intensity in z direction} = \frac{w}{U} \quad (5-38)$$

### 5.3.8 The Eulerian integral scales and auto-correlation coefficients

By definition the Eulerian integral scale is obtained from

$$L_{ij} = \overline{UT_{ij}}, \quad i,j=1,2,3, \quad (5-39)$$

where

$$T_{ij} = \int_0^{\infty} R_{ij}(\tau) d\tau, \quad i,j=1,2,3, \quad (5-40)$$

and



$$R_{ij}(\tau) = \frac{\overline{u_i(t)u_i(t+\tau)}}{\overline{u_i} \overline{u_j}} \quad ; \quad i,j=1,2,3. \quad (5-41)$$

Therefore,

$$T_{ij}(t) = \frac{\sum_{i=1}^k (u_i u_{i+1} t)}{k(u_i u_j)} \quad , \quad i,j=1,2,3, \quad (5-42)$$

where  $t$  is the time interval between any two consecutive readings. The summation was stopped when the value of  $k$  was such that  $R_{ij}(\tau)$  was nearly zero.

$$L_{ij} = \overline{UT}_{ij} \quad (5-43)$$

## 5.4 Error analysis for hot wire measurements

### 5.4.1 Temporal resolution

The temporal resolution of the measuring system can be determined by comparing the characteristics times of the hot wire and the A/D conversion system with the characteristic times of the flow. A typical convection time (Corrsin [1963]) of the smallest relative motions (corresponding to viscous dissipation phenomena) is given as

$$\left(\frac{1}{U}\right) \left(\frac{v^3}{\varepsilon}\right)^{1/4} \quad (5-44)$$

The typical convective time of energy containing eddies,  $T_u$  was on average constant at 0.022 seconds.

The characteristic time for hot wire is given by

$$\frac{d_{\text{Sensor}}}{U_{bt}} \quad (5-45)$$

where  $d_{\text{Sensor}}$  is the diameter of the sensor.

The sampling time for data acquisition was 0.00345 seconds.

From a typical position, one would observe that a phenomena associated with energy production and transfer within the inertial subrange of the energy spectrum would be detected, while the fastest, dissipative actions might be unresolved.

#### 5.4.2 Spatial resolution

For a cylindrical hot wire, the spatial resolution is limited by the length of the wires and the distance between the sensors in the case of cross wire probe. The length and spacing of the sensors can be compared with the characteristic length scales of the flow. If the sensor spacing is  $\delta_s$  and the sensor length is  $l_s$ , then for a given position, it is possible to obtain ratios such as  $l_s/\lambda_u$ ,  $l_s/\eta$ ,  $\delta_s/\lambda_u$ , and  $\delta_s/\eta$ .

The resulting errors in turbulence characteristics can be estimated from these ratios assuming a likely turbulence structure. For example, the measurement error in  $\overline{u^2}$  can be estimated as (Corrsin [1963])  $(\overline{u^2} - \overline{u^2_{measured}}) / \overline{u^2} \approx l_s / 24\lambda_u^2$ . Thus the measurement error of the fluctuating velocity component in the axial direction may be evaluated (typically the resulting errors were less than 0.3%, but varied from point to point).

# CHAPTER SIX

## RESULTS AND DISCUSSIONS

Apart from the preliminary tests which were carried out by use of single wire anemometry, all the results presented in this chapter were carried out using cross hot wire anemometry. The effect on these results by varying the ducts half angle and the distance from the exit plane and the presence of solid walls are discussed.

### 6.1 Preliminary tests

The initial preliminary tests were carried out on the circular duct. Before any hot-wire anemometry tests were carried out, it was necessary to establish the variation of both atmospheric pressure and temperature with time. This is shown in Figures 6 and 7 respectively. Although from time to time during the duct's operating time, calibration of the hot wire anemometer was carried out, both pressure and temperature were not constant and an average value for the day was used for calculations. These two parameters were measured at the circular duct's entry, upstream of the axial fan.

However, the average value taken varied by less than 1% for the atmospheric pressures. The temperature variation was more significant in that the mornings were always cold with temperatures less than 20°C while the afternoons had over 25°C. This in typical days gave a variation of less than 2.5%.

The frequency inverter was calibrated in terms of velocity for both circular and rectangular duct's exit planes. Shown in Figures 8 and 9 are typical inverter calibration

curves. The axial velocity varied linearly with the inverter frequency for both circular and rectangular ducts. This enabled one to relate the inverter frequencies to actual velocities it was therefore possible to choose accurately the air velocity at both positions from these graphs for the other preliminary tests that were required.

A major concern in fluid experiments is the effect of Reynolds number on any test parameters. Shown in Figure 10 are the effects of Reynolds number on turbulence characteristics within the range, the experiments were conducted was insignificant. The axial turbulence intensity was chosen to represent the other turbulence characteristics.

The statistical approach adopted in this research assumed that the turbulence was isotropic. Various turbulence characteristics (non-dimensionalized time averaged mean axial velocity and axial turbulence intensity) were tested with respect to time.

Results showed that, there was very little variation on these parameters with a maximum value less than 5% at different Reynolds number. This is shown in Figure 11. Symmetry tests at the circular duct's exit and at the test section exit plane were carried out.

For the test section, the symmetry tests were in both vertical and horizontal directions. Results showed that the flow was symmetrical. In addition, the velocity distribution portrayed a turbulent flow. This is shown in Figures 12, 13 and 14.

Another major concern in the present study was whether in the region of interest, the flow had separated. Separation tests were carried out and for angles up to  $20^{\circ}$ , there was no evidence of separation. All the subsequent experiments were carried out at an inverter frequency of 40Hz. This was mainly because at higher inverter

frequencies, the effects of vibration were significant while at low frequencies the flow was not fully developed at the inlet plane of the test section.

## 6.2 Velocity measurements

### 6.2.1 Axial mean velocity

Shown in Figures 15,16, 17 and 18 are the mean axial velocity isovel contours for half angles of  $10^{\circ}$ ,  $15^{\circ}$ ,  $17.5^{\circ}$  and  $20^{\circ}$ , respectively.

The measurements were carried out at four different planes, that is, at the exit plane, at 100 mm, at 200 mm and at 300 mm from the exit plane and the test positions that facilitated plotting of the contours are shown in Figure 5(b). All other subsequent turbulence characteristics were measured at the same locations as the axial mean velocity.

Four values of the isovel contours were selected for presentation. These were values of  $\overline{U} / \overline{U}_c$  equivalent to 0.95, 0.90, 0.85 and 0.80 and were presented for all planes of measurements. As would be expected, due to the presence of the boundary layer, the axial mean velocity reduced towards the wall. The maximum value of  $\overline{U}$  was obtained at the centre of the duct and was used to normalize the axial mean velocities in the other positions.

Results showed that for a given distance from the centreline along the axial direction, the axial mean velocity increased with increasing distance from the exit plane. This is consistent with the requirements of continuity equation of fluids in motion, since as the distance from the exit plane is increased, the cross-sectional area normal to the flow reduces.

It was observed that for any given position, the axial mean velocity reduced with increasing half angle. This was due to the same requirement of continuity equation. Isovel contours for the mean axial velocity show that, the isovels are displaced towards the corners of the duct. This could be attributed to the presence of secondary flow (in most cases between 10 and 15% of the mean flow).

From the contours, one can observe that the bulging is almost symmetrical about the bisector line.

Another consistent observation is that, the contours get closer to each other as the distance from the exit plane is increased. They are also observed to be closer to each other as the half angle is reduced.

Both these observations may be attributed to the degree of turbulence as the angle and the distance from the exit plane are varied. The flow is more turbulent for larger angles and smaller distances from the exit plane. This observation may also be supported by the behaviour of the fluctuating axial velocity, which provides a measure of the turbulence intensity.

## 6.2.2 Secondary flow

For flow in a non-circular duct, the  $x$ -axis is defined in the direction of the duct centreline and  $y$  and  $z$ -axis are orthogonal coordinates in the lateral cross-section as shown in Figure 5(c). The flow in the axial direction is described by  $\bar{U}$  and the secondary flows by  $\bar{V}$  and  $\bar{W}$ .

Shown in Figures 19, 20 and 21 are the mean horizontal velocity profiles presented in the form  $\bar{V}/\bar{U}_c$ . Results show that, generally for all angles, the mean horizontal velocity increases as the wall is approached. The mean horizontal velocity decreased with increasing half angle and increasing distance from the exit plane. Negative values were obtained near the walls and were more pronounced for measurements taken along 20 mm from the wall.

Figure 22, 23 and 24 show the mean axial velocity profiles presented in the form  $\bar{W}/\bar{U}_c$ . The flow was expected to be two-dimensional with very little variation of the vertical mean velocity. This was not generally the case. Results show that the vertical mean velocity reduce with increasing distance from the exit plane. In majority of cases, it increases with increasing half angles. Again, negative values were obtained near the walls and were more pronounced for measurements along 20 mm from the wall.

This can be attributed to the fact that, near the walls, there must be negligible production of vorticity, which leaves the area near the bisector as the only possible region from which vorticity may arise. Within the triangular sector between the bisector and the corner, the production must be negative, tending to produce clockwise rotation of fluid elements.

The normalized secondary flow was in the range of between 0.1 and 0.15 absolute. This Figure looks abnormally high as compared to approximately 0.01 for flows within straight ducts (Brundett and Baines [1964]).

This abnormal increase may be attributed to the diverging configuration of the duct which would naturally make the flow at least two-dimensional in the mean velocity field, even at low Reynolds number. This may also be confirmed by the fact that the secondary flow is generally observed to increase with increasing half angles.

### 6.2.3 Turbulence intensities

Shown in Figures 25,26 and 27 are profiles of the axial turbulence intensities,  $u' / \bar{U}$ . Results indicate that the axial turbulence intensities increase towards the walls. They reduced as the distance from the exit plane was increased. Along the centreline the axial turbulence intensities for  $15^\circ$ ,  $17.5^\circ$  and  $20^\circ$  were nearly of the same order of magnitude. The axial turbulence intensities for these angles along the centreline were in the range of 20% and 35%.

Along 20 mm and 60 mm from the wall, it can be observed that the axial turbulence intensities for  $10^\circ$  and  $15^\circ$  are distinctively higher than those of  $17.5^\circ$  and  $20^\circ$ . This behaviour may be attributed to the fact that the degree of turbulence (or degree of randomness) increases as the wall is approached and furthermore results from this research indicate that the degree of turbulence also increases with increasing half angles.

The effect of change of the half angles on turbulence intensities seems to be more pronounced than the effect of proximity to the wall.



Figures 28, 29 and 30 are the horizontal turbulence intensity profiles  $v' / \bar{U}$ .

The horizontal turbulence intensities were almost the same as those of the axial turbulence intensities and portrayed similar profiles.

The behaviour of the vertical turbulence intensities  $w' / \bar{U}$  are shown in Figures 31, 32 and 33. Even though they varied in almost a similar way and also portrayed the same profiles, their magnitude are somewhat higher than those of both axial and horizontal turbulence intensities. The turbulence intensities increase towards the walls (within the vicinity of the boundary layer) due to exchange of momentum between the fluctuating and the mean velocity fields.

### 6.3 Reynolds shear stress and correlation coefficients

Shown in Figures 33 to 39 are the Reynolds shear stresses profiles. Two of the three off diagonal Reynolds shear stresses were measured. These were;  $-\overline{\rho uv}$  and  $-\overline{\rho uw}$ . The three normal stresses were also measured but since they do not play an important role in transport of momentum, they are not presented here.

Results showed that stresses reduced as the wall was approached with no distinct pattern. This can also be observed since values of Reynolds stresses measured along the centreline are higher than those measured along 20 mm and 60 mm from the wall. This may be attributed to the fact that at the wall the production of vorticity is zero and therefore Reynolds shear stresses must be zero at the wall and very small within the viscous sublayer (Brundett and Baines [1964]). The values of the

Stresses were up to a maximum of  $2.00 \text{ N/m}^2$ , while the minimum was maintained at  $0.01 \text{ N/m}^2$ .

There seems to be no distinct variation in the Reynolds stresses due to the change in the distances from the exit plane along the axial direction, but on average values of Reynolds shear stresses reduce with increasing half angle. This was observed for both  $-\overline{\rho uv}$  and  $-\overline{\rho uw}$ .

By normalizing Reynolds shear stress by the product of the local rms velocities, the Reynolds shear stress can be presented as a correlation coefficient. This was done for  $\overline{uv} / u'v'$  and  $\overline{uw} / u'w'$  only as shown in Figures 40 to 45. The maximum value achieved for  $\overline{uv} / u'v'$  was on average 0.4 to 0.55, while the maximum value for  $\overline{uw} / u'w'$  was 0.8. In all cases values of  $\overline{uw} / u'w'$  were always greater than those of  $\overline{uv} / u'v'$ .

stresses were up to a maximum of  $2.00 \text{ N/m}^2$ , while the minimum was maintained at  $0.01 \text{ N/m}^2$ .

There seems to be no distinct variation in the Reynolds stresses due to the change in the distances from the exit plane along the axial direction, but on average values of Reynolds shear stresses reduce with increasing half angle. This was observed for both  $-\overline{\rho uv}$  and  $-\overline{\rho uw}$ .

By normalizing Reynolds shear stress by the product of the local rms velocities, the Reynolds shear stress can be presented as a correlation coefficient. This was done for  $\overline{uv}/u'v'$  and  $\overline{uw}/u'w'$  only as shown in Figures 40 to 45. The maximum value achieved for  $\overline{uv}/u'v'$  was on average 0.4 to 0.55, while the maximum value for  $\overline{uw}/u'w'$  was 0.8. In all cases values of  $\overline{uw}/u'w'$  were always greater than those of  $\overline{uv}/u'v'$ .

## 6.4 Turbulent kinetic energy and turbulent kinetic energy dissipation rate.

Presented in Figures 46,47 and 48 are plots of turbulent kinetic energy per unit mass. It was observed that values of the turbulent kinetic energy decreased as the distance from the exit plane was increased. Generally, turbulent kinetic energy was found to be maximum near the walls and minimum at the centre.

The maximum value of turbulent kinetic energy obtained was  $11 \text{ m}^2/\text{s}^2$  while the minimum was  $0.2 \text{ m}^2/\text{s}^2$ . Measurements taken along the centreline and along a distance 60 mm from the wall indicated that turbulent kinetic energy measured for a half angle of  $10^\circ$  generally gave lower values.

Other noticeable observation was that, for measurements along 20 mm distance from the wall, turbulent kinetic energy for  $17.5^\circ$  and  $20^\circ$  remained fairly constant for the first three planes of measurement.

Figures 49, 50 and 51 show the turbulent kinetic energy dissipation rate. The dissipation rate for half angles of  $10^\circ$  and  $15^\circ$  were always lower than for  $17.5^\circ$  and  $20^\circ$ .  $10^\circ$  had the lowest dissipation rate.

In most of the cases the dissipation rate increased as the distance from the centre was increased and had the highest values at the wall. The highest dissipation rate achieved was  $0.11 \text{ m}^2/\text{s}^2$  per second with average values of 0.01 to  $0.05 \text{ m}^2/\text{s}^2$  per second.

## 6.5 Scales

### 6.5.1 Taylor's microscales

Figures 52, 53 and 54 present the distribution of the Taylor's microscales. It was observed that the Taylor's microscales for  $17.5^\circ$  and  $20^\circ$  were distinctively lower than those for  $10^\circ$  and  $15^\circ$  and reduced generally with increasing half angle.

The effect of the wall and the distance from the exit plane on the microscales seems to be insignificant. The maximum values obtained were 0.45 mm and a minimum value of 0.05 mm.

### 6.5.2 Kolmogoroff's velocity scale

Figures 55, 56 and 57 show the distribution of the Kolmogoroff's velocity scale. Noticeably the Kolmogoroff's velocity scale for  $10^\circ$  was almost always lower than for the other angles, while the velocity for  $17.5^\circ$  and  $20^\circ$  remained almost constant at higher values. The Kolmogoroff's velocity scale increase with increasing half angle. However the effect of the distance from the exit plane is insignificant.

The general trend for  $10^\circ$  as can be observed is that it always reduced towards the wall, but attained high values for distances very near the wall.

The maximum values obtained were 0.025 to 0.035 mm/s, while the lowest values were 0.01 mm/s.

### 6.5.3 Kolmogoroff's time scale

Values of the time scale for  $10^\circ$  were always higher than those of the others.

This is shown in Figures 58, 59 and 60. The general trend was such that the time scale for  $10^\circ$  always increased as the wall was approached and decreased for distances very near the walls. Like the Kolmogoroff's velocity scale  $17.5^\circ$  and  $20^\circ$  showed fairly constant values. The maximum values attained was 0.1 milliseconds while the minimum was 0.01 milliseconds. Values of the time scale generally increased with increase in distance from the exit plane and reduced with increasing half angles.

### 6.5.4 Auto-correlation coefficients

The curves for the auto-correlation coefficients at selected positions are shown in Figures 61, 62 and 63. The decay time for the auto-correlation was found to be between 18 and 24 milliseconds. It was observed that values of auto-correlation for axial, horizontal and vertical directions were almost the same. The delay time seems to be unrelated to the half angles.

# CHAPTER SEVEN

## CONCLUSIONS

The results of this research reveal that the flow within a diverging axisymmetric duct circular duct is three dimensional. The turbulence intensities increased near the walls and were in the range between 15% and 45%, and decreased with increasing distance from the exit plane. Reynolds shear stress varied between 0.01 and 2 N/m<sup>2</sup> while the correlation coefficients showed a maximum value of 0.8. The turbulent kinetic energy measured was between 0.2 and 11 m<sup>2</sup>/s<sup>2</sup>; while the dissipation rate show values in the range between 0.01 and 0.05 m<sup>2</sup>/s<sup>2</sup> per second. The Taylor microscale measured 0.05 mm near the walls and 0.45 mm at the center. The Kolmogoroff's velocity scale varied between 0.01 and 0.035 mm/s while the Kolmogoroff's time scale gave a maximum value of 0.1 milliseconds. Measurements of the Eulerian integral time remained constant at 0.022 seconds.

The main conclusions drawn from measurements in a diverging axisymmetric non-circular duct are listed below

- i. The axial mean velocity bulged towards the corners of the duct. This was caused by the presence of the secondary flow which was between 10% and 15% of the mean axial flow.
- ii. At an equal distance from the centre and outside the boundary layer, the turbulence intensities increased as the half angle was increased and was above 20%. They reduced with increasing distance from the exit plane.

- iii. The values of the Reynolds shear stresses reduce with increasing half angle, had low values near walls and were unaffected by the distance from the exit plane.
- iv. The turbulence kinetic energy increased with increasing half angles and the highest values achieved near the walls.
- v. The rate of dissipation of kinetic energy was greatest at the walls and increased with increasing half angles. However, since the difference in the half angles tested were small, the order of magnitude of the variation of the turbulent kinetic energy dissipation rate was the same.
- vi. The Taylor's microscale did not vary with the distances from the wall and was unaffected by the distance from the exit plane but decreased with increasing half angle of the duct.
- vii. The Kolmogoroff's velocity scale did not vary with distances from the wall but increased with increasing half angle of the duct.
- viii. The Kolmogoroff's time scale did not depend on the distances from the wall but decreased with increasing half angle of the duct.
- ix. The auto-correlation shapes at the centre positions were comparable to those in uniformly shear flows and flows in two dimensional ducts.

The research carried out was mainly concerned with momentum transfer in the turbulent flow field. The author suggests that further work may be carried out to investigate the mass transfer (mixing theory) in a diverging non-circular duct. The behaviour of turbulence characteristics when the flow is reversed (converging duct) may also be considered.



Figure 6 . VARIATION OF TYPICAL ATMOSPHERIC PRESSURE WITH TIME

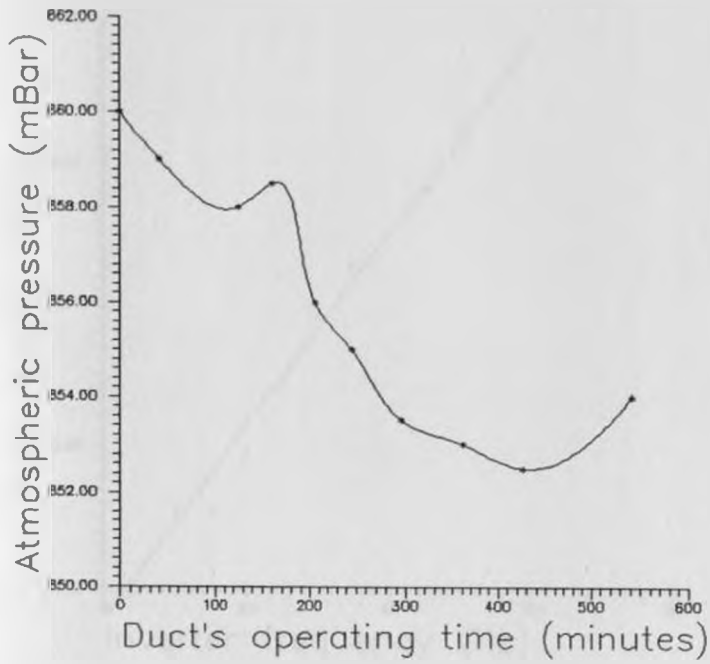


Figure 7 VARIATION OF TYPICAL ATMOSPHERIC TEMPERATURE WITH TIME

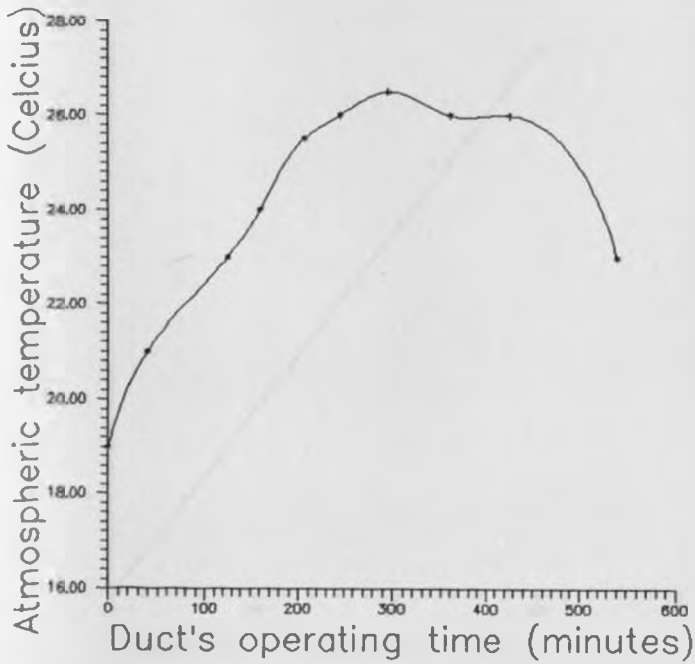


Figure 8 : INVERTER CALIBRATION CURVE AT THE CIRCULAR DUCT'S EXIT

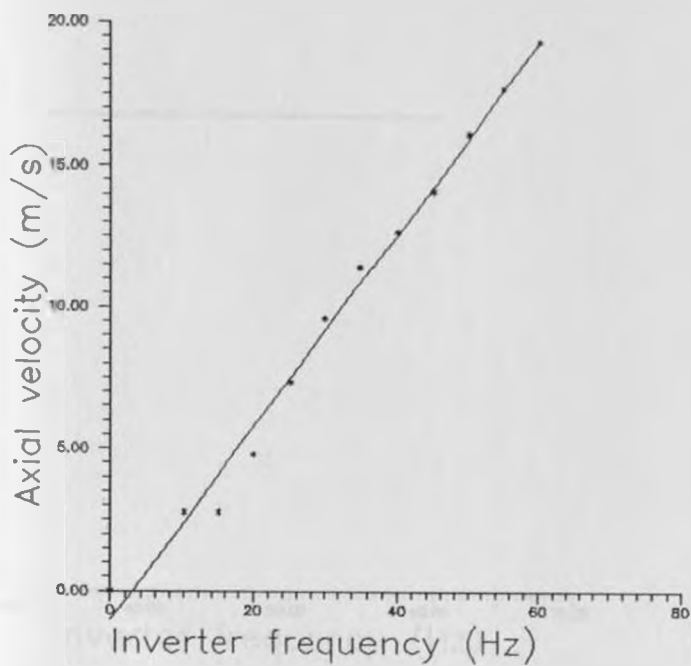


Figure 9 INVERTER CALIBRATION CURVE AT THE RECTANGULAR DUCT'S EXIT

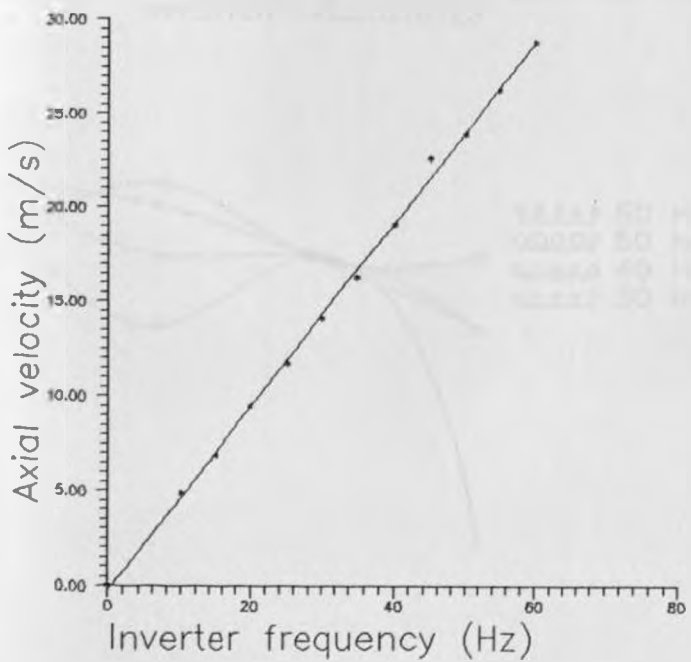


Figure 10 VARIATION OF TURBULENCE INTENSITY WITH FREQUENCY

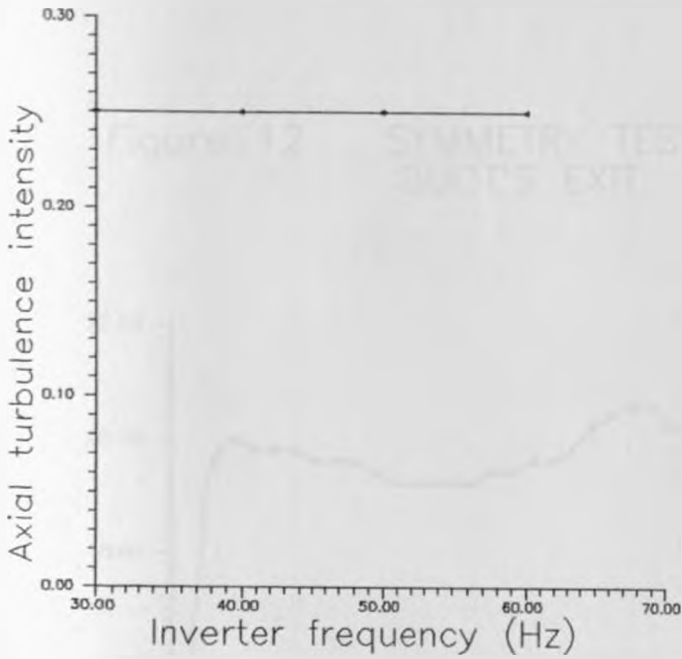


Figure 11 VARIATION OF VELOCITY WITH TIME FOR DIFFERENT INVERTER FREQUENCIES

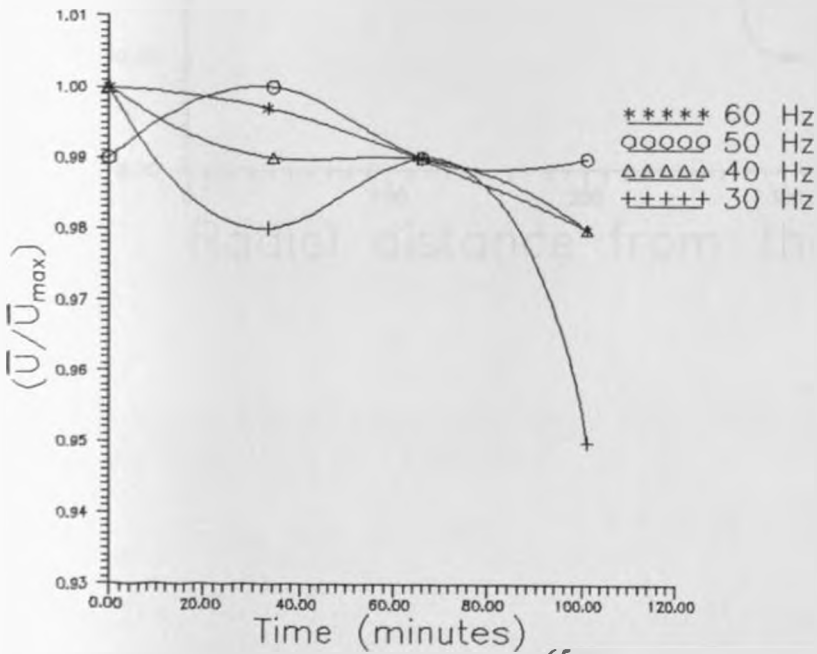


Figure 10 VARIATION OF TURBULENCE INTENSITY WITH FREQUENCY

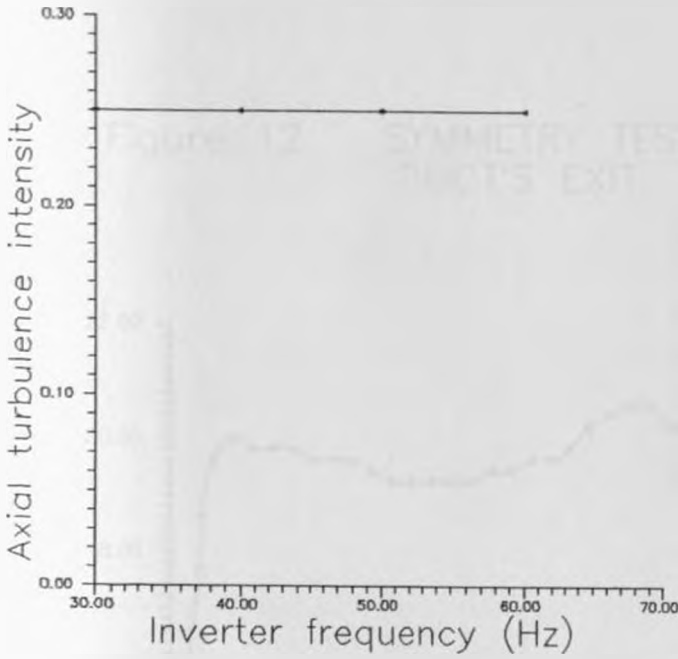


Figure 11 VARIATION OF VELOCITY WITH TIME FOR DIFFERENT INVERTER FREQUENCIES

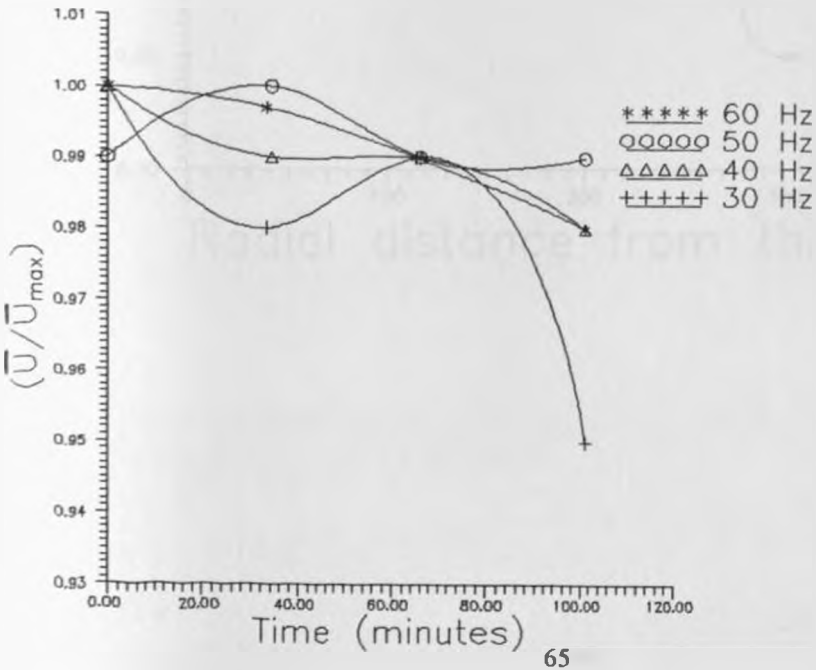


Figure 12 SYMMETRY TEST AT THE CIRCULAR DUCT'S EXIT

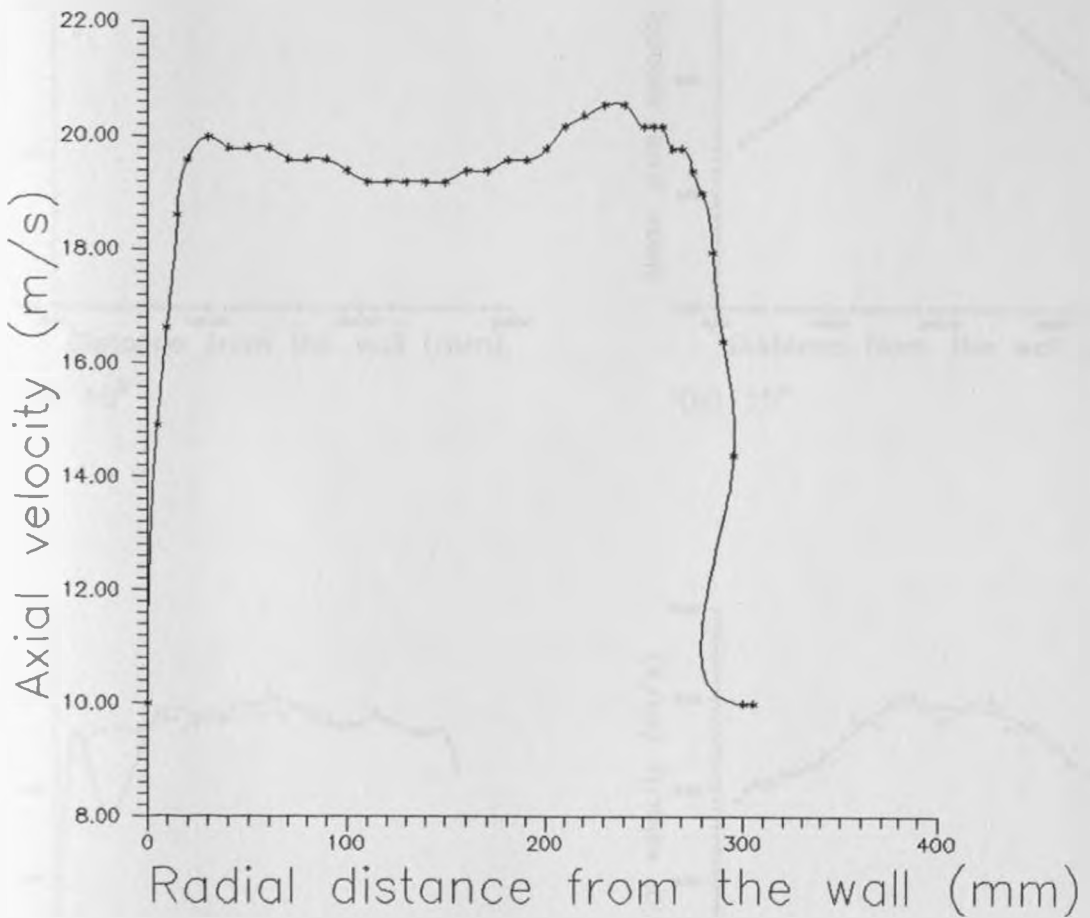
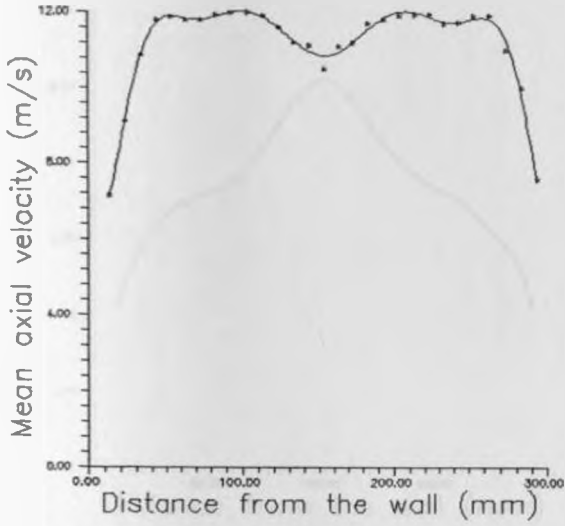
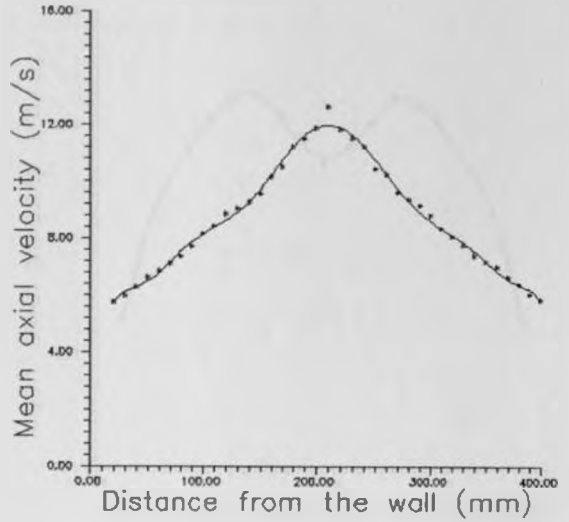


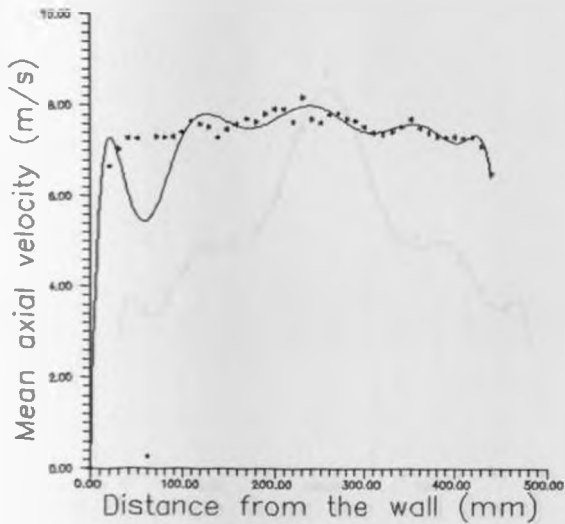
Figure 13 HORIZONTAL SYMMETRY AT THE TEST DUCT'S EXIT PLANE FOR ALL ANGLES



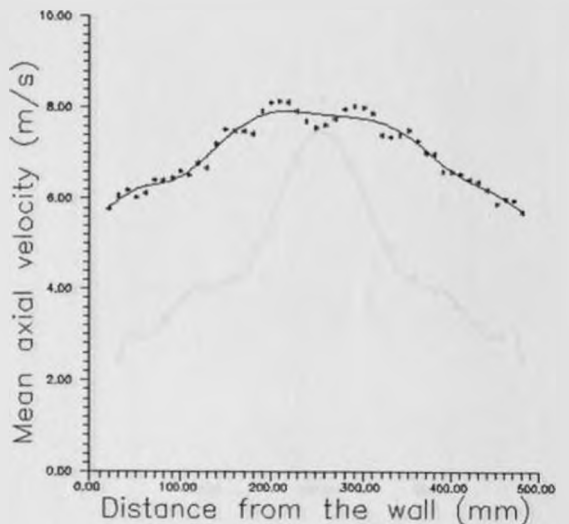
(a)  $10^{\circ}$



(b)  $15^{\circ}$

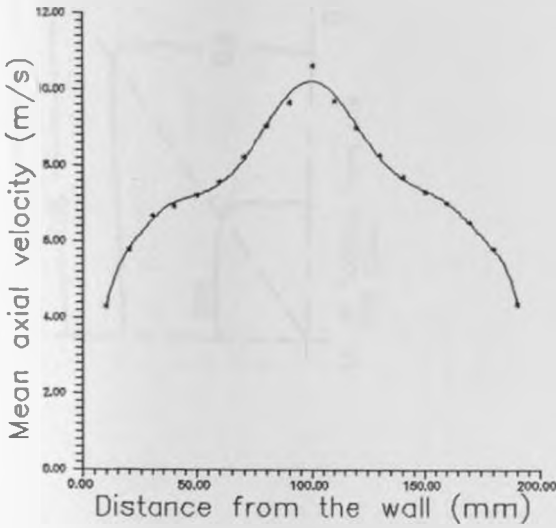


(c)  $17.5^{\circ}$

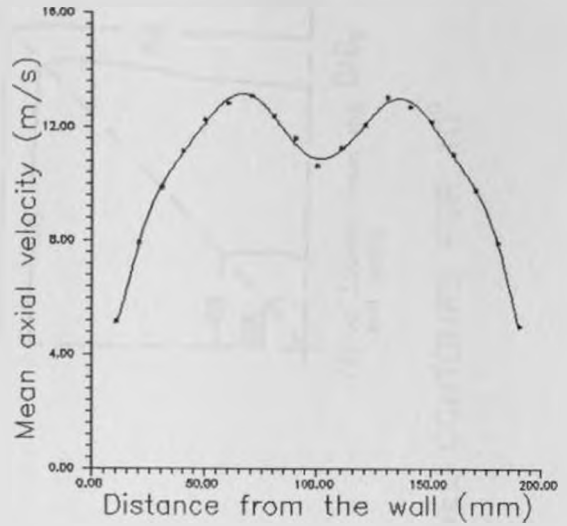


(d)  $20^{\circ}$

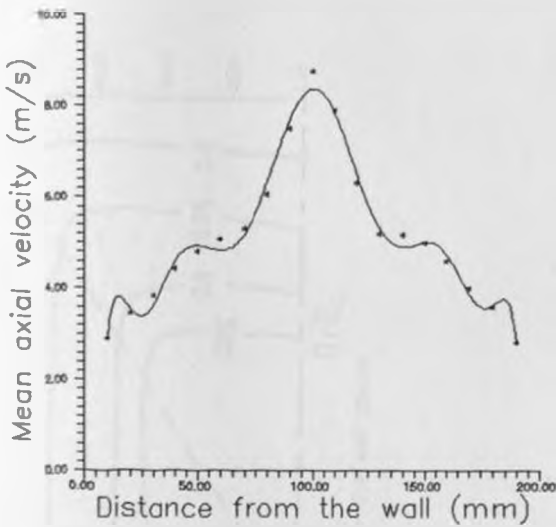
Figure 14 VERTICAL SYMMETRY AT THE TEST DUCT'S EXIT PLANE FOR ALL ANGLES



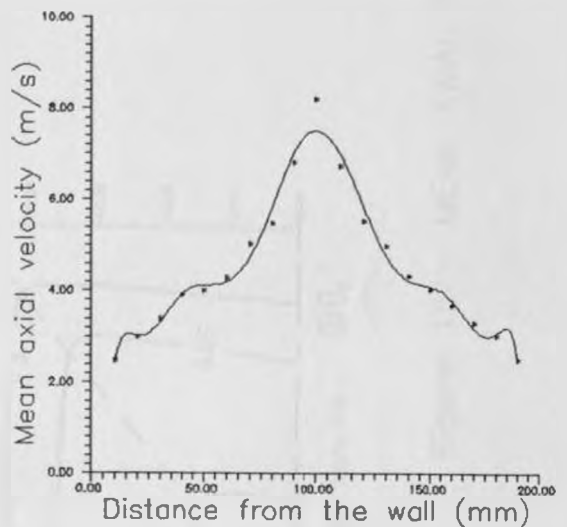
(a)  $10^\circ$



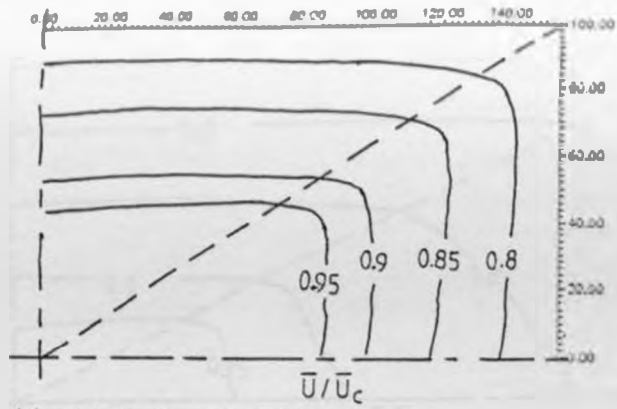
(b)  $15^\circ$



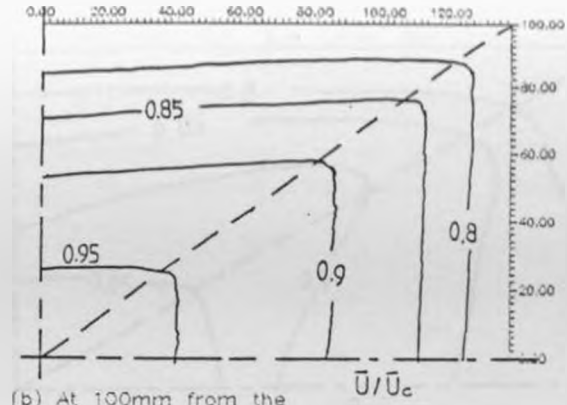
(c)  $17.5^\circ$



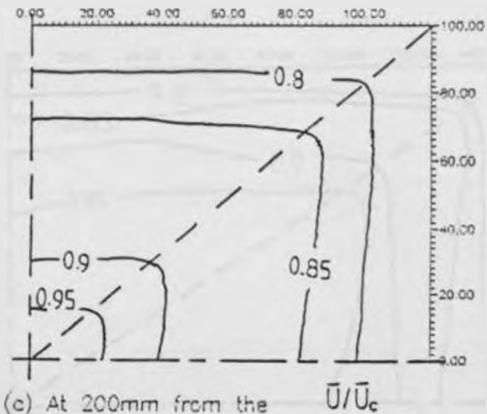
(d)  $20^\circ$



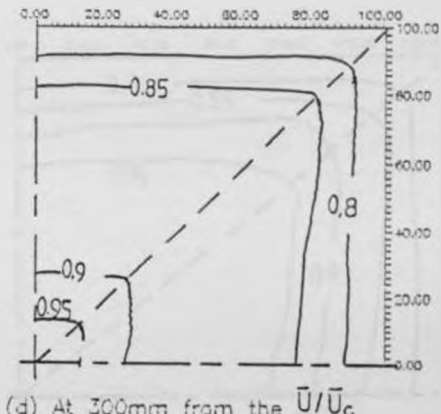
(a) At from the exit plane



(b) At 100mm from the exit plane



(c) At 200mm from the exit plane



(d) At 300mm from the exit plane

Figure 15 MEAN AXIAL VELOCITY ISOVEL CONTOURS FOR  $10^\circ$



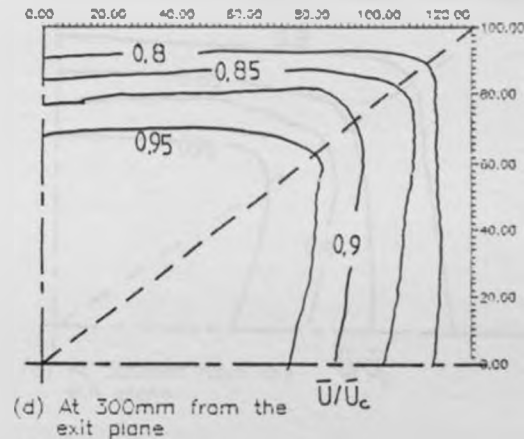
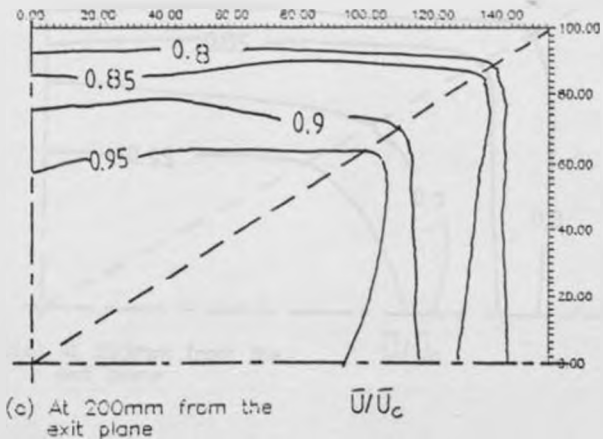
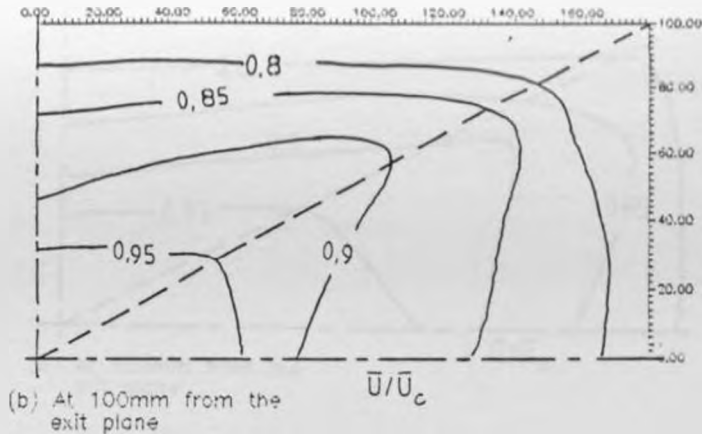
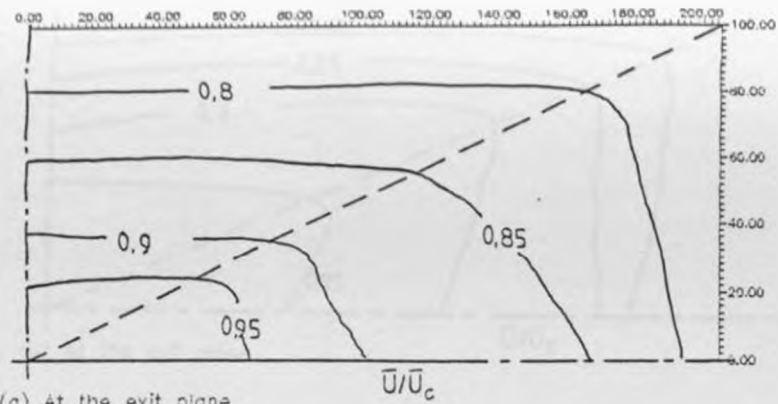
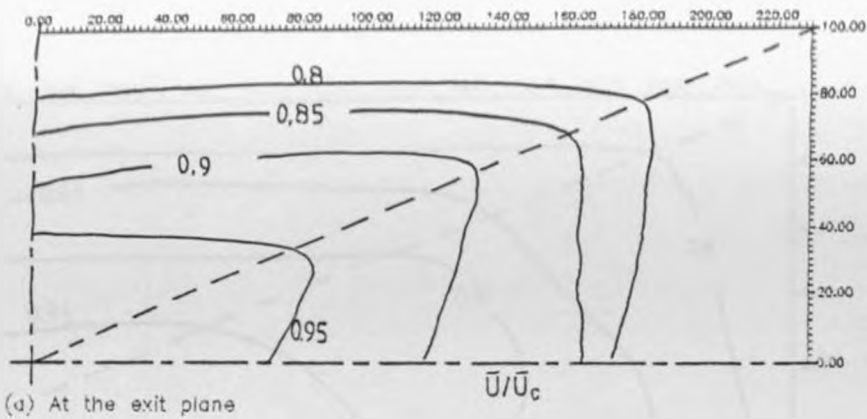


Figure 16 MEAN AXIAL VELOCITY ISOVEL CONTOURS FOR  $15^\circ$



71

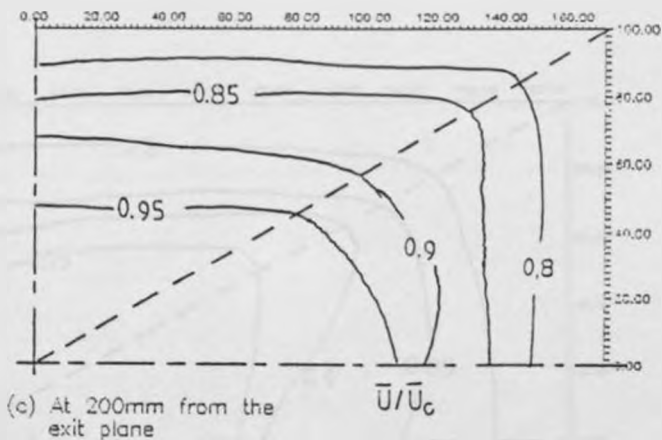
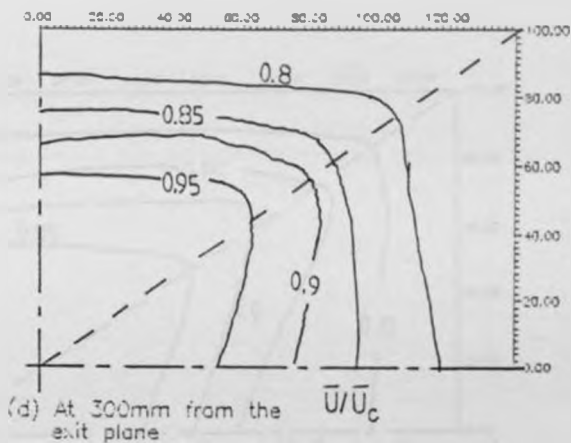
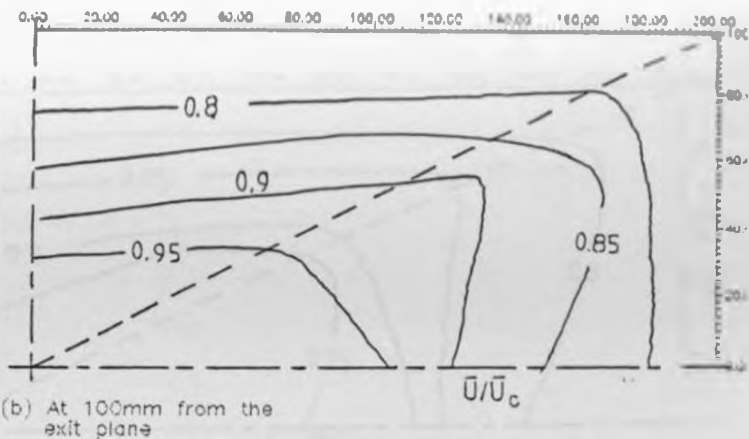
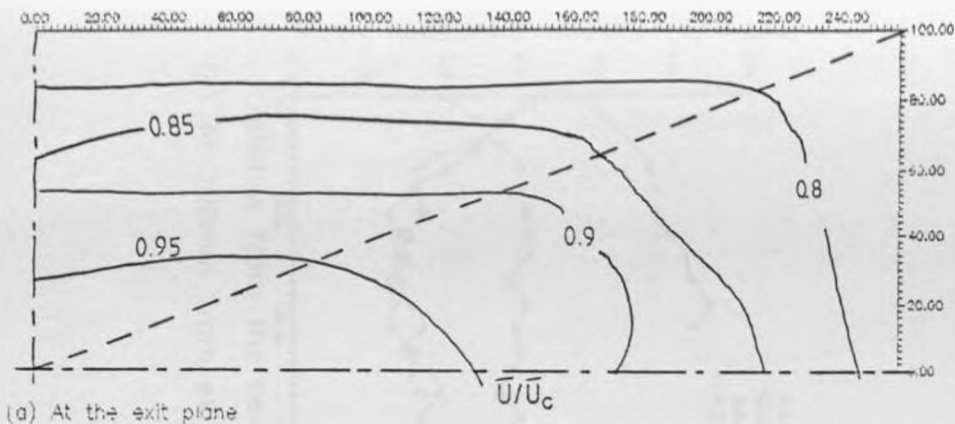


Figure 17 MEAN AXIAL VELOCITY



ISOVEL CONTOURS FOR  $17.5^\circ$



72

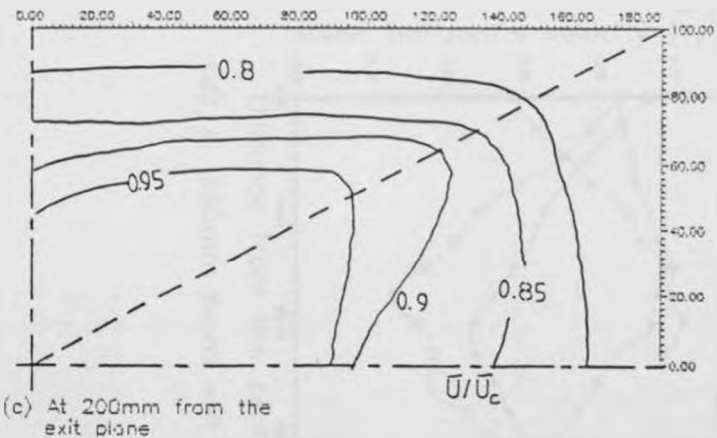
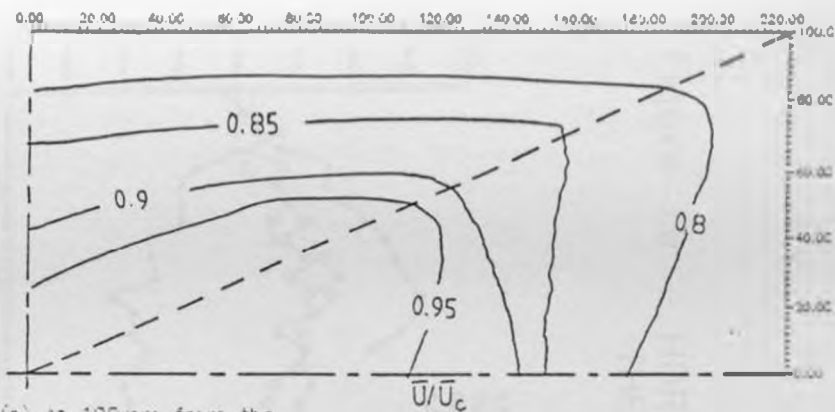
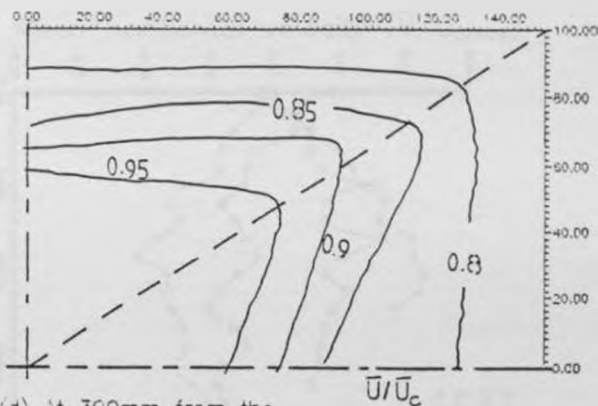


Figure 18 MEAN AXIAL VELOC



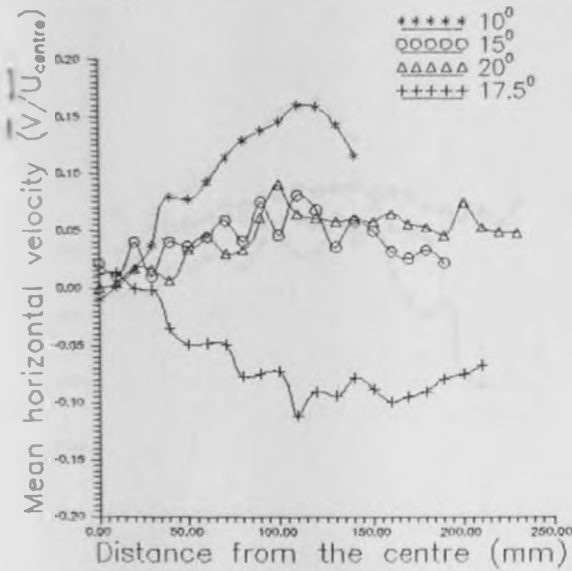
(b) At 100mm from the exit plane



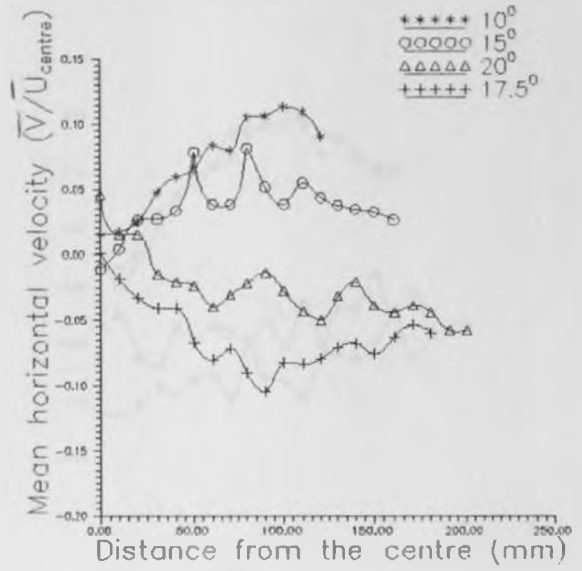
(d) At 300mm from the exit plane

TY ISOVEL CONTOURS FOR  $20^\circ$

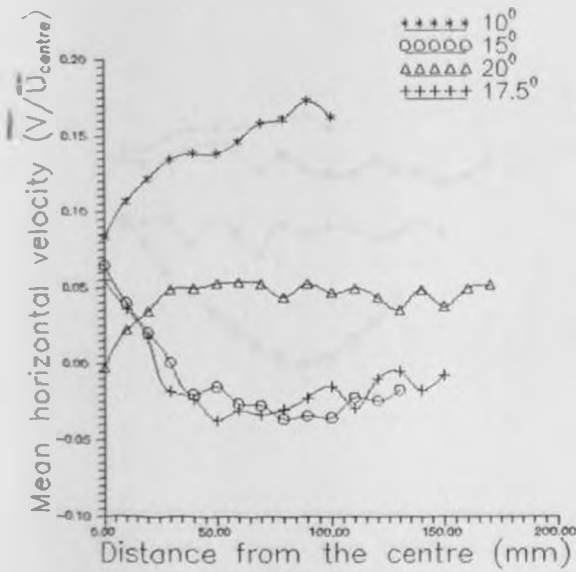
Figure 19 HORIZONTAL MEAN VELOCITY MEASURED ALONG THE CENTRELINE



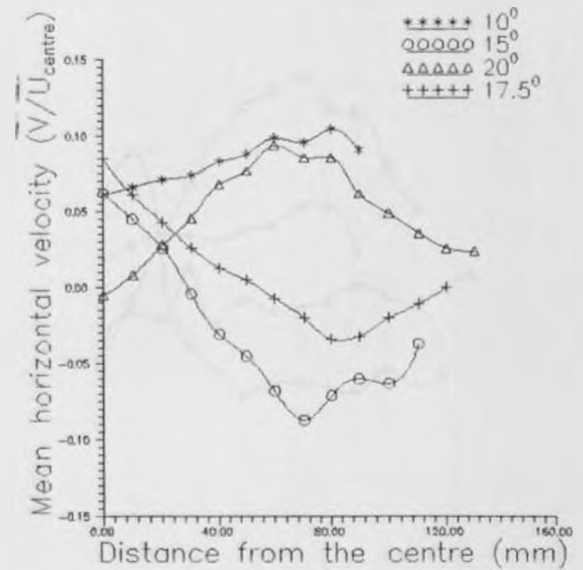
(a) At the exit plane



(b) At 100mm from the exit



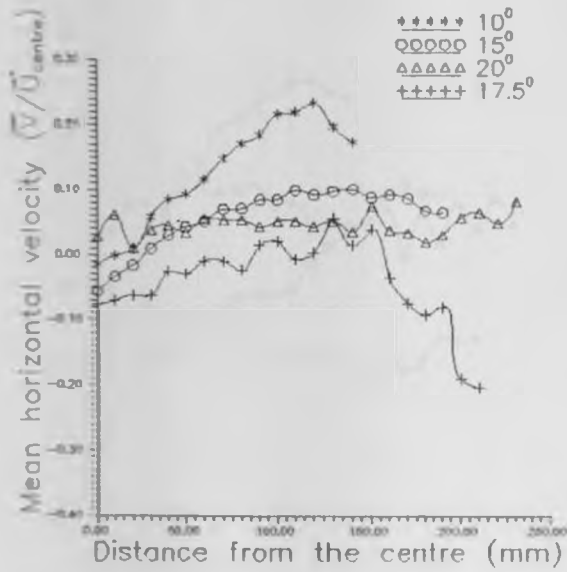
(c) At 200mm from exit



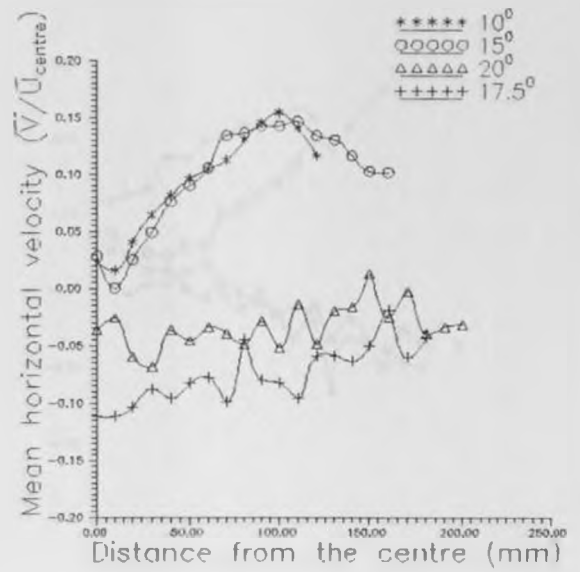
(d) At 300mm from exit

Figure 20

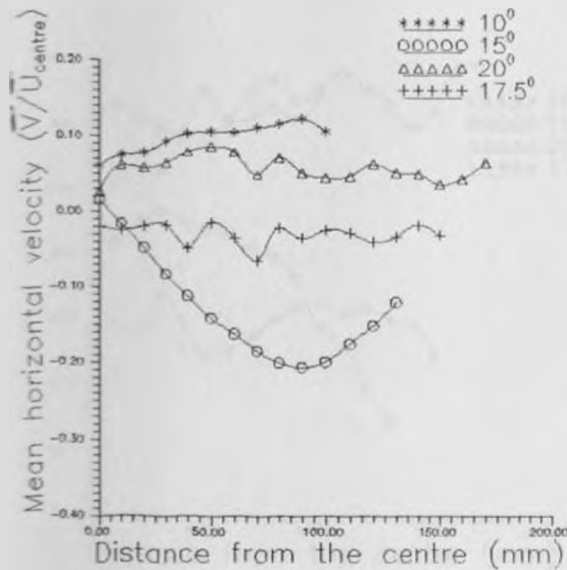
HORIZONTAL MEAN VELOCITY MEASURED ALONG A DISTANCE 60MM FROM THE WALL



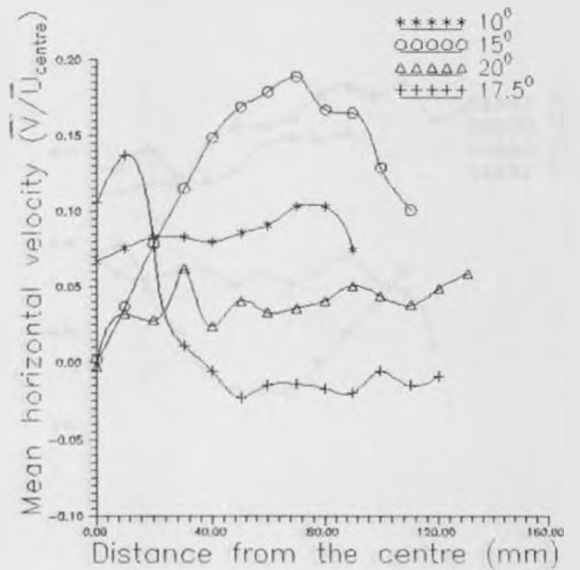
(a) At the exit plane



(b) At 100mm from the exit



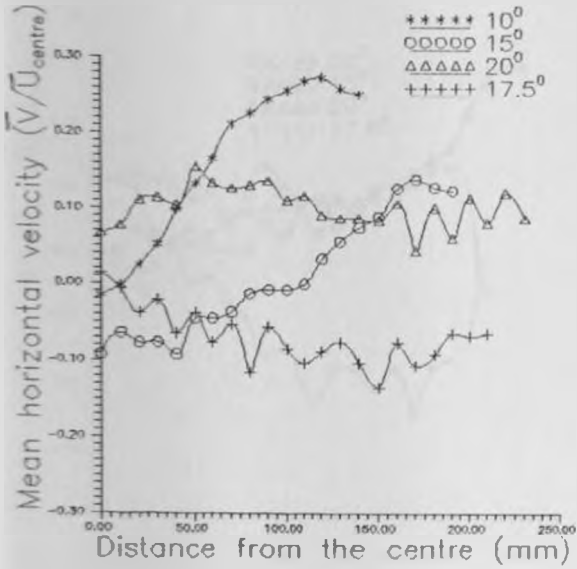
(c) At 200mm from exit



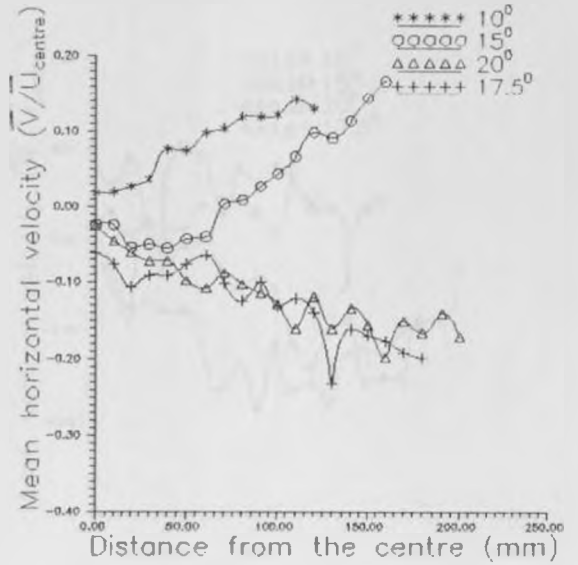
(d) At 300mm from exit

Figure 21

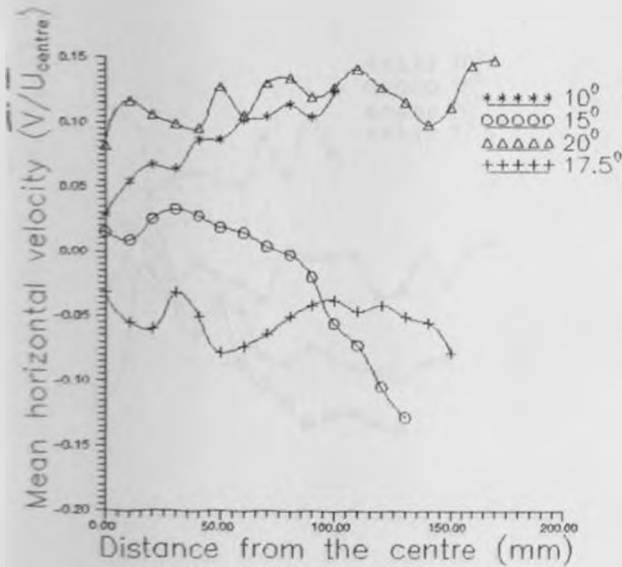
HORIZONTAL MEAN VELOCITY MEASURED ALONG A DISTANCE 20MM FROM THE WALL



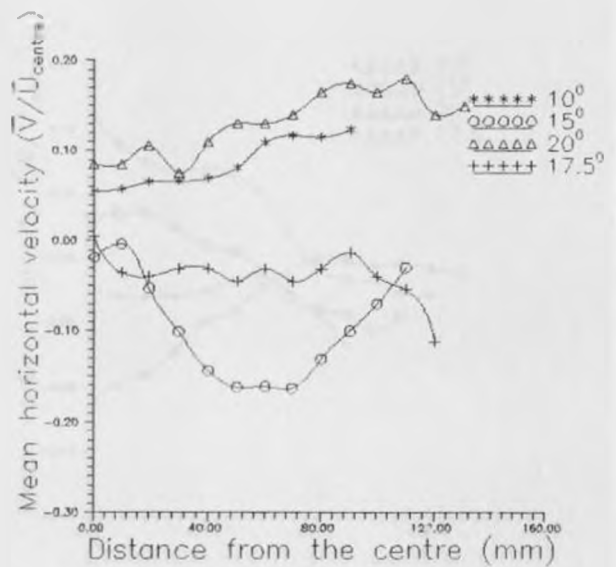
(a) At the exit plane



(b) At 100mm from the exit



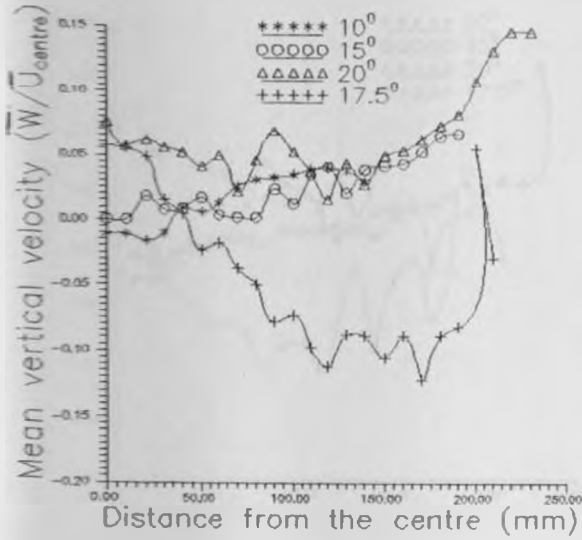
(c) At 200mm from exit



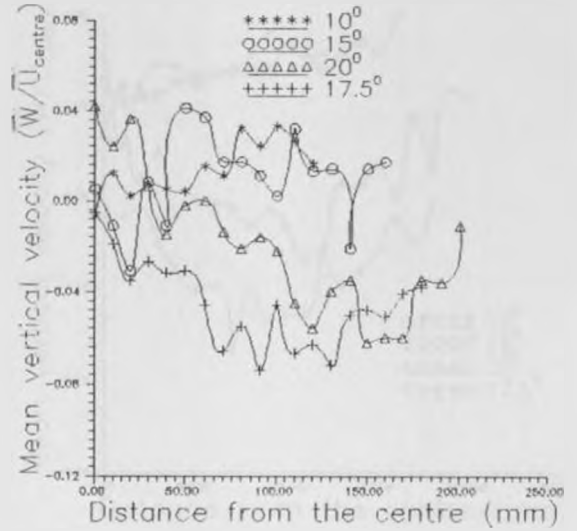
(d) At 300mm from exit



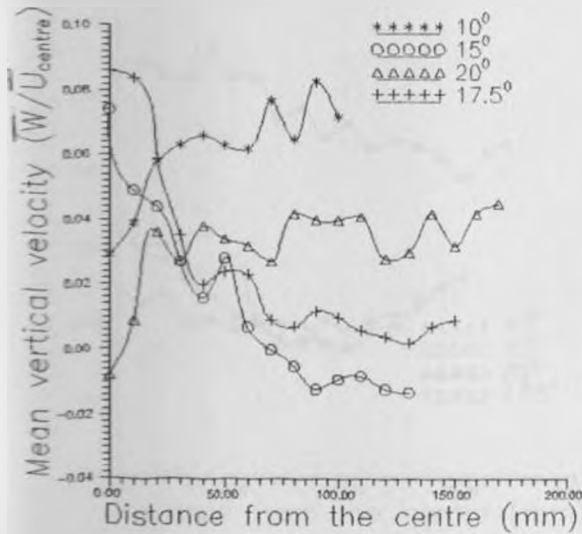
Figure 22 VERTICAL MEAN VELOCITY MEASURED ALONG THE CENTRELINE



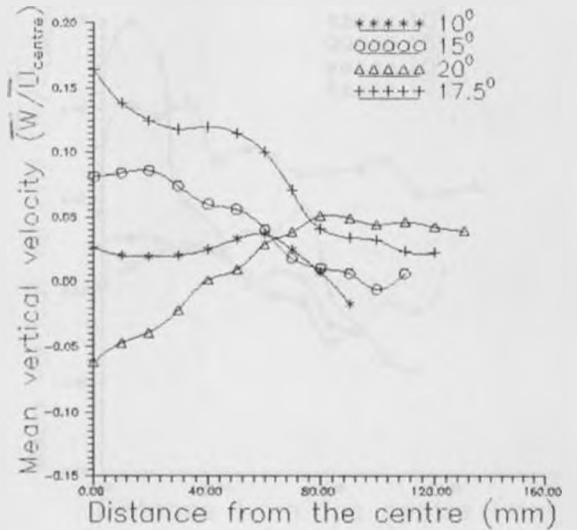
(a) At the exit plane



(b) At 100mm from the exit

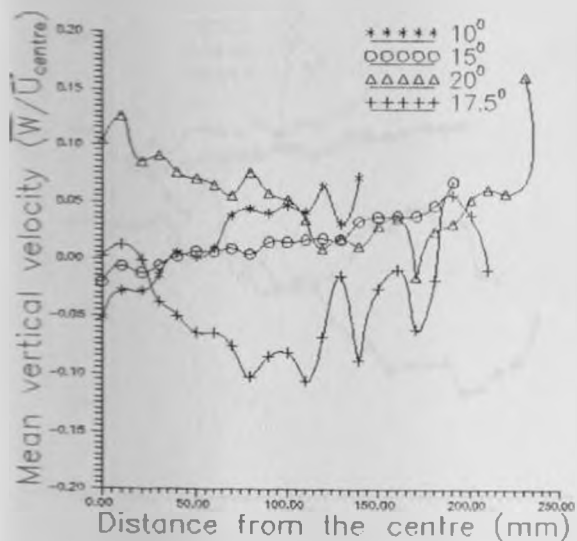


(c) At 200mm from exit

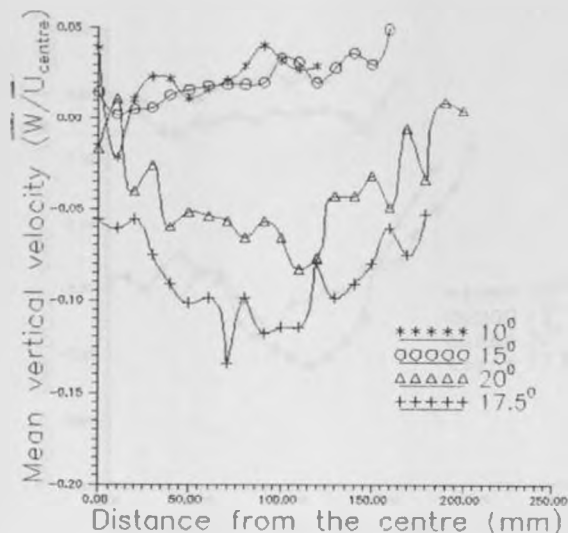


(d) At 300mm from exit

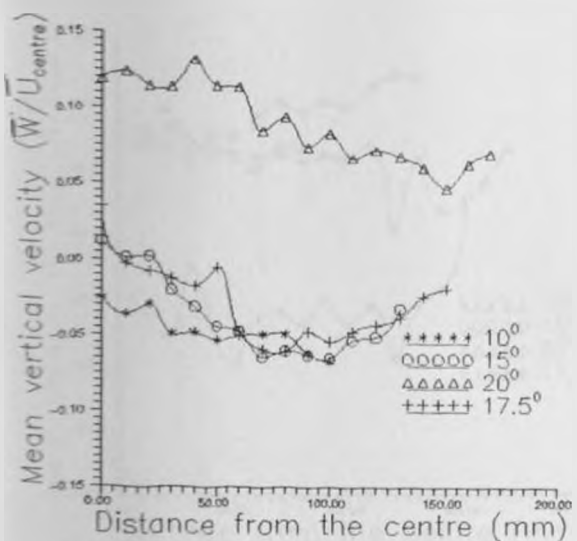
Figure 23 VERTICAL MEAN VELOCITY MEASURED ALONG A DISTANCE 60MM FROM THE WALL



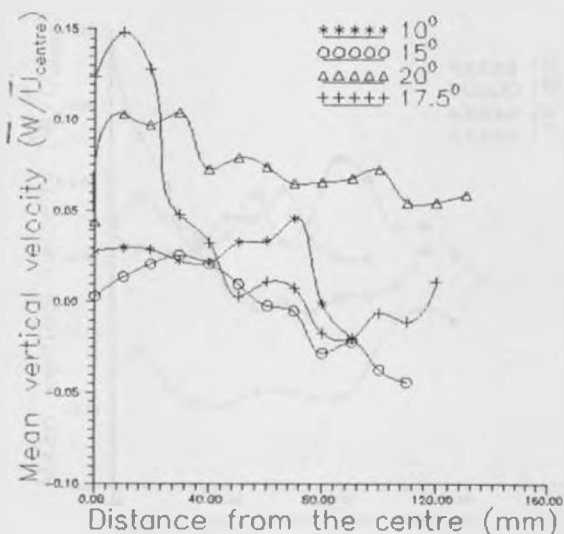
(a) At the exit plane



(b) At 100mm from the exit

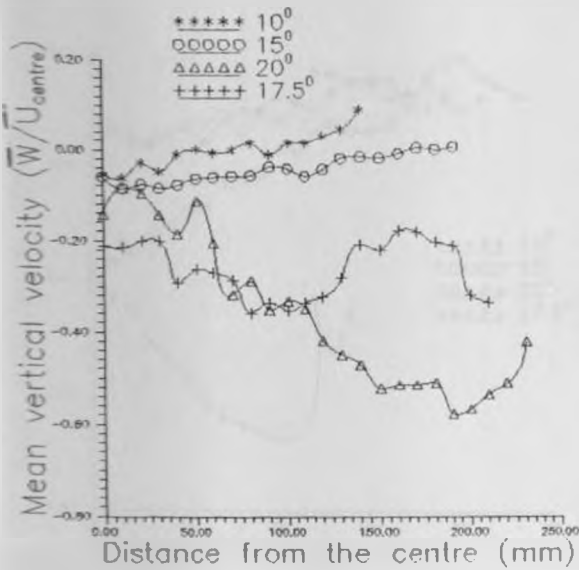


(c) At 200mm from exit

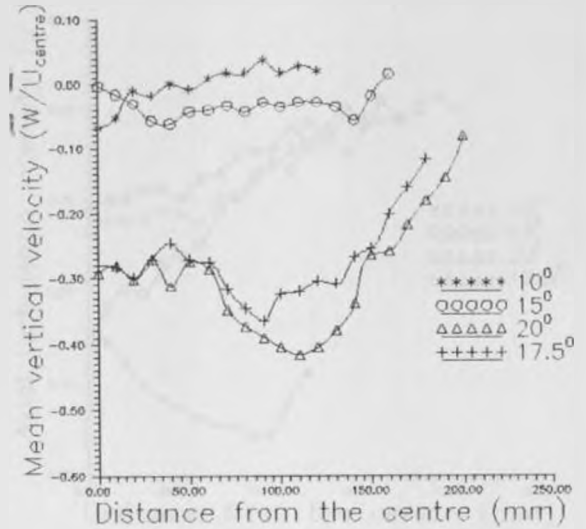


(d) At 300mm from exit

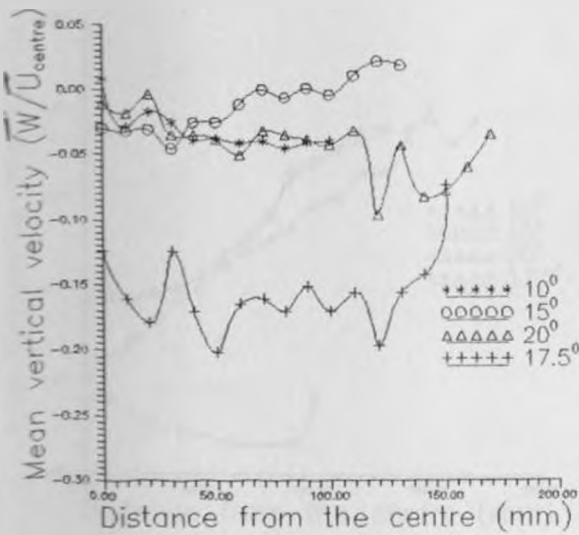
Figure 24 VERTICAL MEAN VELOCITY MEASURED ALONG A DISTANCE 20MM FROM THE WALL



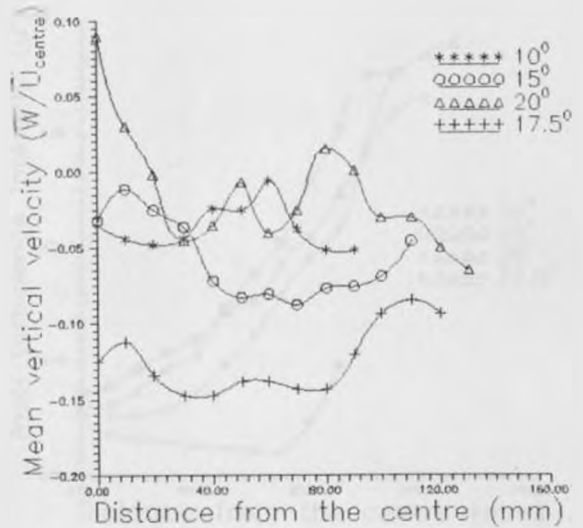
(a) At the exit plane



(b) At 100mm from the exit

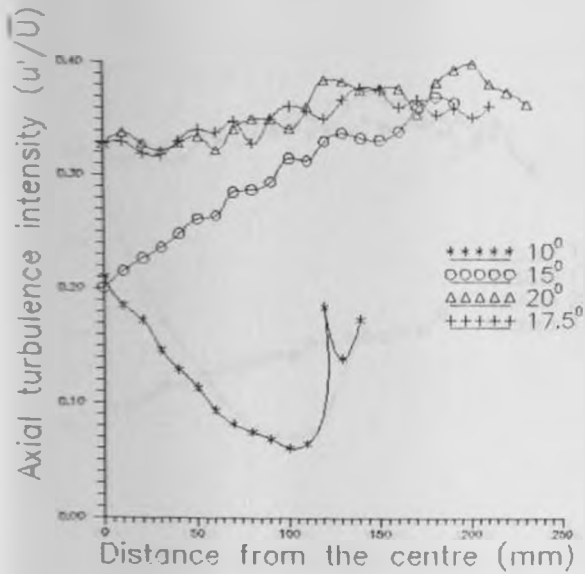


(c) At 200mm from exit

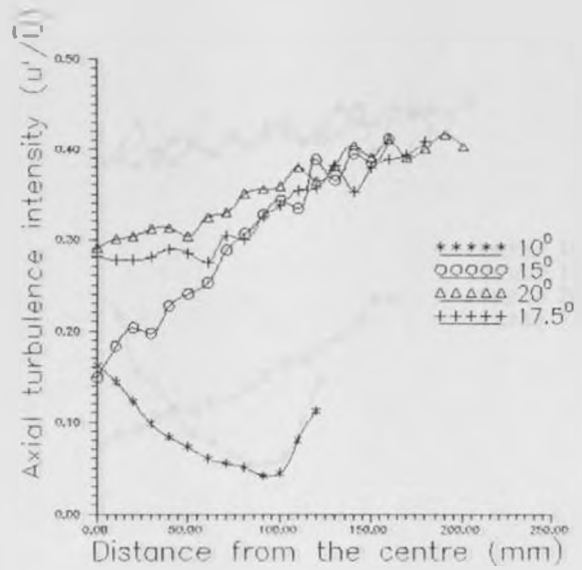


(d) At 300mm from exit

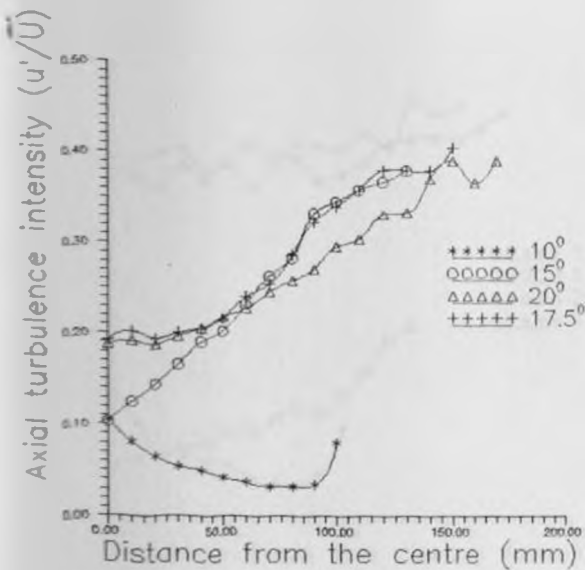
Figure 25 AXIAL TURBULENCE INTENSITY MEASURED ALONG THE CENTRELINE



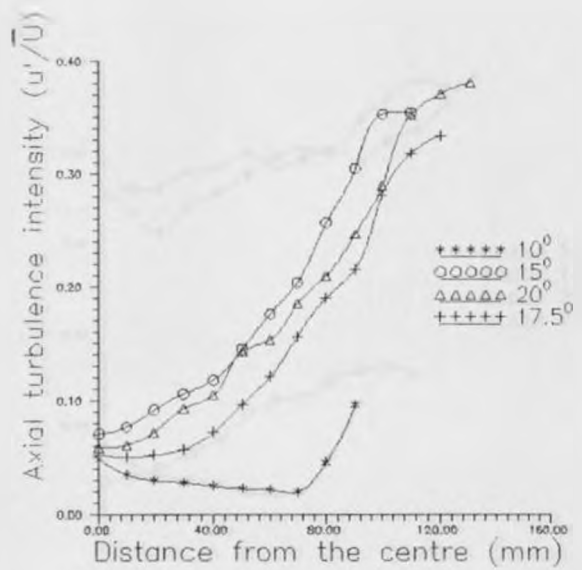
(a) At the exit plane



(b) At 100mm from the exit

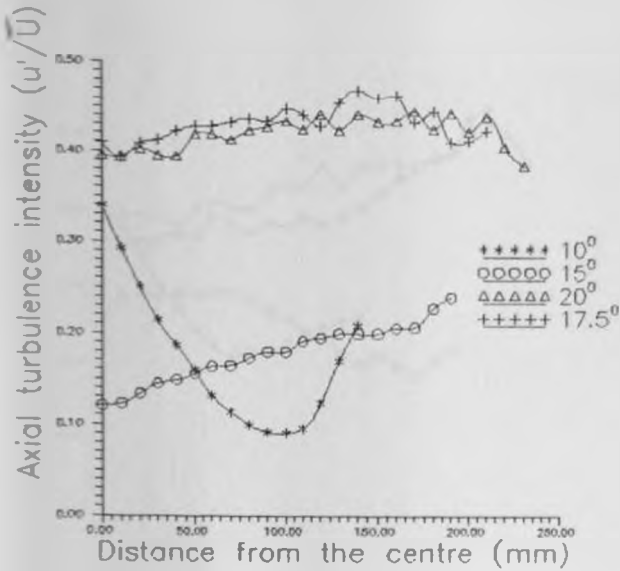


(c) At 200mm from exit

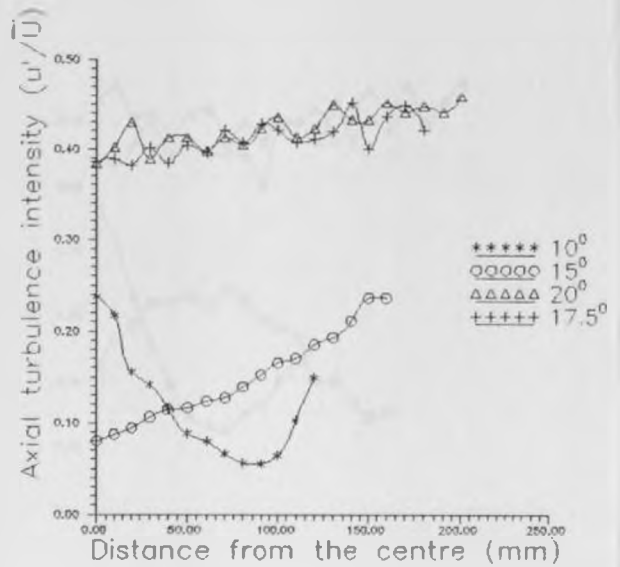


(d) At 300mm from exit

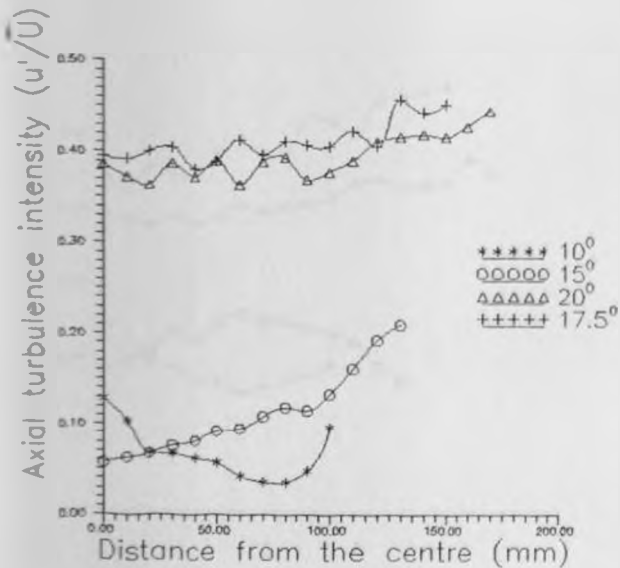
Figure 26 AXIAL TURBULENCE INTENSITY MEASURED ALONG A DISTANCE 60MM FROM THE WALL



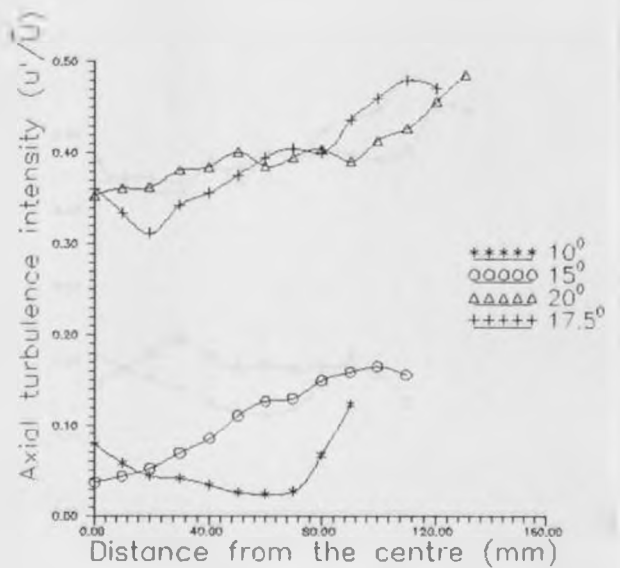
(a) At the exit plane



(b) At 100mm from the exit

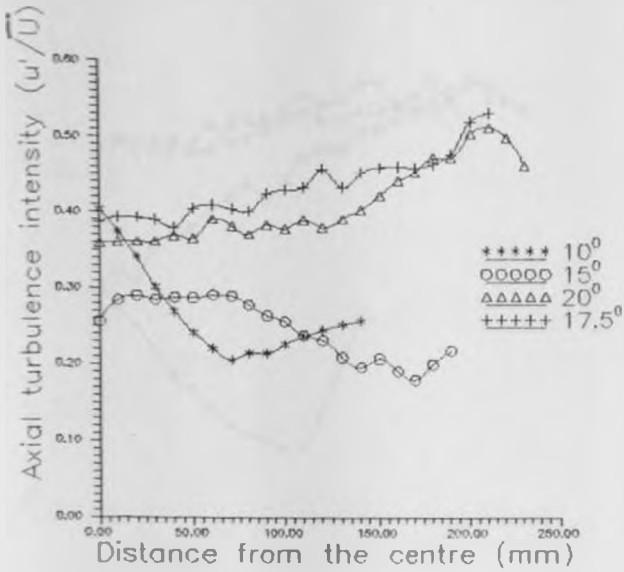


(c) At 200mm from exit

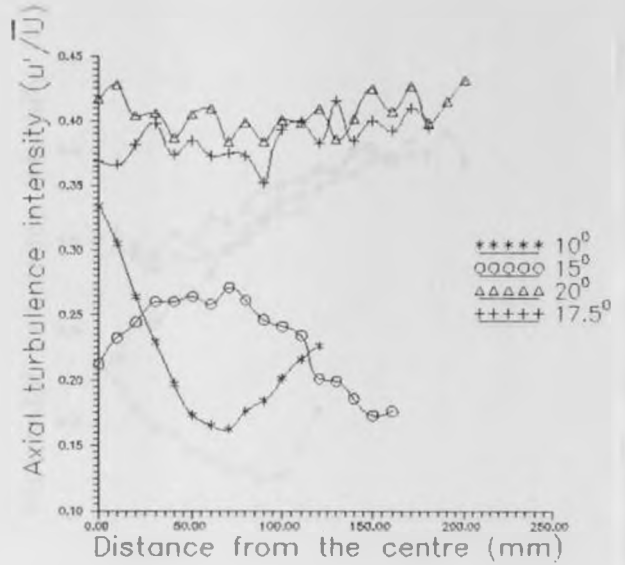


(d) At 300mm from exit

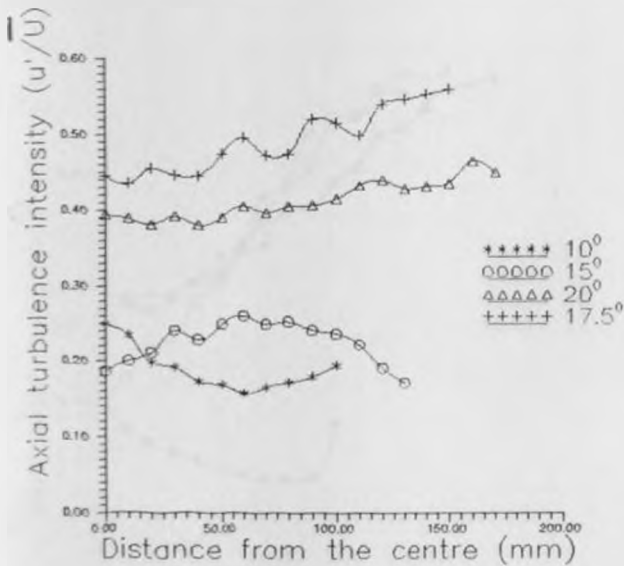
Figure 27 AXIAL TURBULENCE INTENSITY MEASURED ALONG A DISTANCE 20MM FROM THE WALL



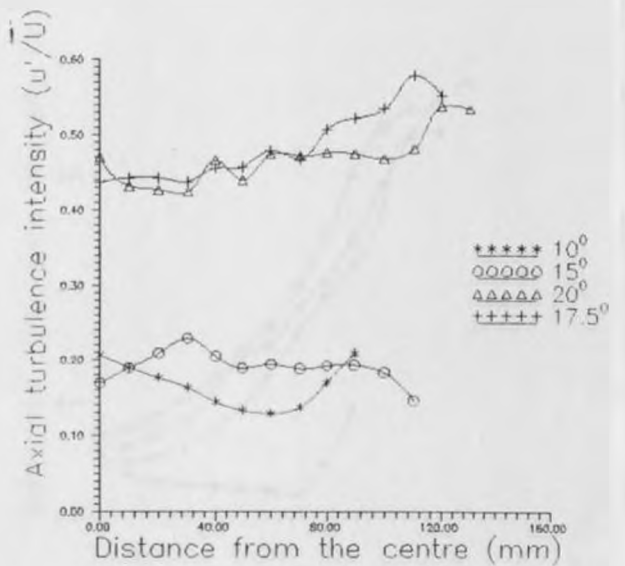
(a) At the exit plane



(b) At 100mm from the exit

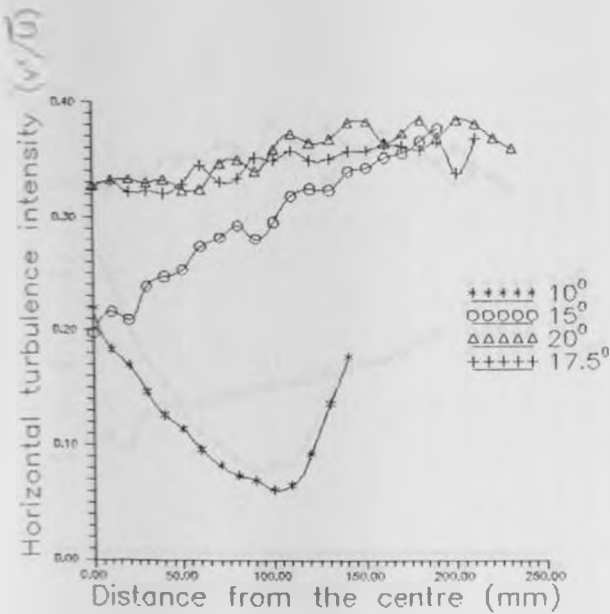


(c) At 200mm from exit

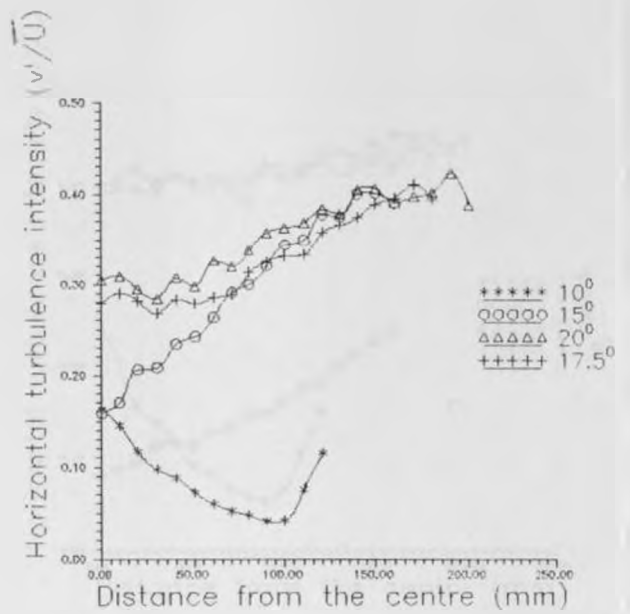


(d) At 300mm from exit

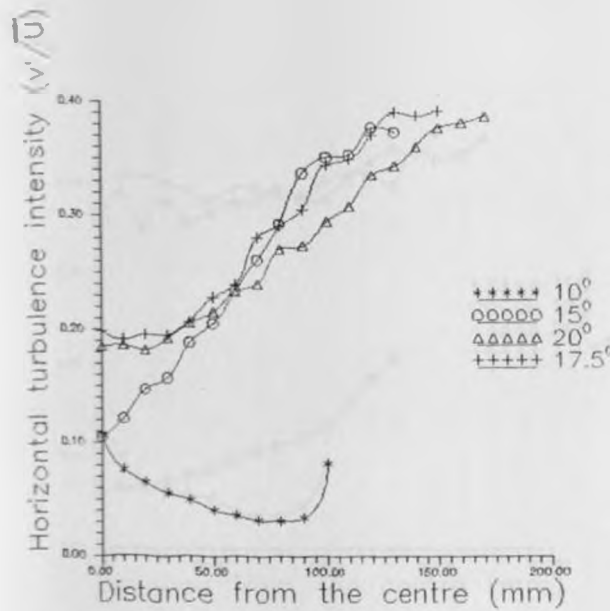
Figure 28 HORIZONTAL TURBULENCE INTENSITY MEASURED ALONG THE CENTRELINE



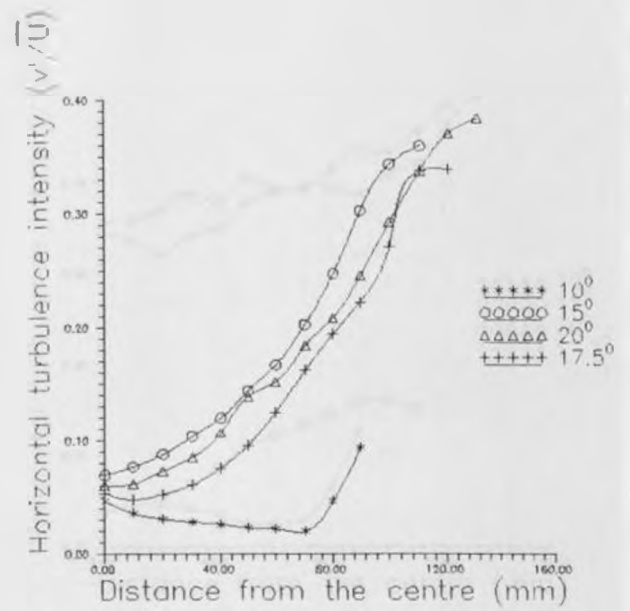
(a) At the exit plane



(b) At 100mm from the exit

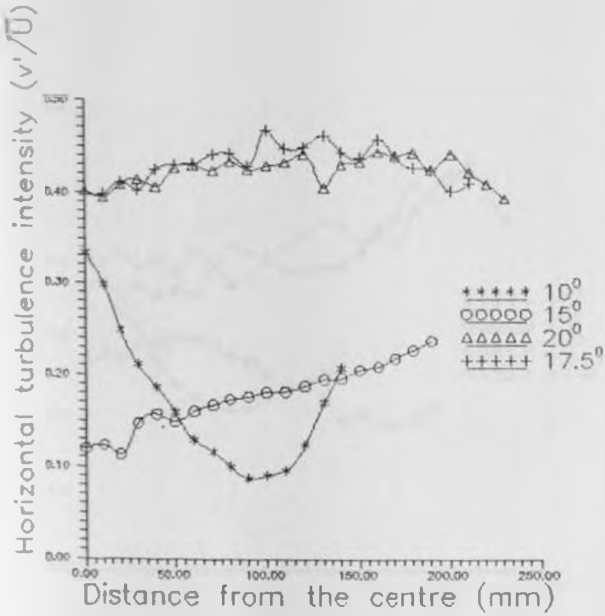


(c) At 200mm from exit

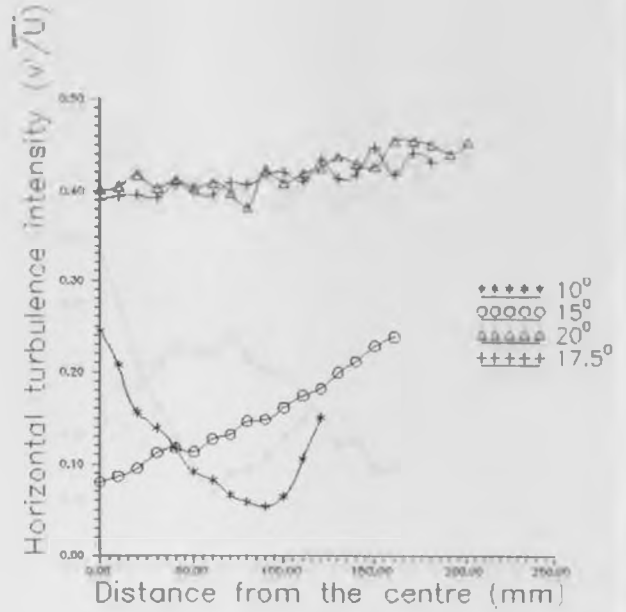


(d) At 300mm from exit

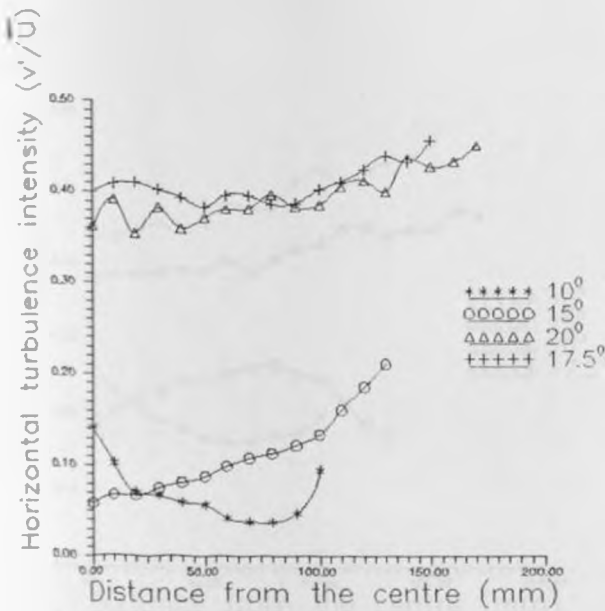
Figure 29 HORIZONTAL TURBULENCE INTENSITY MEASURED ALONG A DISTANCE 60 FROM THE WALL



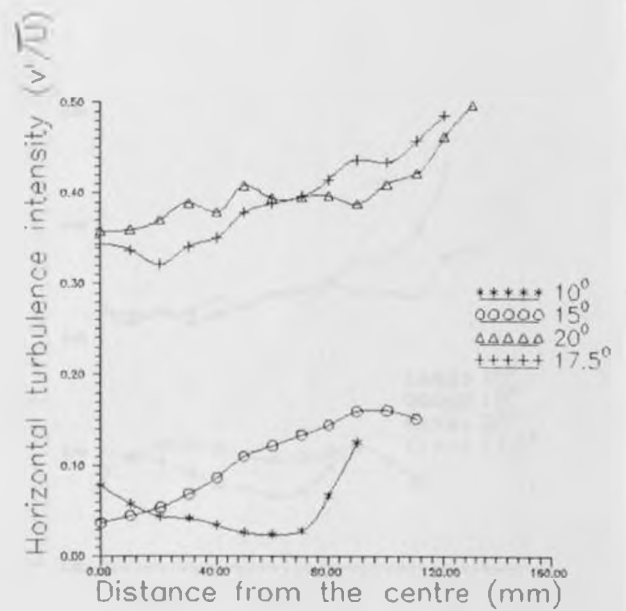
(a) At the exit plane



(b) At 100mm from the exit



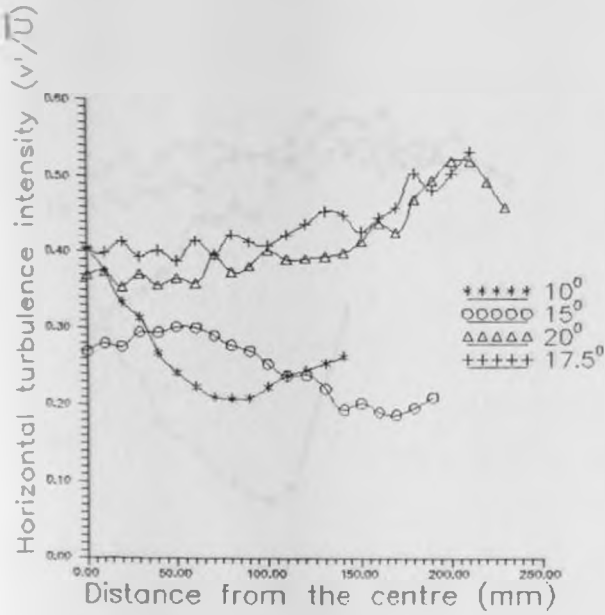
(c) At 200mm from exit



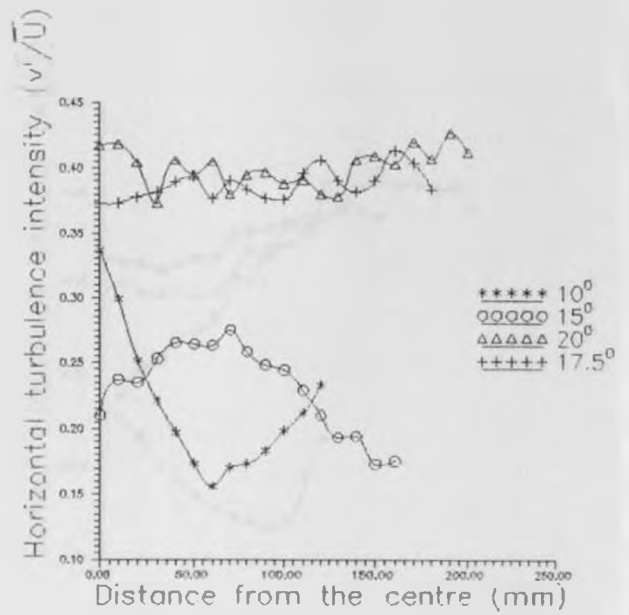
(d) At 300mm from exit



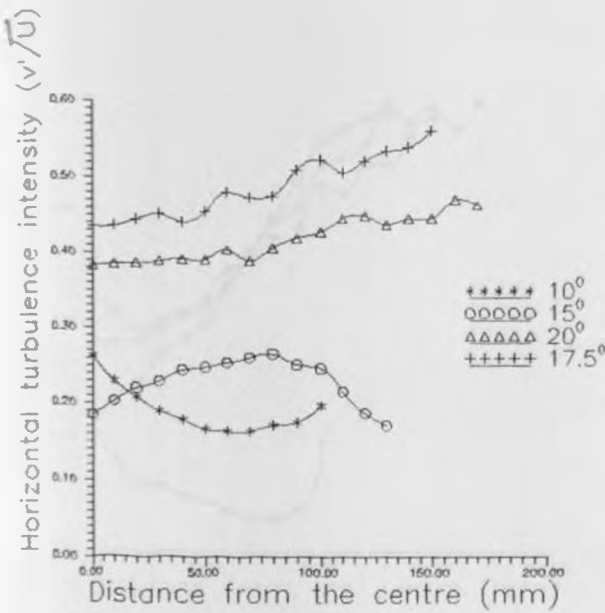
Figure 30 HORIZONTAL TURBULENCE INTENSITY MEASURED ALONG A DISTANCE 20MM FROM THE WALL



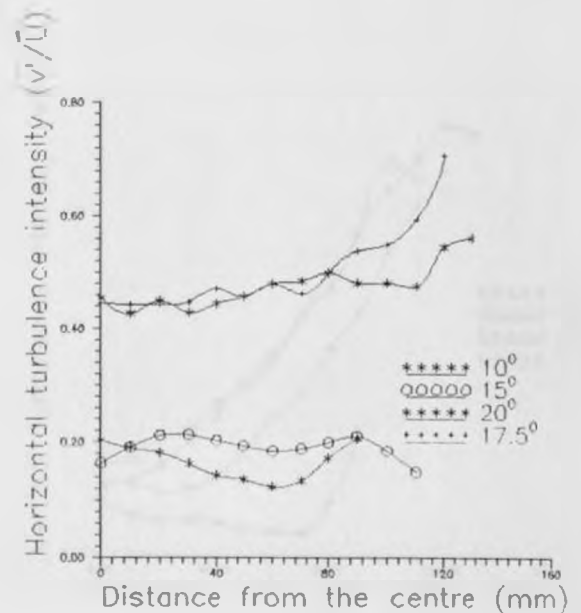
(a) At the exit plane



(b) At 100mm from the exit

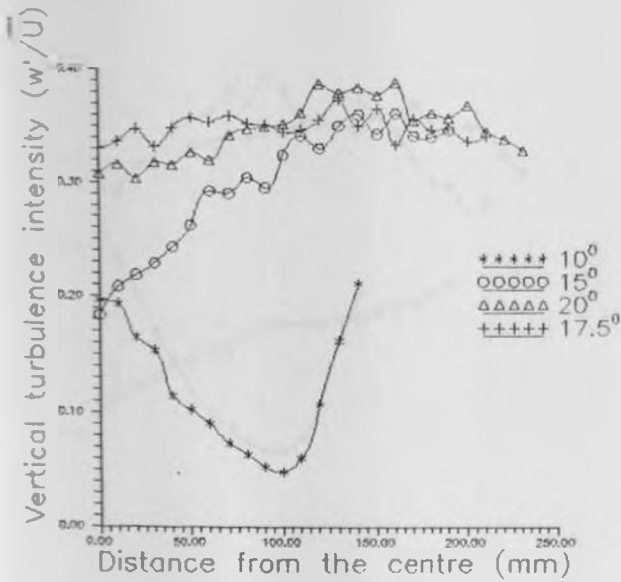


(c) At 200mm from the exit

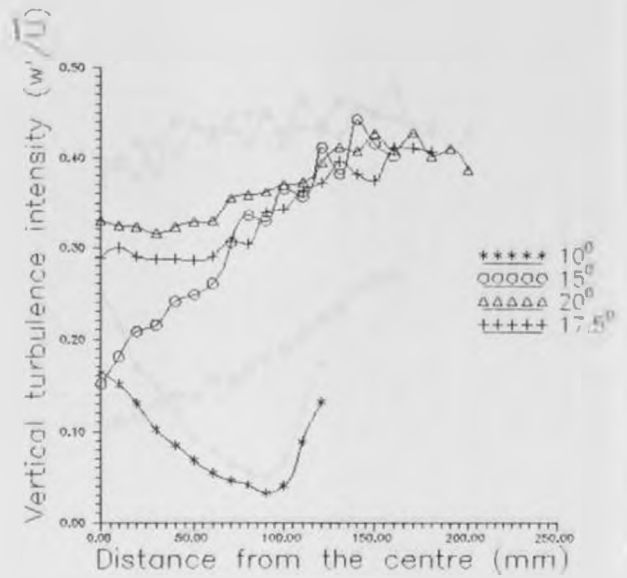


(d) At 300mm from the exit

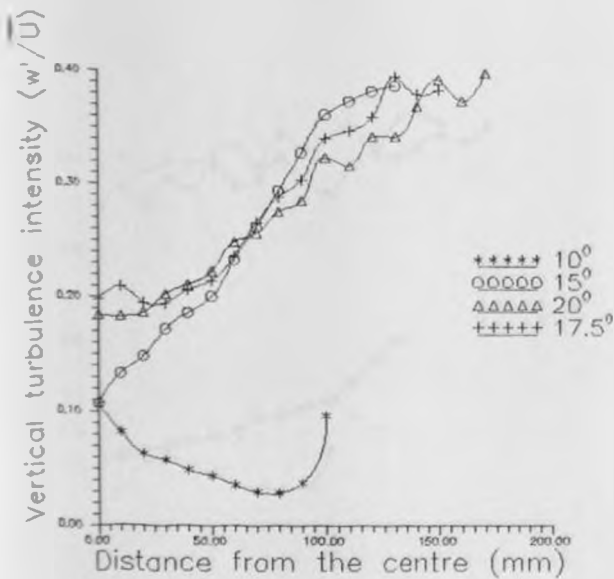
Figure 31 VERTICAL TURBULENCE INTENSITY MEASURED ALONG THE CENTRELINE



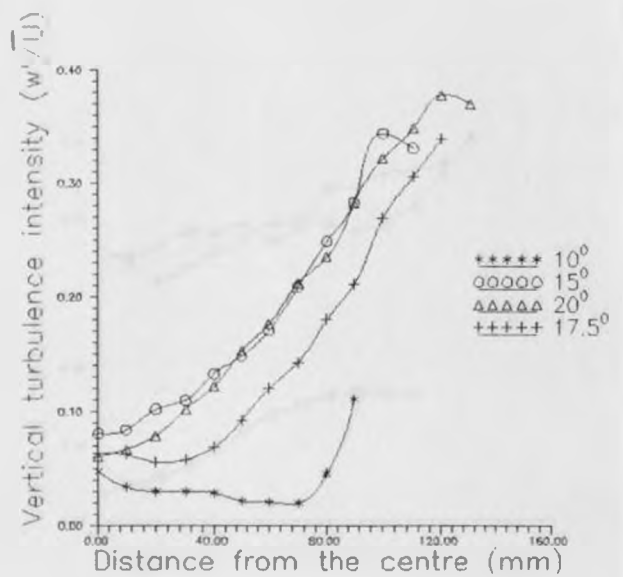
(a) At the exit plane



(b) At 100mm from the exit

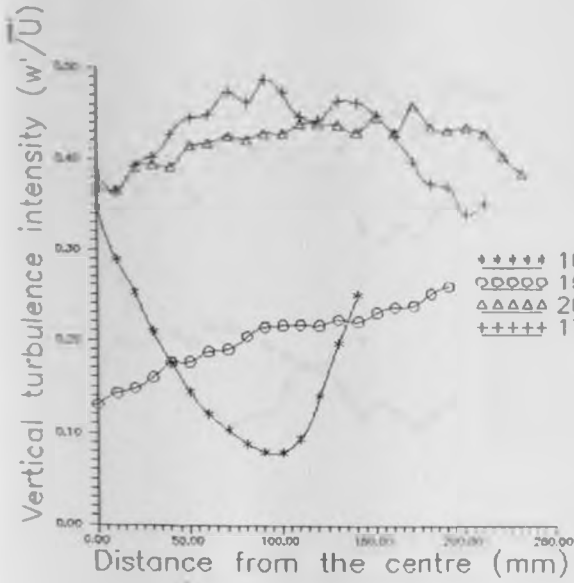


(c) At 200mm from exit

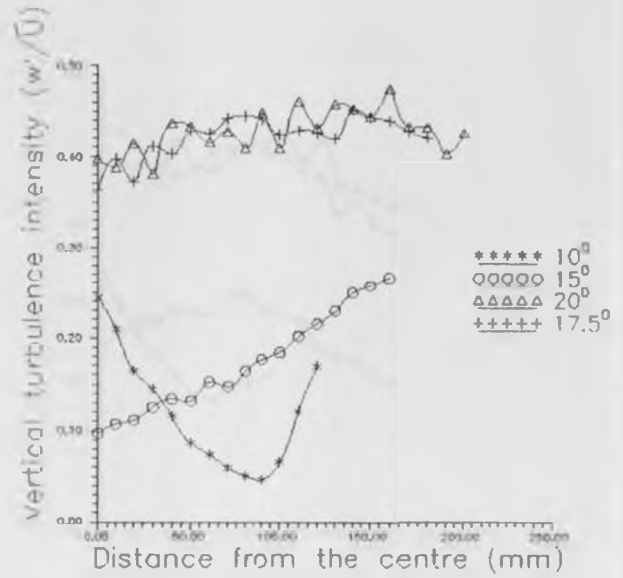


(d) At 300mm from exit

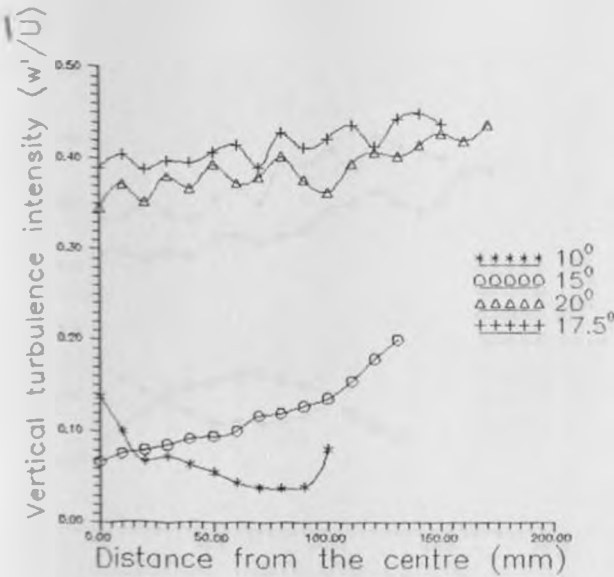
Figure 32 VERTICAL TURBULENCE INTENSITY MEASURED ALONG A DISTANCE 60MM FROM THE WALL



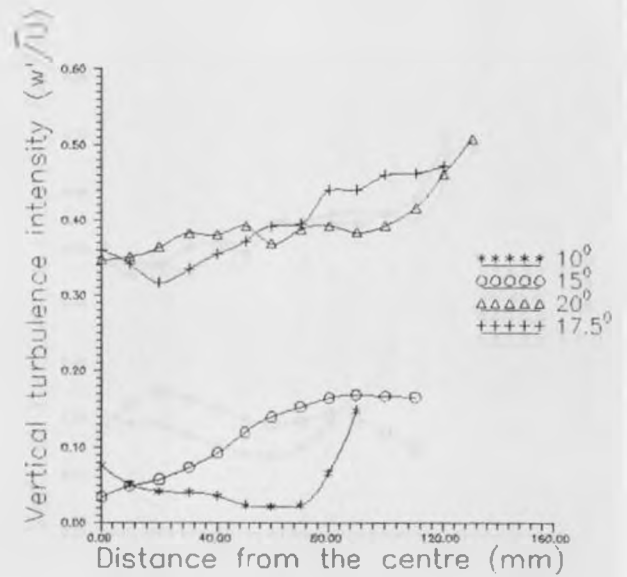
(a) At the exit plane



(b) At 100mm from the exit

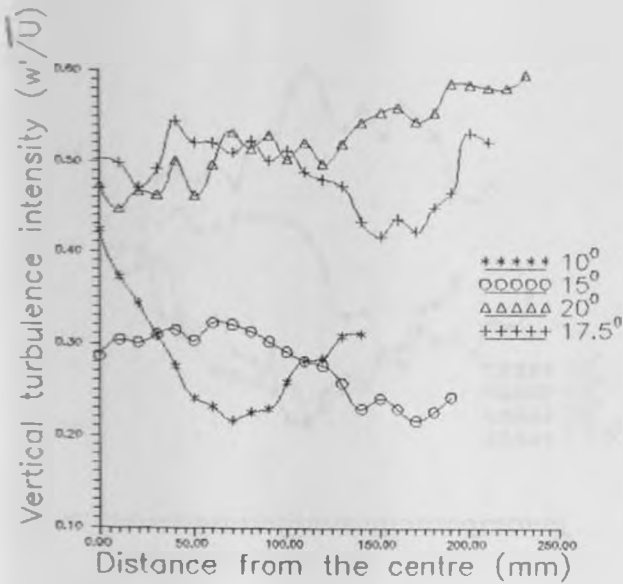


(c) At 200mm from exit

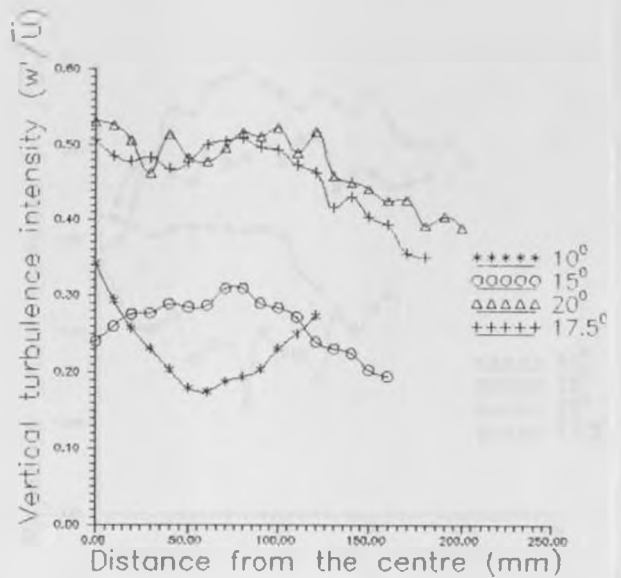


(d) At 300mm from exit

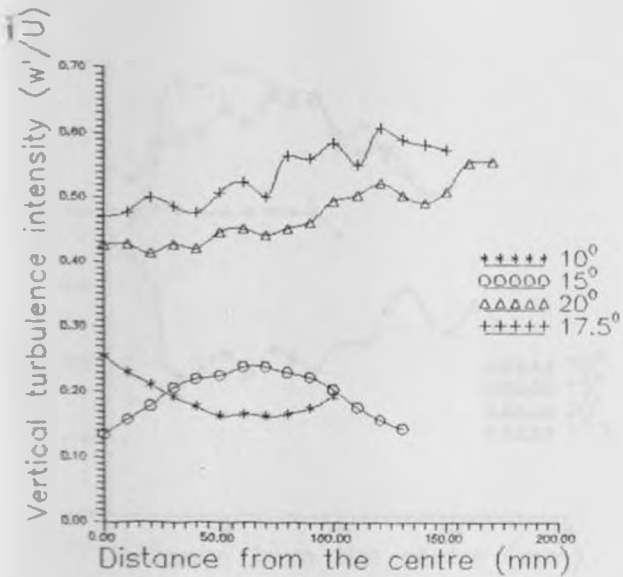
Figure 33 VERTICAL TURBULENCE INTENSITY MEASURED ALONG A DISTANCE 20MM FROM THE WALL



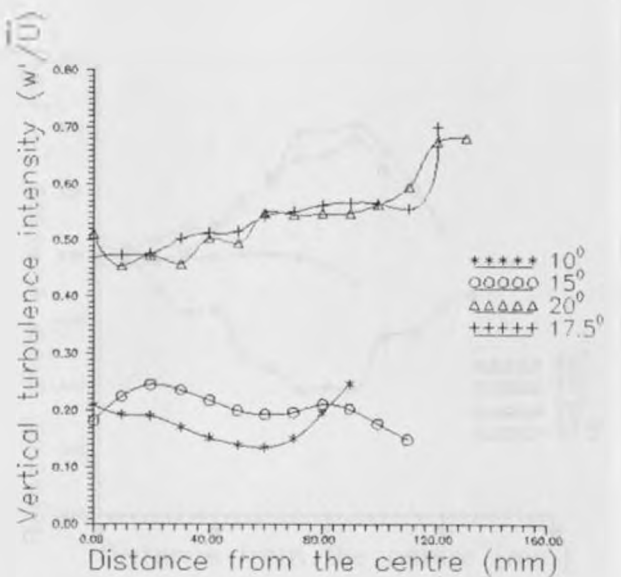
(a) At the exit plane



(b) At 100mm from the exit

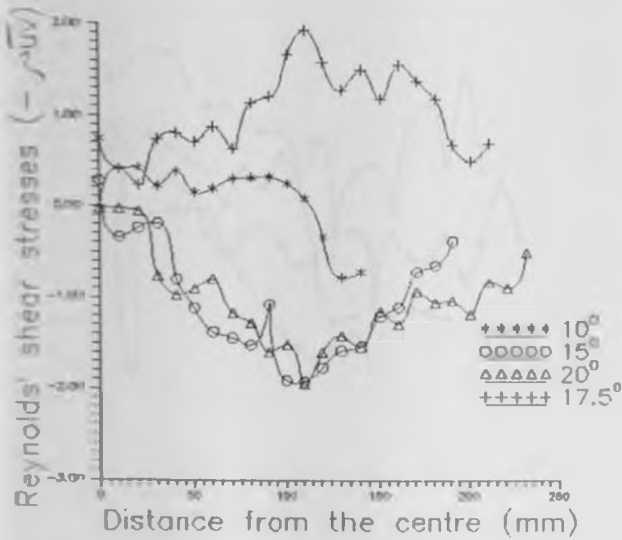


(c) At 200mm from exit

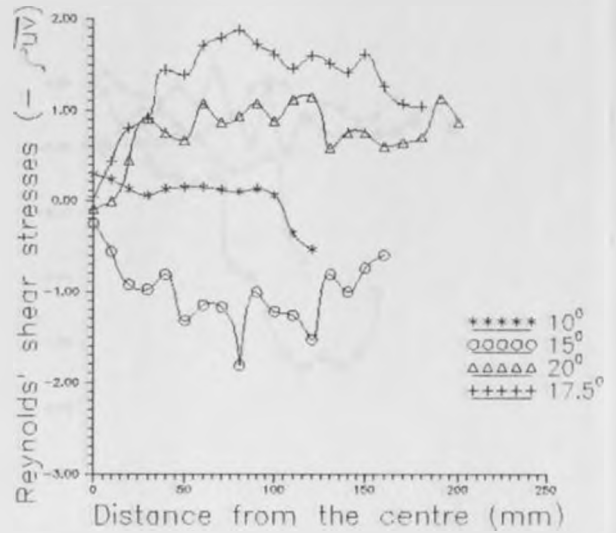


(d) At 300mm from exit

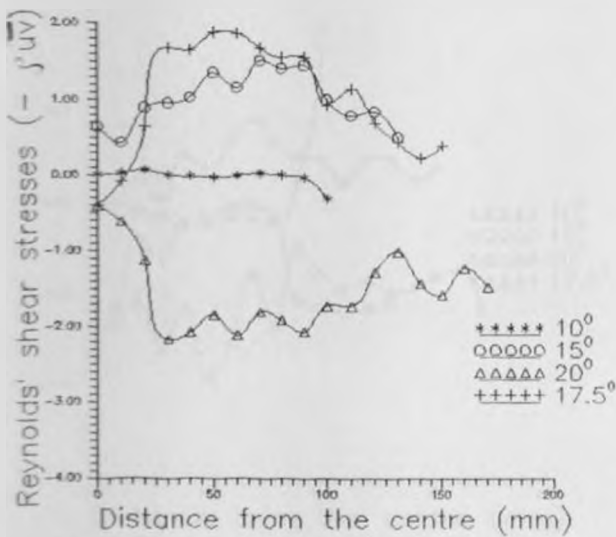
Figure 34 REYNOLD'S SHEAR STRESSES ( $-\int \overline{uv}$ ) MEASURED ALONG THE CENTRELINE



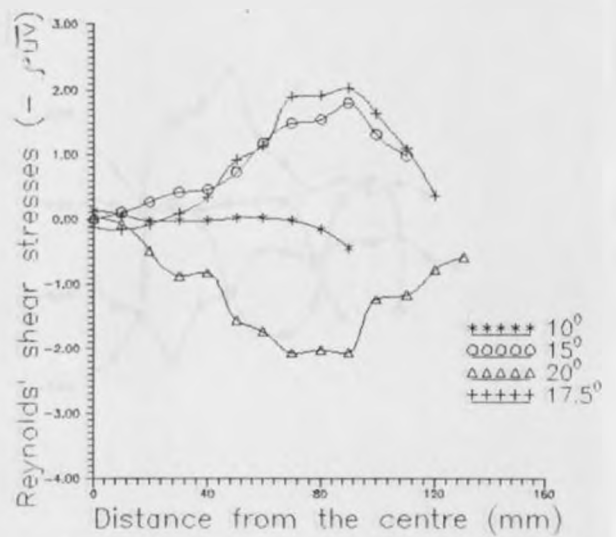
(a) At the exit plane



(b) At 100mm from the exit



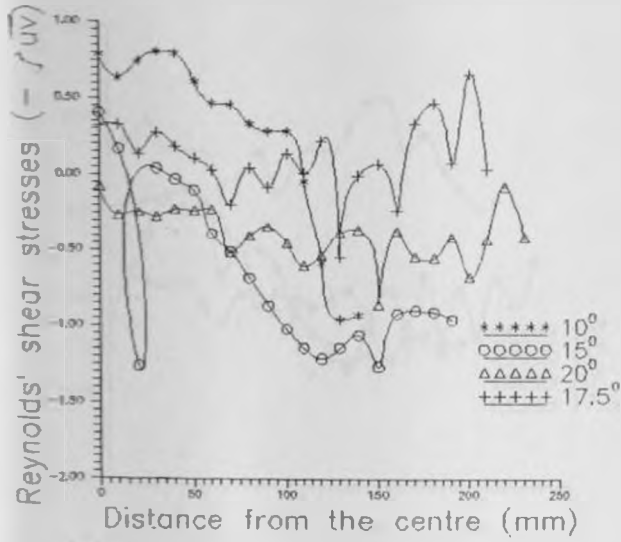
(c) At 200mm from exit



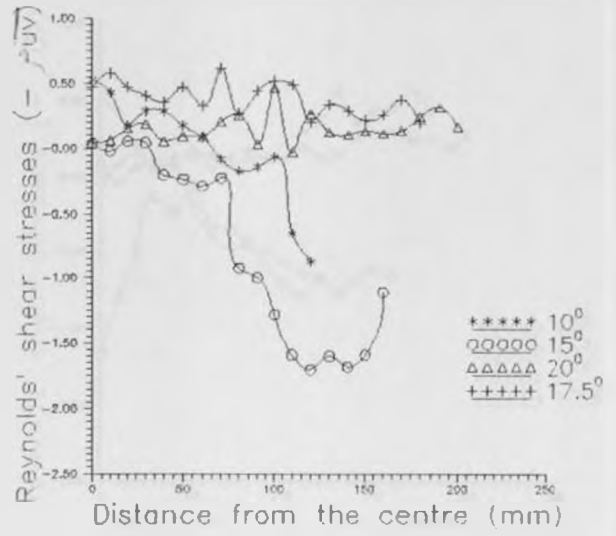
(d) At 300mm from exit

Figure 35

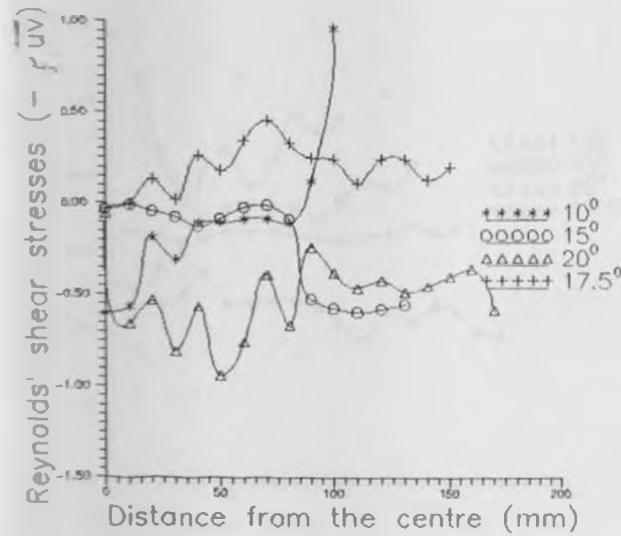
REYNOLD'S SHEAR STRESSES ( $-\tau_{uv}$ )  
MEASURED ALONG A DISTANCE 60MM FROM THE WALL



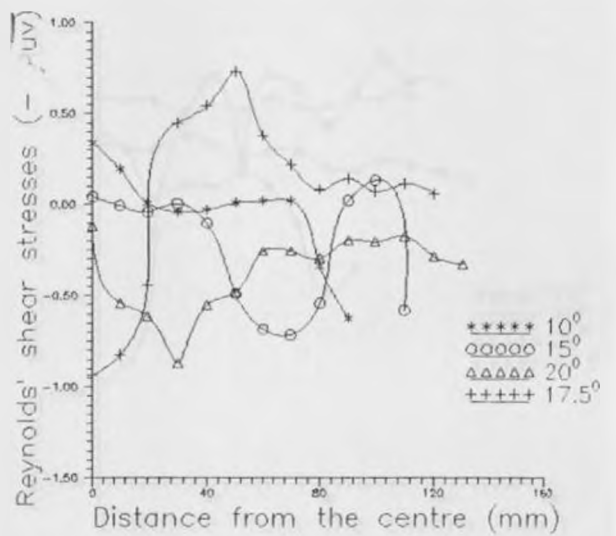
(a) At the exit plane



(b) At 100mm from the exit



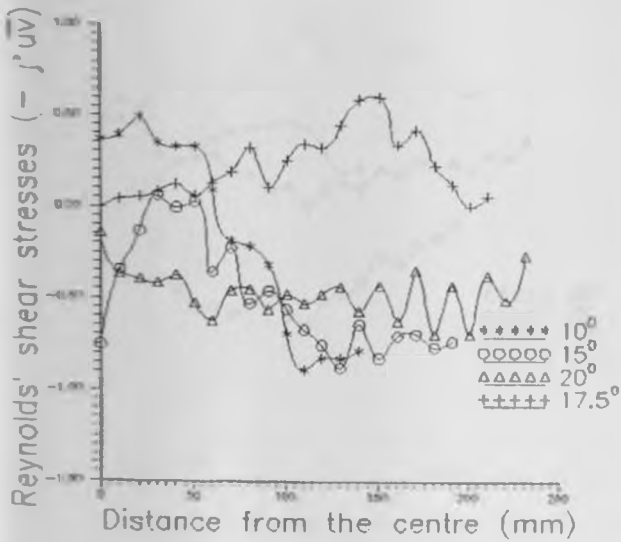
(c) At 200mm from exit



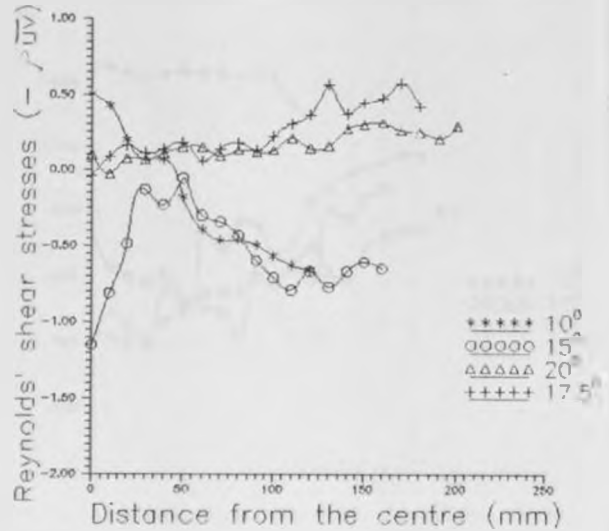
(d) At 300mm from exit

Figure 36

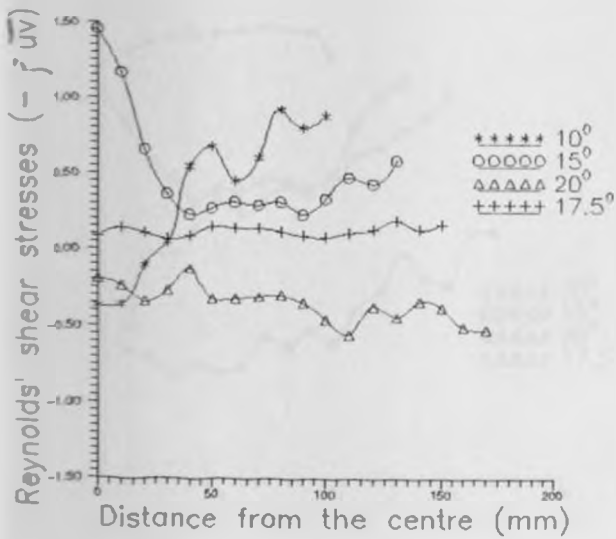
REYNOLD'S SHEAR STRESSES ( $-\rho \overline{uv}$ )  
 MEASURED ALONG A DISTANCE 20MM FROM  
 THE WALL



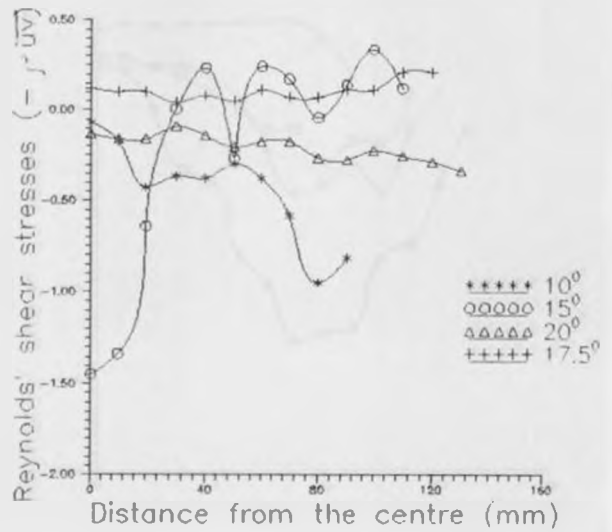
(a) At the exit plane



(b) At 100mm from the exit

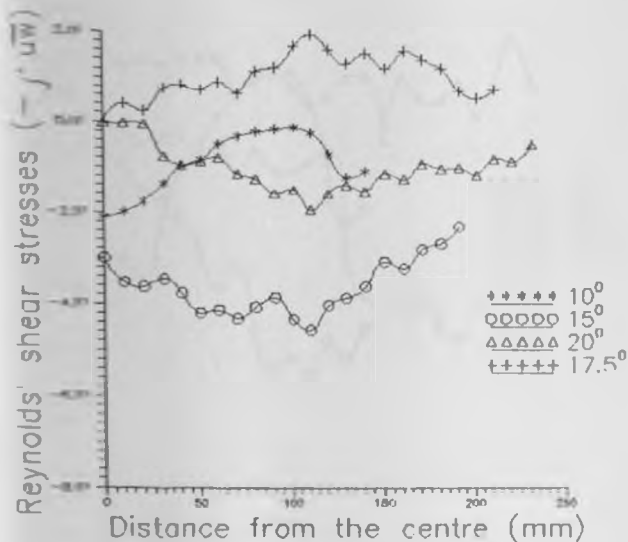


(c) At 200mm from exit

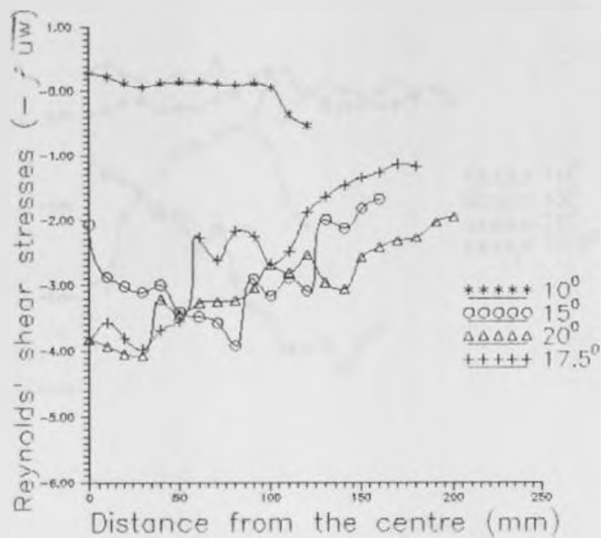


(d) At 300mm from exit

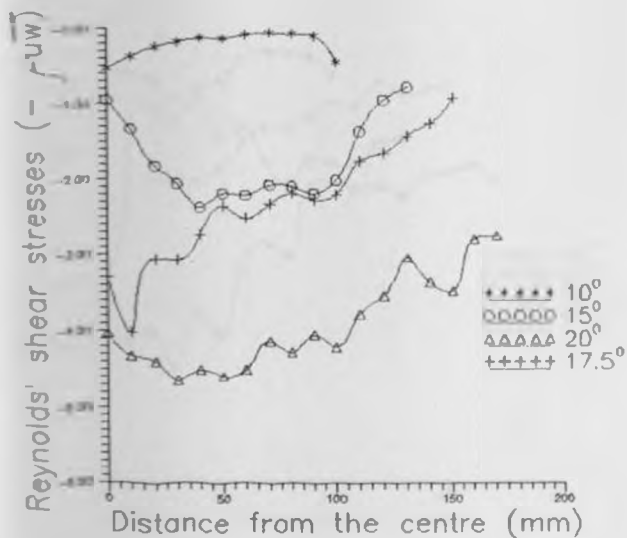
Figure 37 REYNOLD'S SHEAR STRESSES ( $-\rho \overline{uw}$ ) MEASURED ALONG THE CENTRELINE



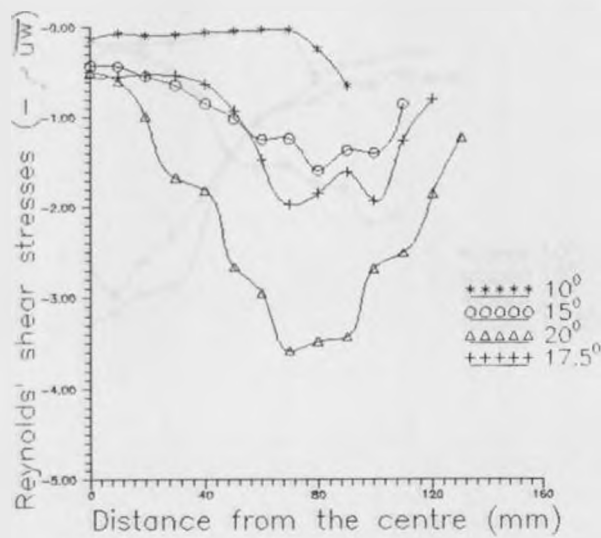
(a) At the exit plane



(b) At 100mm from the exit



(c) At 200mm from exit

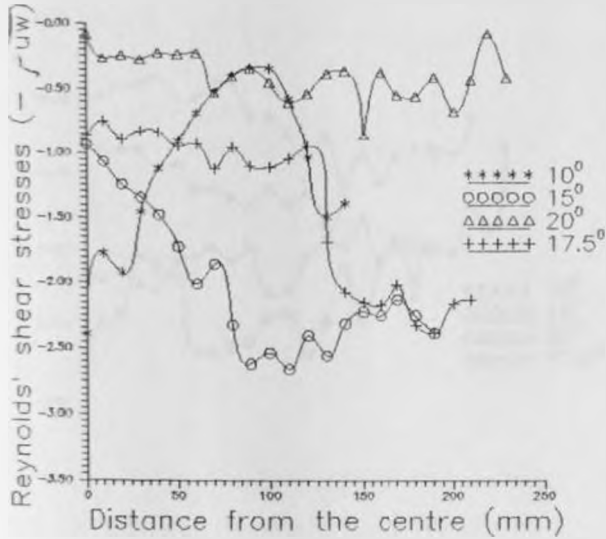


(d) At 300mm from exit

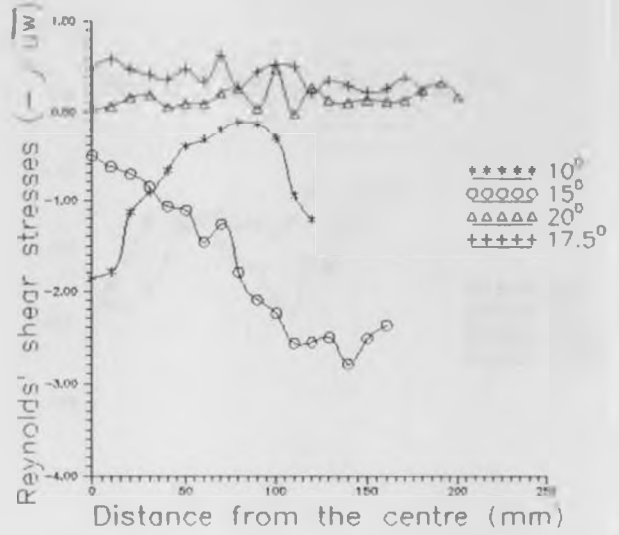


Figure 38

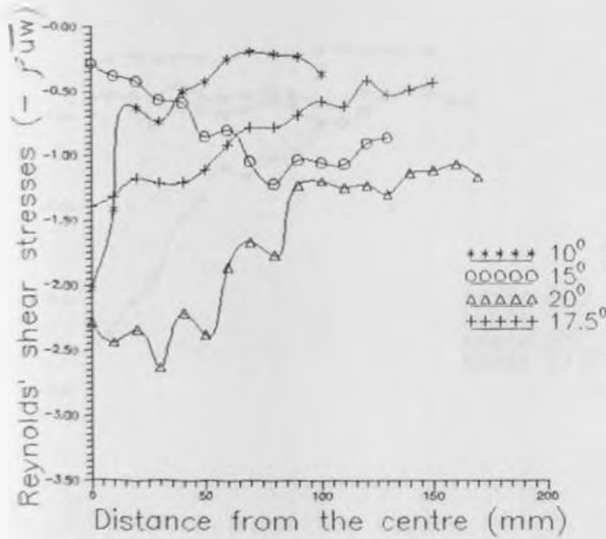
REYNOLD'S SHEAR STRESSES ( $-\tau / \overline{uw}$ )  
 MEASURED ALONG A DISTANCE 60MM FROM  
 THE WALL



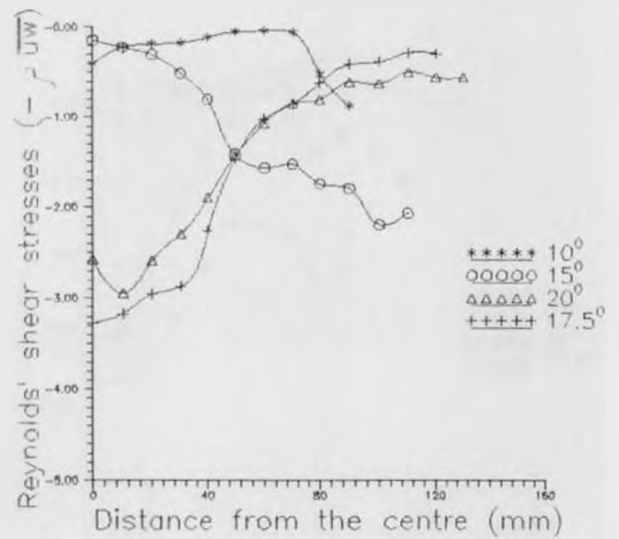
(a) At the exit plane



(b) At 100mm from the exit

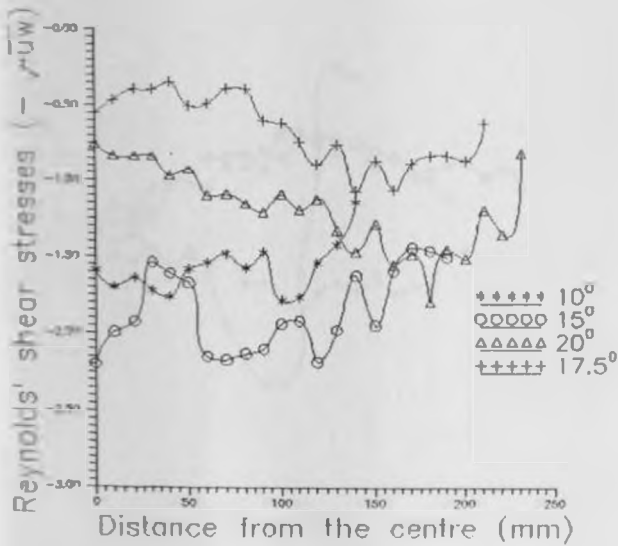


(c) At 200mm from exit

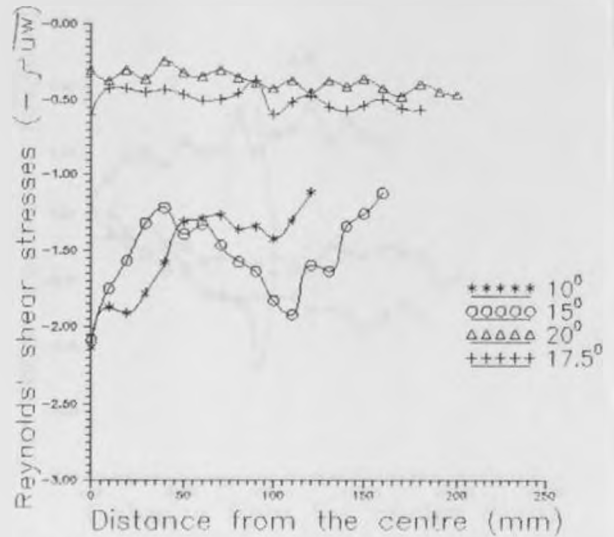


(d) At 300mm from the exit

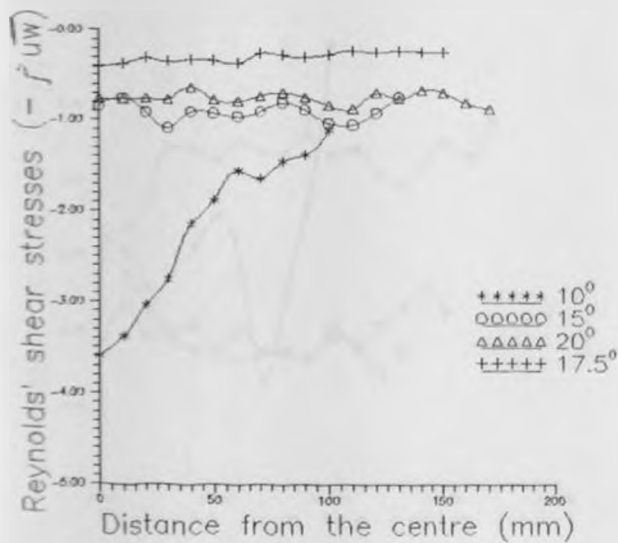
Figure 39 REYNOLD'S SHEAR STRESSES ( $-\overline{j'uw}$ ) MEASURED ALONG A DISTANCE 20MM FROM THE WALL



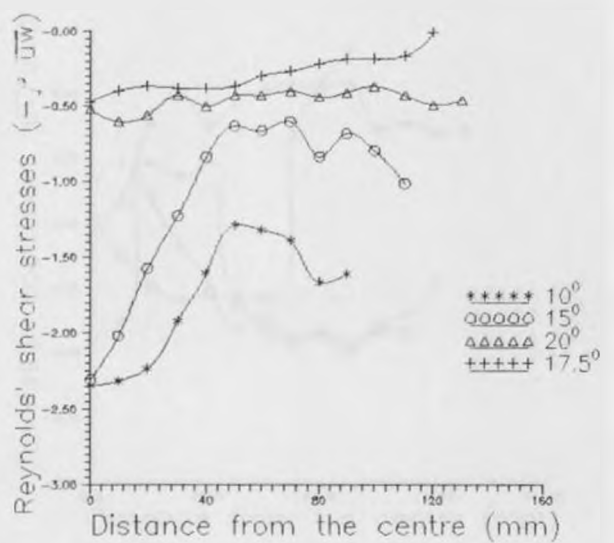
(a) At the exit plane



(b) At 100mm from the exit

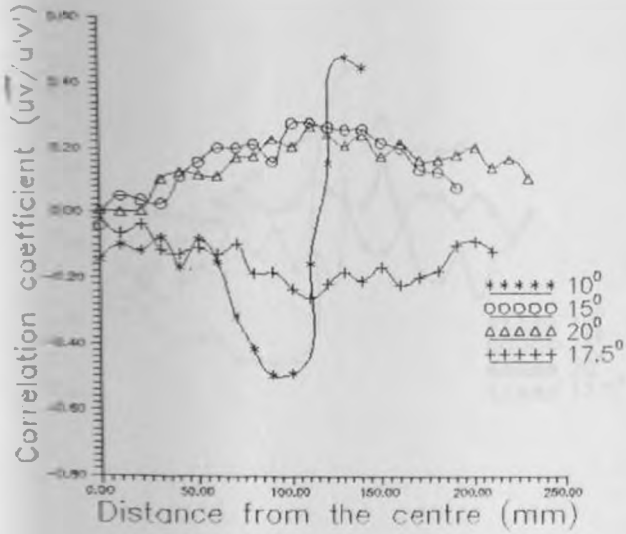


(c) At 200mm from exit

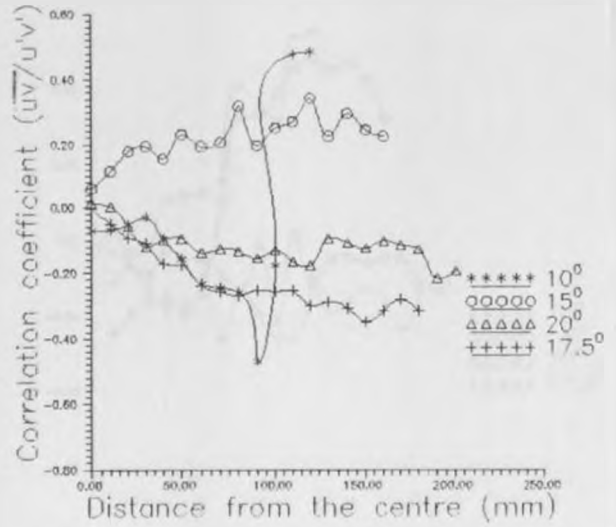


(d) At 300mm from exit

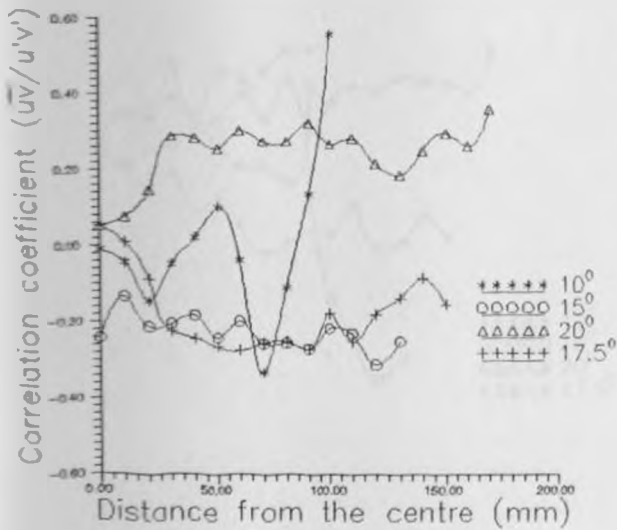
Figure 40 CORRELATION COEFFICIENT ( $\overline{uv}/u'v'$ ) MEASURED ALONG THE CENTRELINE



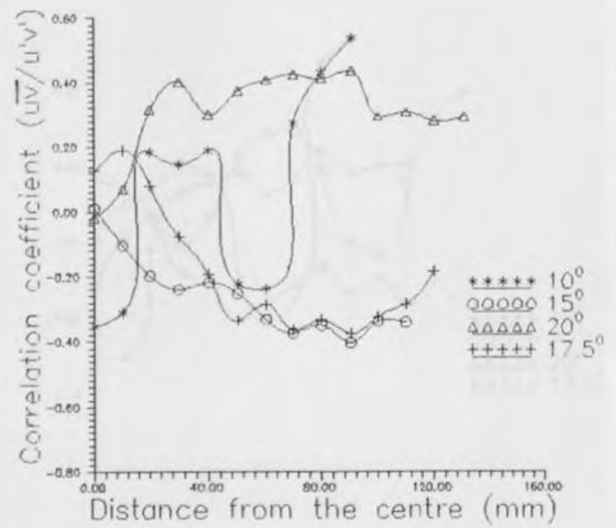
(a) At the exit plane



(b) At 100mm from the exit



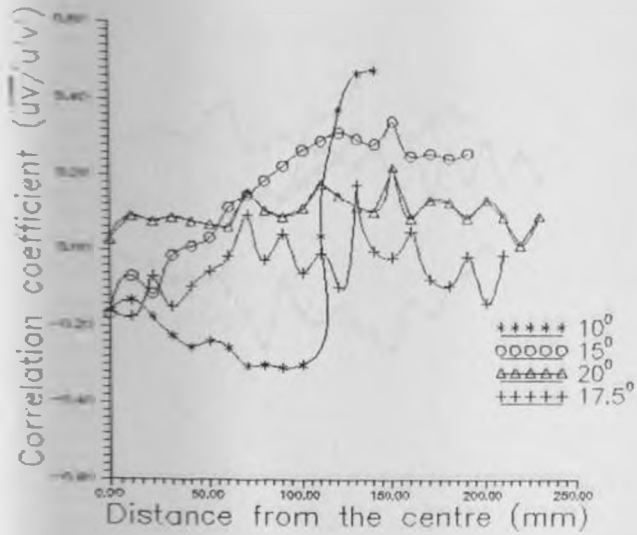
(c) At 200mm from exit



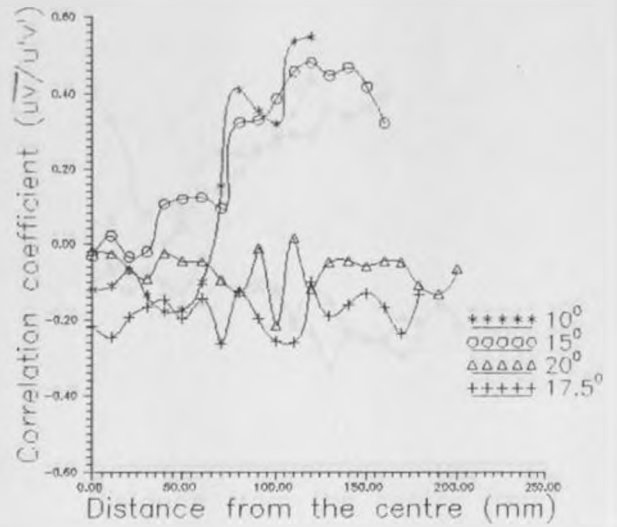
(d) At 300mm from exit

Figure 41

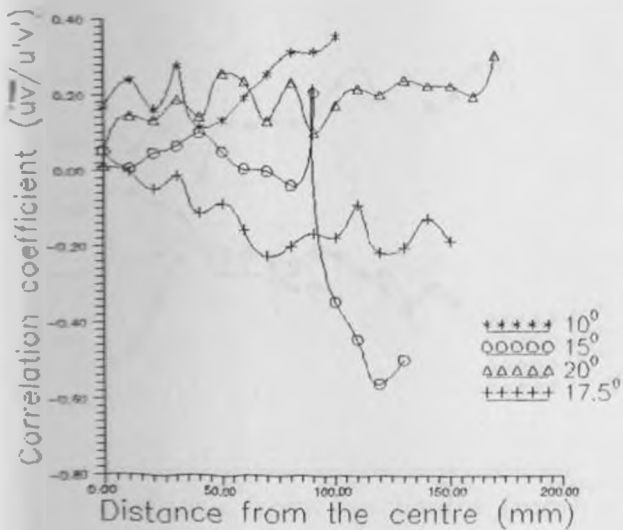
CORRELATION COEFFICIENT ( $\overline{uv}/u'v'$ )  
MEASURED ALONG A DISTANCE 60MM FROM  
THE WALL



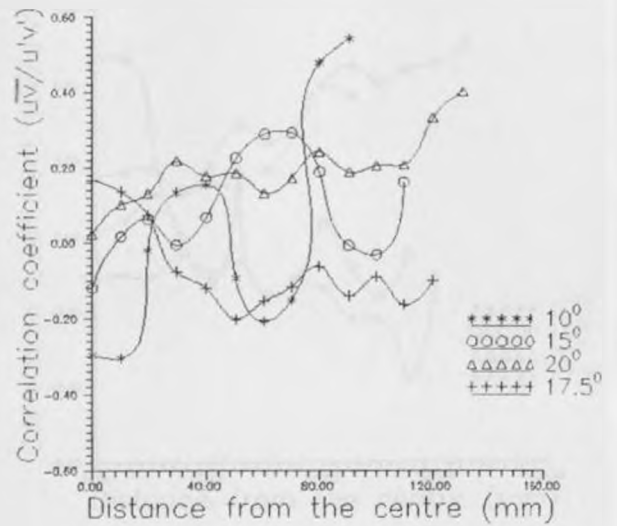
(a) At the exit plane



(b) At 100mm from the exit



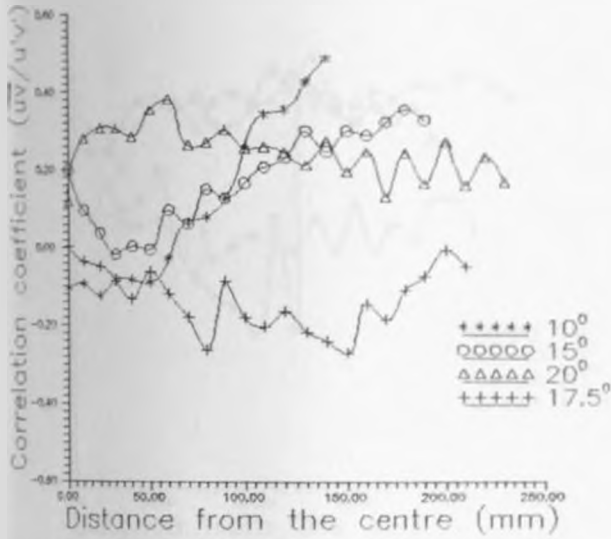
(c) At 200mm from exit



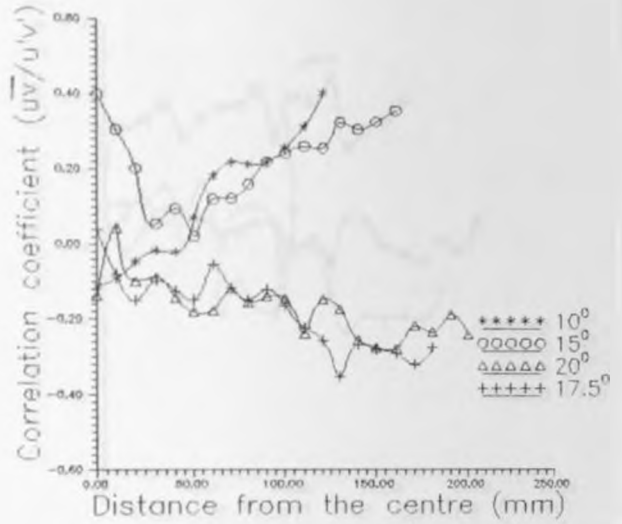
(d) At 300mm from exit

Figure 42

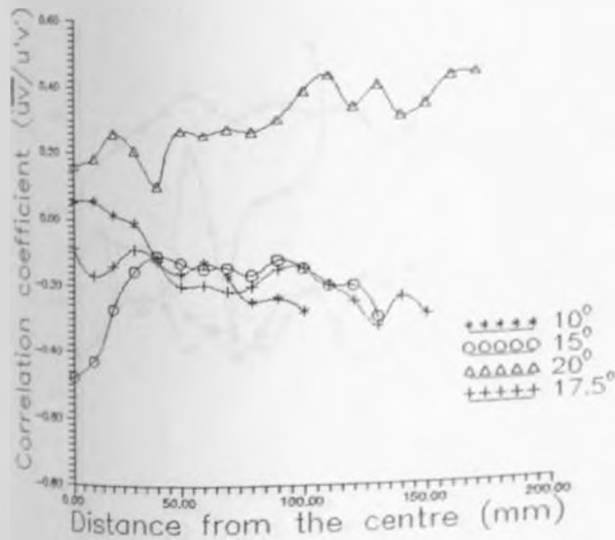
CORRELATION COEFFICIENT ( $\overline{uv}/u'v'$ )  
MEASURED ALONG A DISTANCE 20MM FROM  
THE WALL



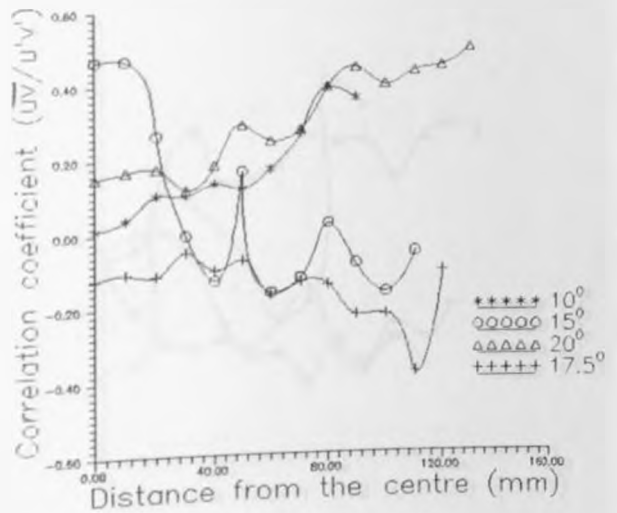
(a) At the exit plane



(b) At 100mm from the exit

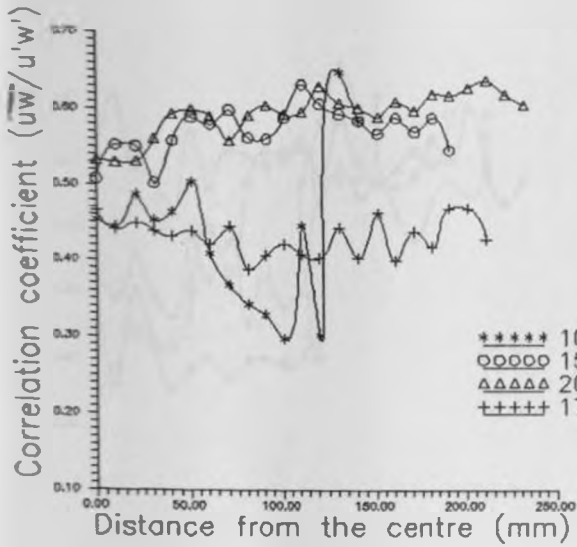


(c) At 200mm from exit

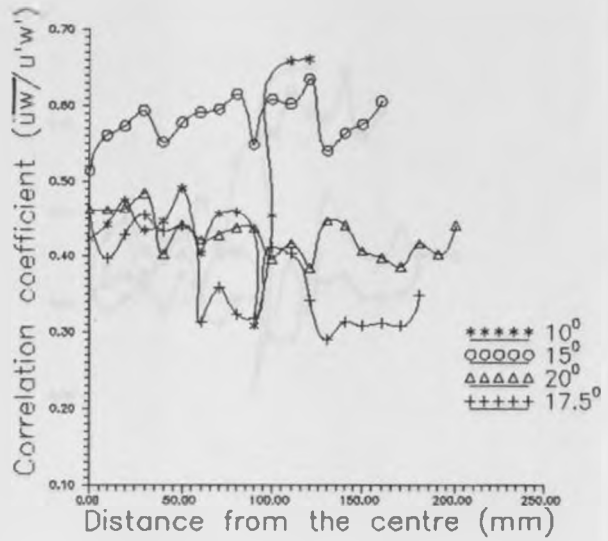


(d) At 300mm from exit

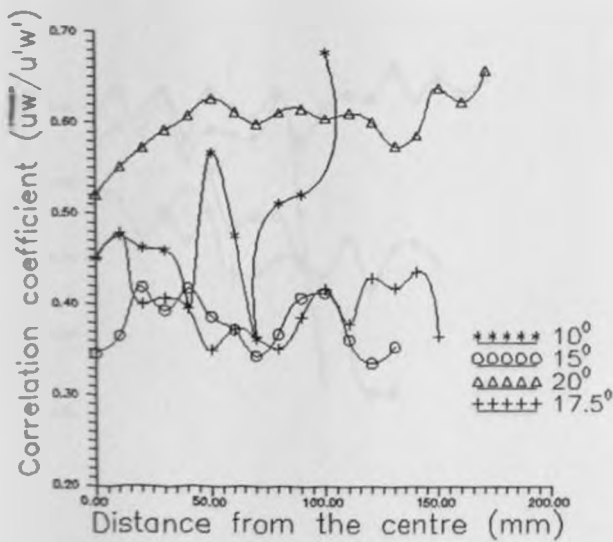
Figure 43 CORRELATION COEFFICIENT ( $\overline{uw}/u'w'$ ) MEASURED ALONG THE CENTRE LINE



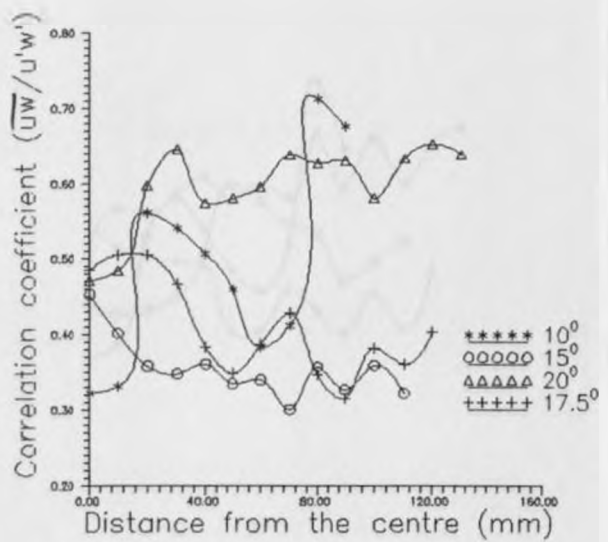
(a) At the exit plane



(b) At 100mm from the exit

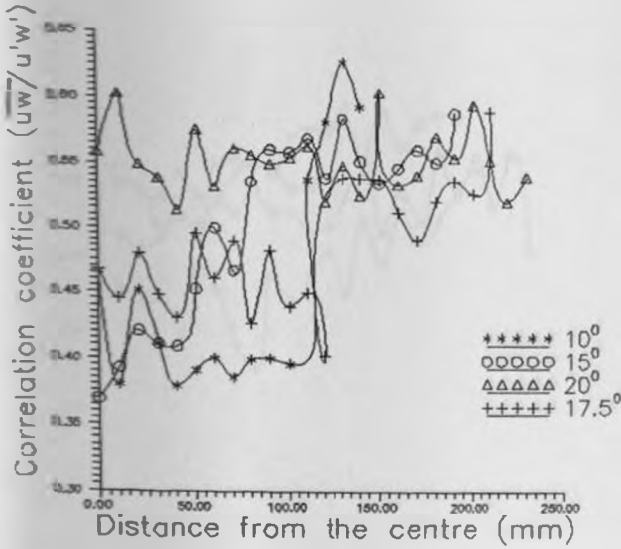


(c) At 200mm from exit

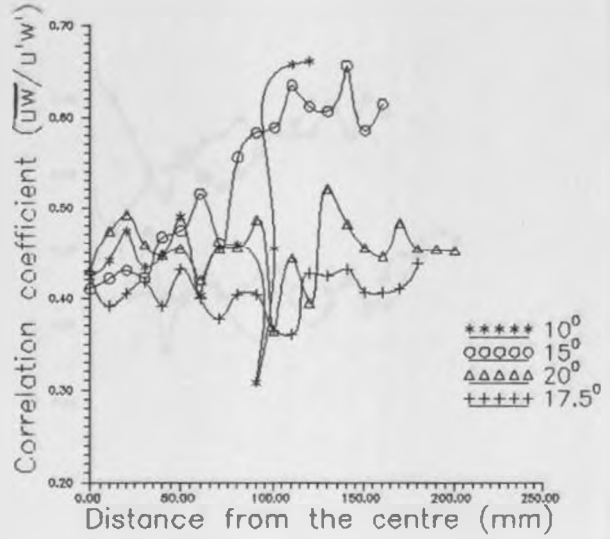


(d) At 300mm from exit

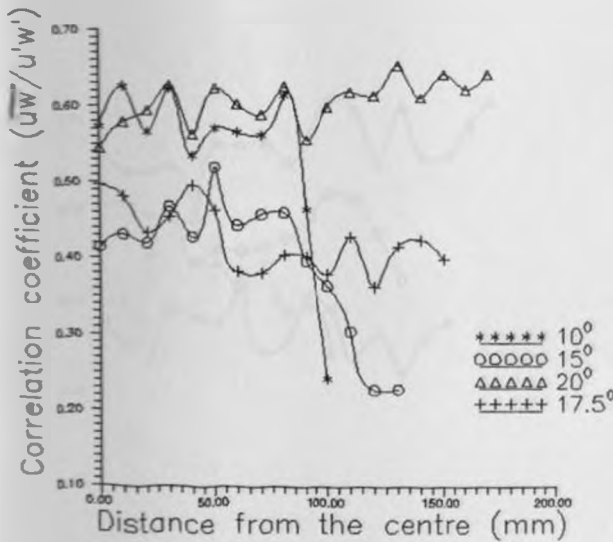
Figure 44 CORRELATION COEFFICIENT ( $\overline{uw}/u'w'$ ) MEASURED ALONG A DISTANCE 60MM FROM THE WALL



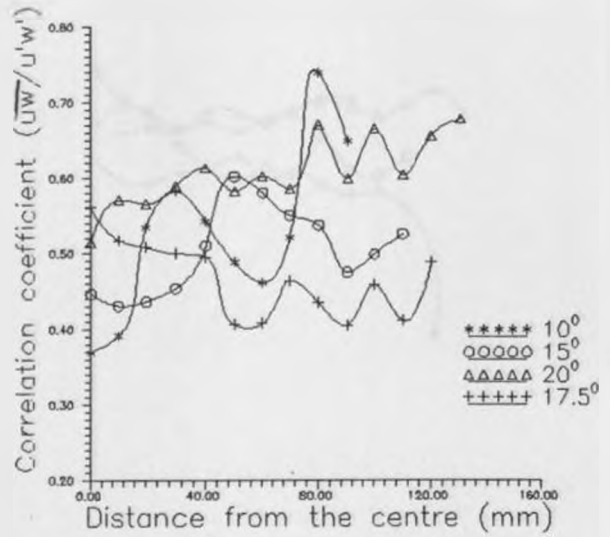
(a) At the exit plane



(b) At 100mm from the exit



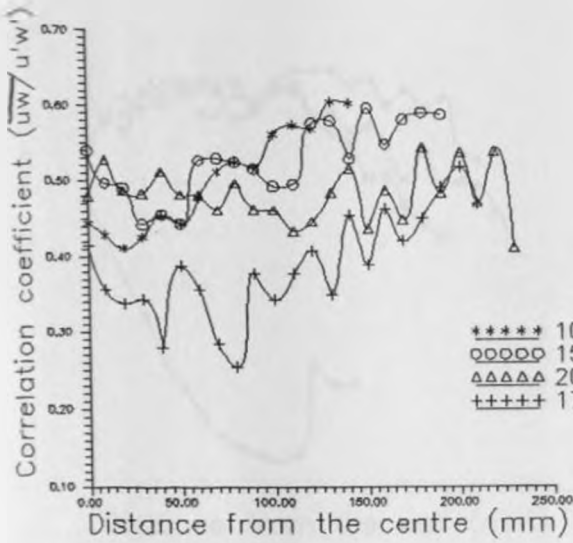
(c) At 200mm from exit



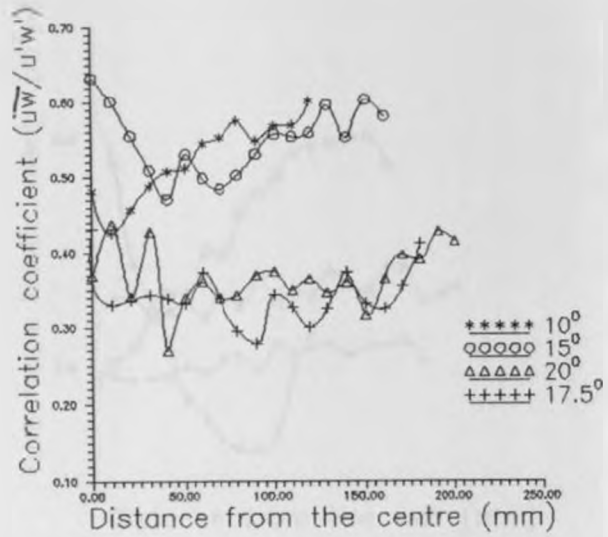
(d) At 300mm from exit

Figure 45

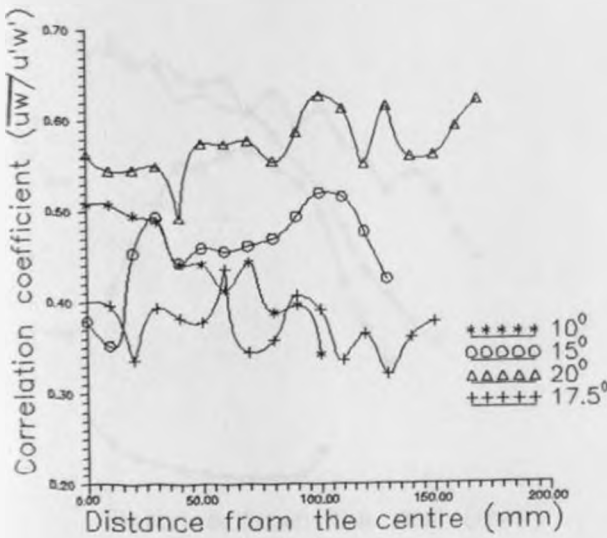
CORRELATION COEFFICIENT ( $\overline{uw}/u'w'$ )  
 MEASURED ALONG A DISTANCE 20MM FROM  
 FROM THE WALL



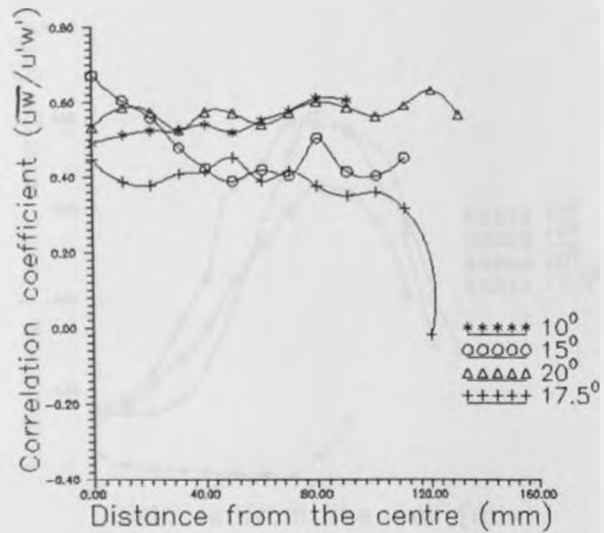
(a) At the exit plane



(b) At 100mm from the exit



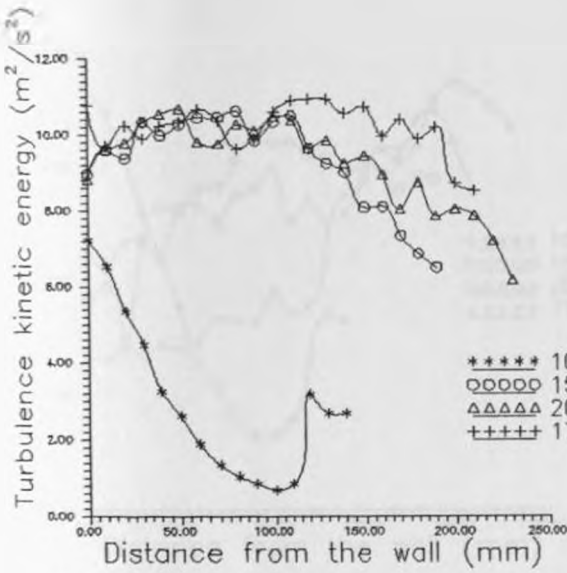
(c) At 200mm from exit



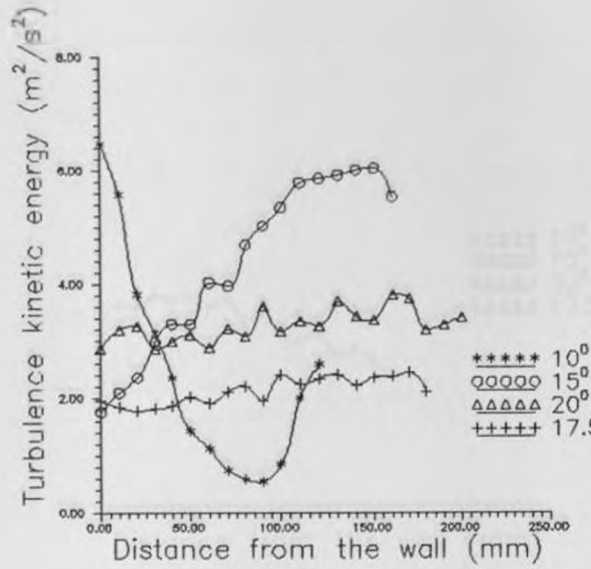
(d) At 300mm from exit



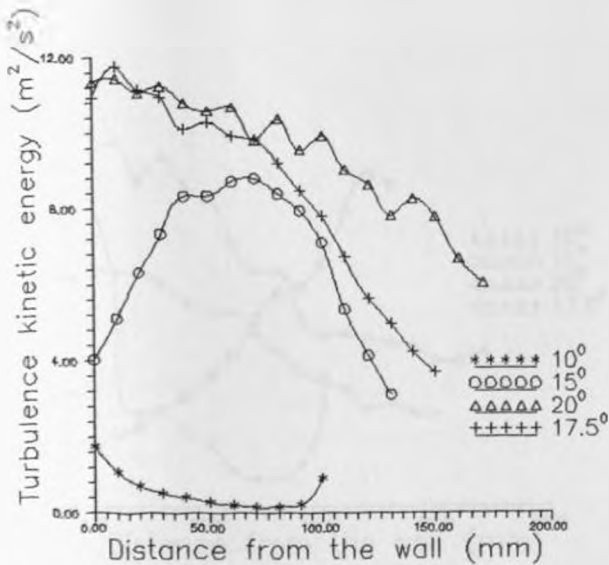
Figure 46 TURBULENCE KINETIC ENERGY MEASURED ALONG THE CENTRELINE



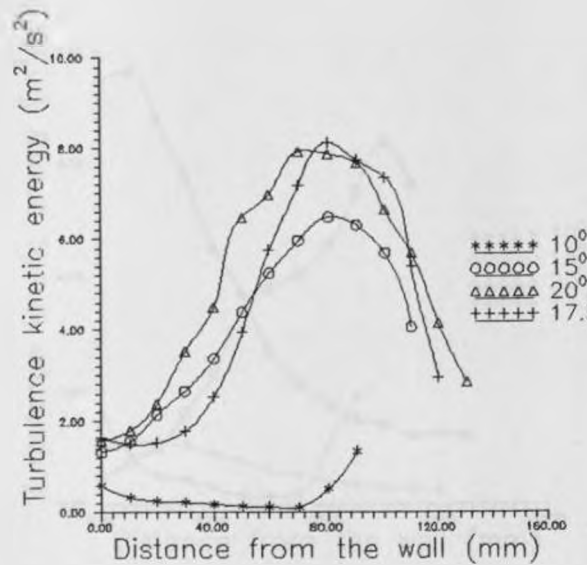
(a) At the exit plane



(b) At 100mm from the exit

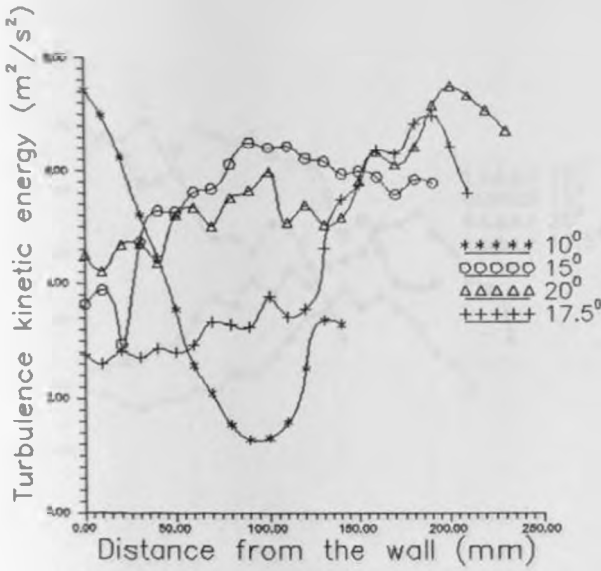


(c) At 200mm from exit

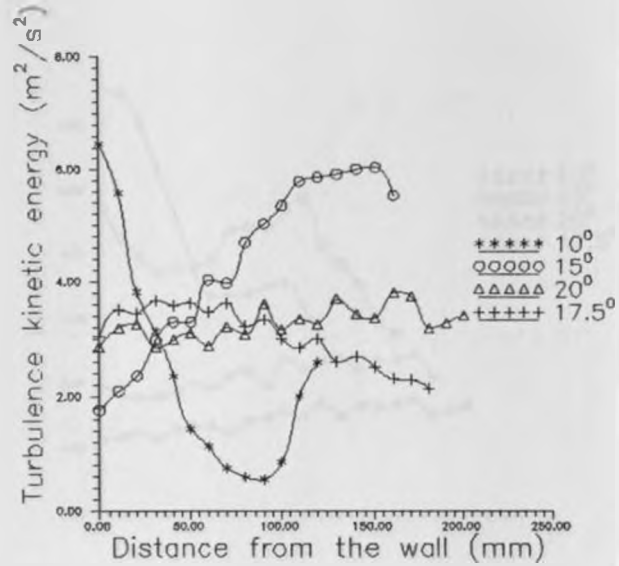


(d) At 300mm from exit

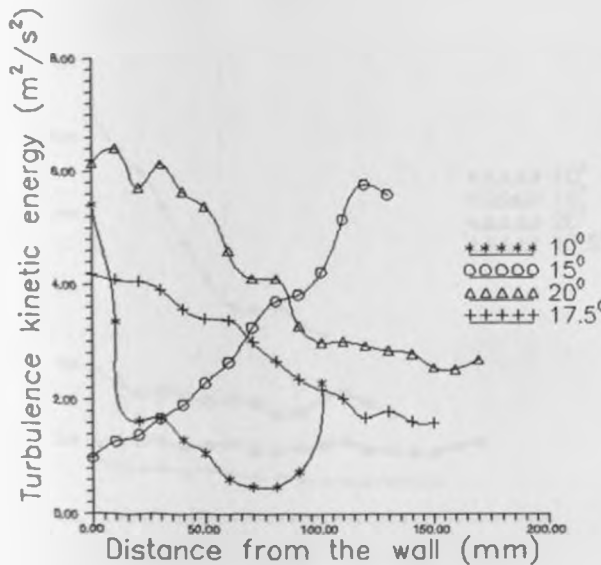
Figure 47 TURBULENCE KINETIC ENERGY MEASURED ALONG A DISTANCE 60MM FROM THE WALL



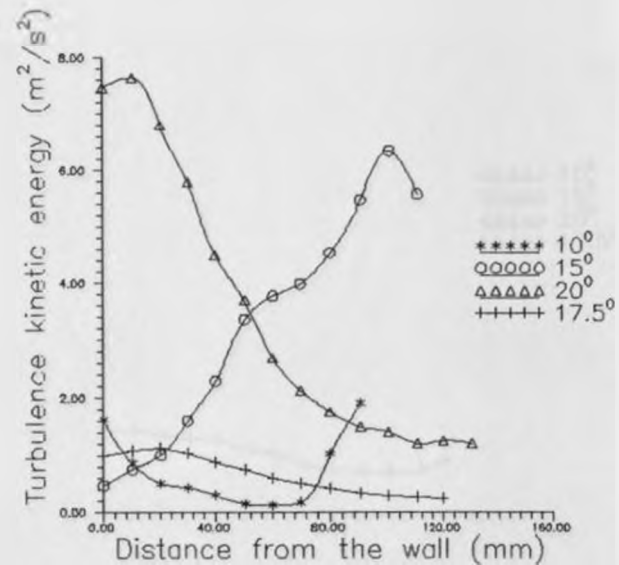
(a) At the exit plane



(b) At 100mm from the exit

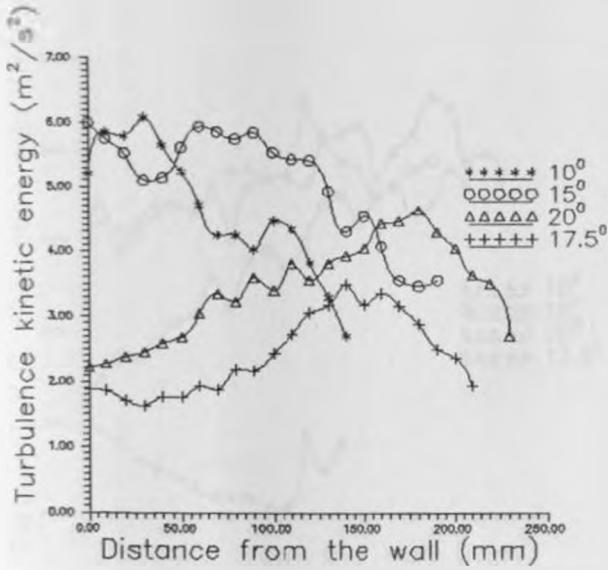


(c) At 200mm from exit

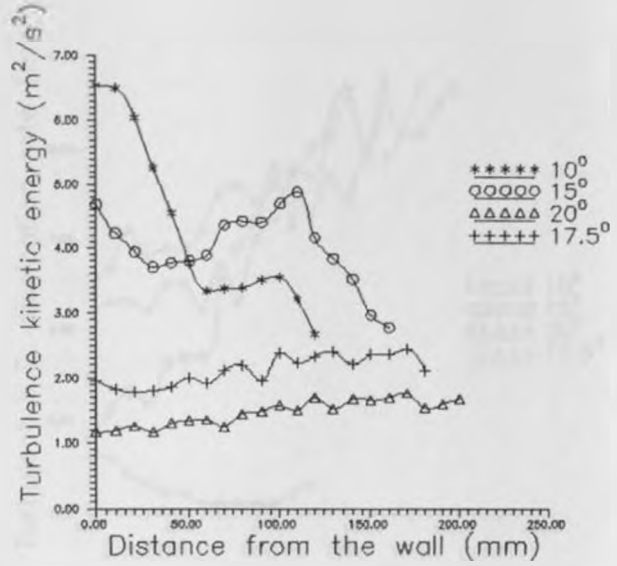


(d) At 300mm from exit

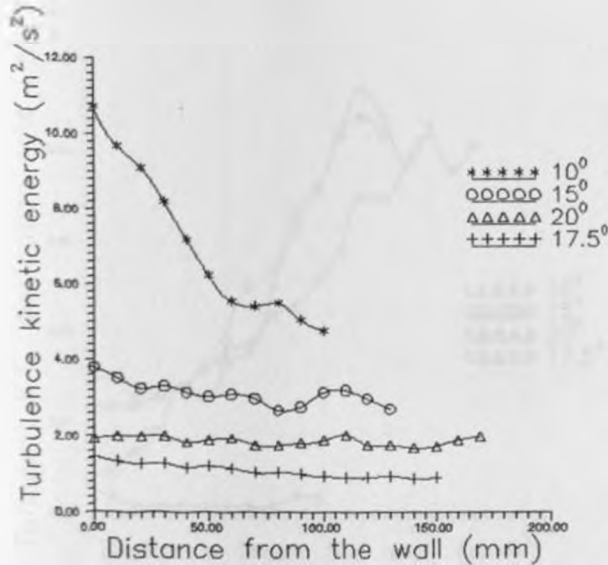
Figure 48 TURBULENCE KINETIC ENERGY MEASURED ALONG A DISTANCE 20MM FROM THE WALL



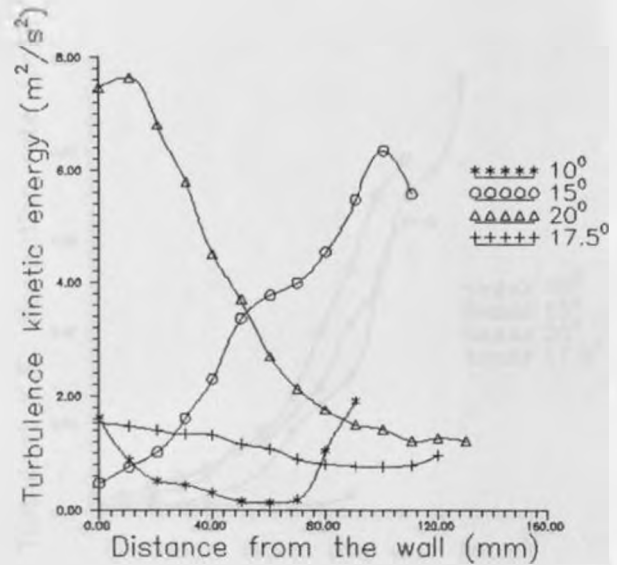
(a) At the exit plane



(b) At 100mm from the exit

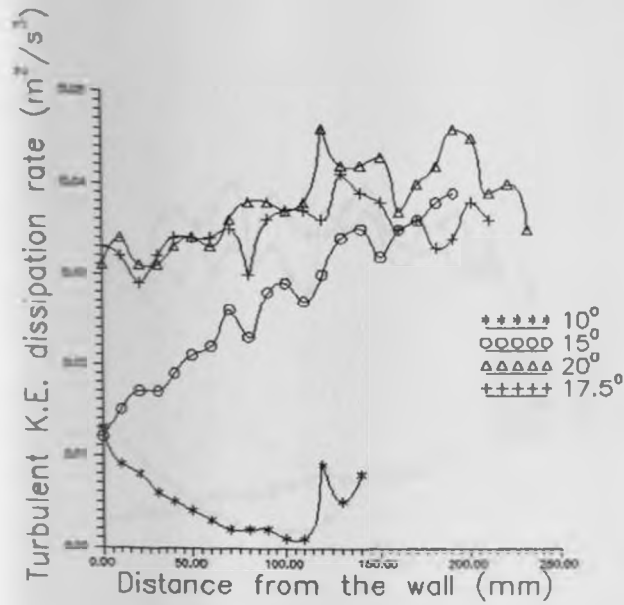


(c) At 200mm from exit

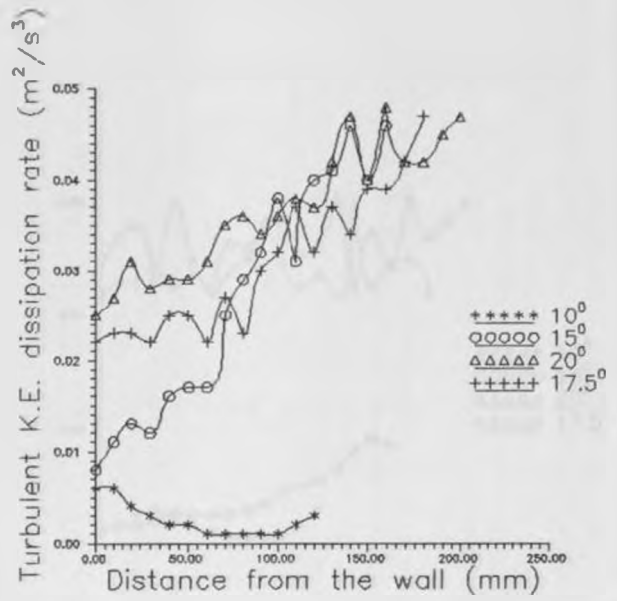


(d) At 300mm from exit

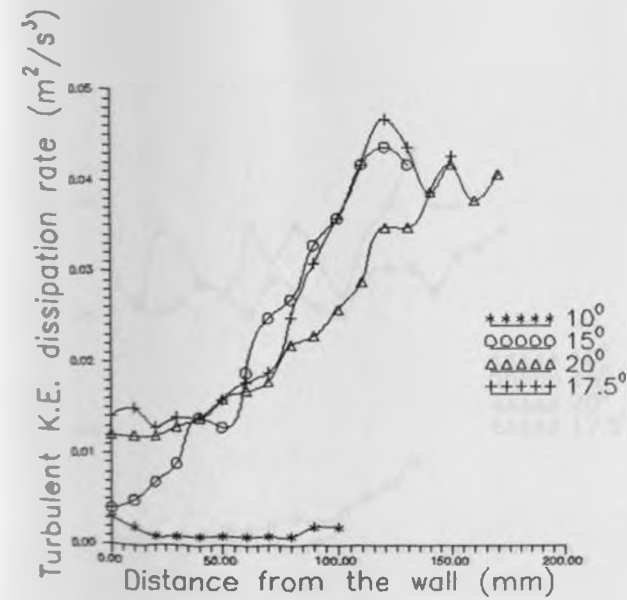
Figure 49 TURBULENT KINETIC ENERGY DISSIPATION RATE MEASURED ALONG THE CENTRELINE



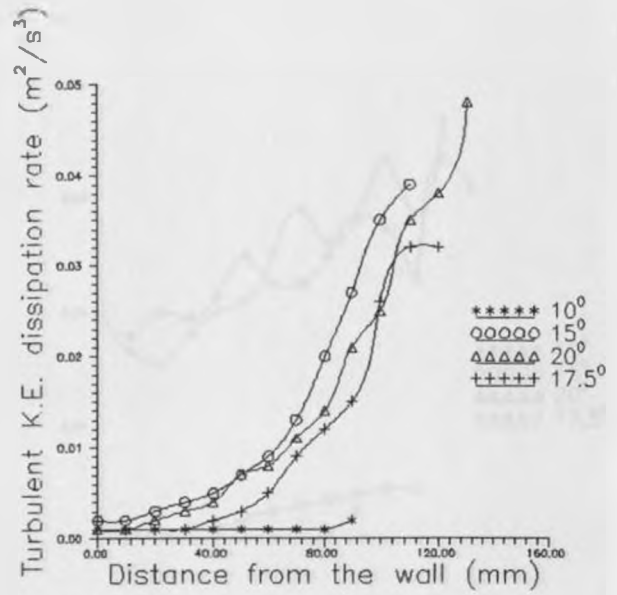
(a) At the exit plane



(b) At 100mm from the exit

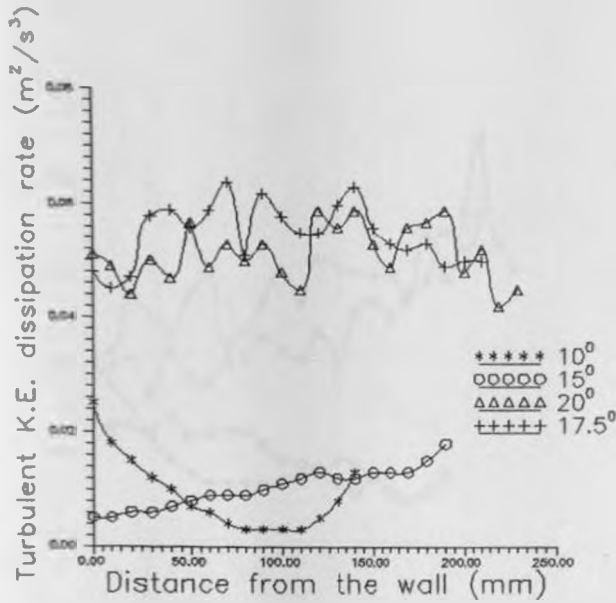


(c) At 200mm from exit

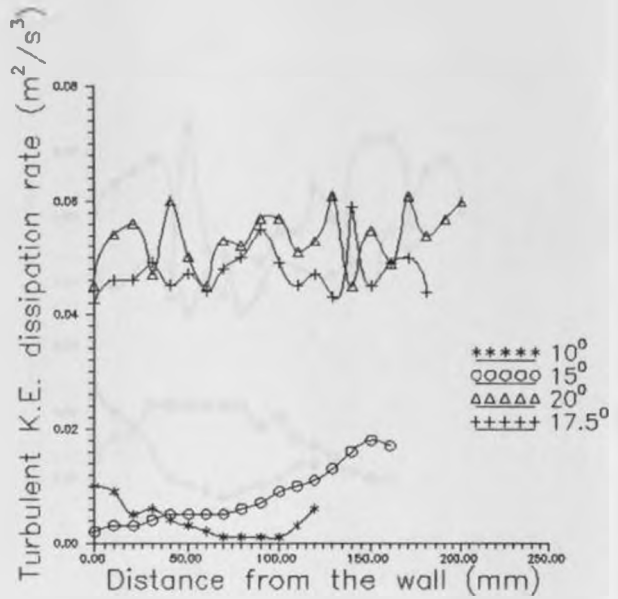


(d) At 300mm from exit

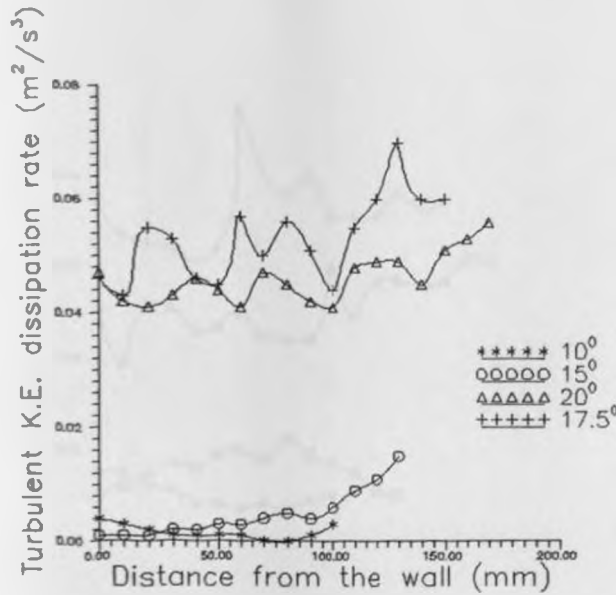
Figure 50 TURBULENT KINETIC ENERGY DISSIPATION RATE MEASURED ALONG A DISTANCE 60MM FROM THE WALL



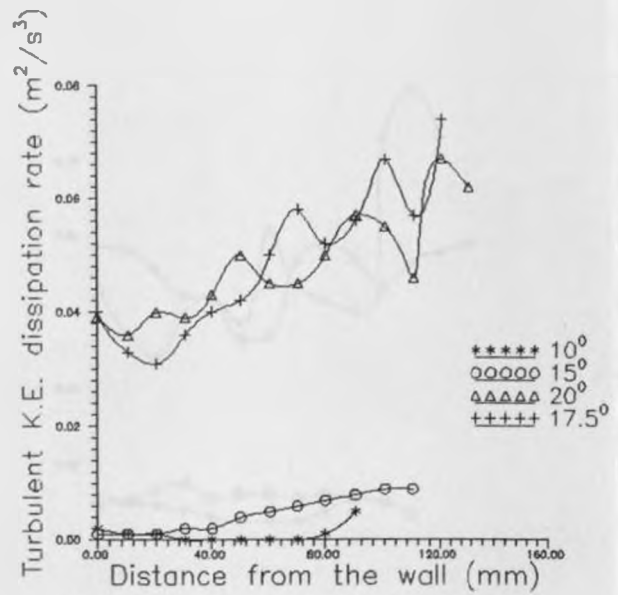
(a) At the exit plane



(b) At 100mm from the exit

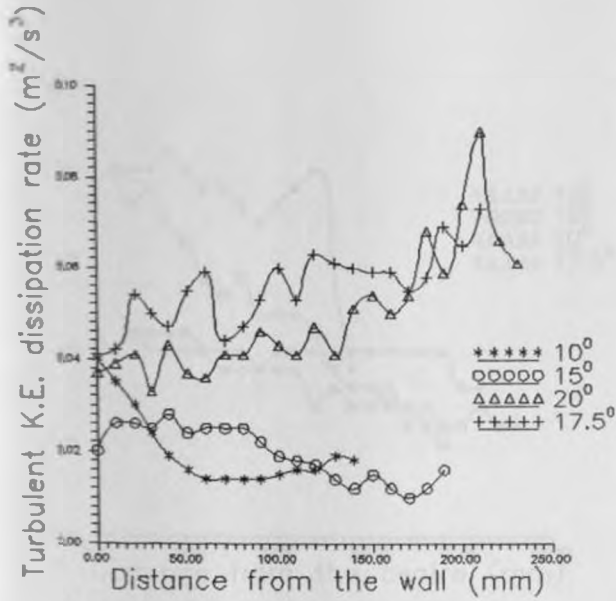


(c) At 200mm from exit

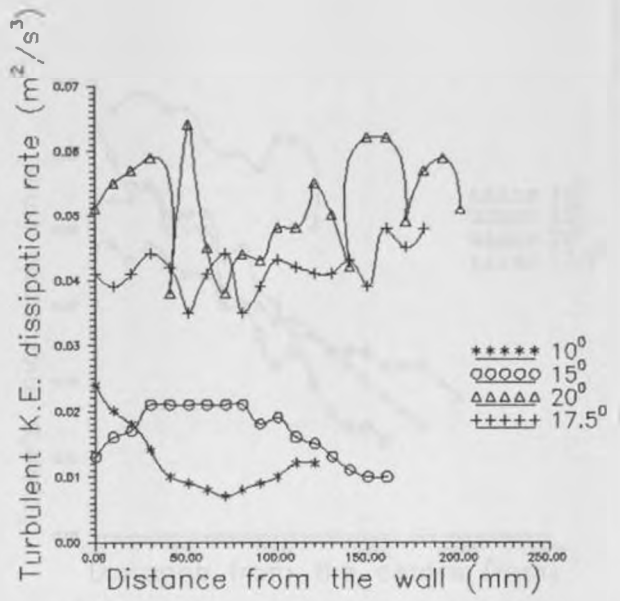


(d) At 300mm from exit

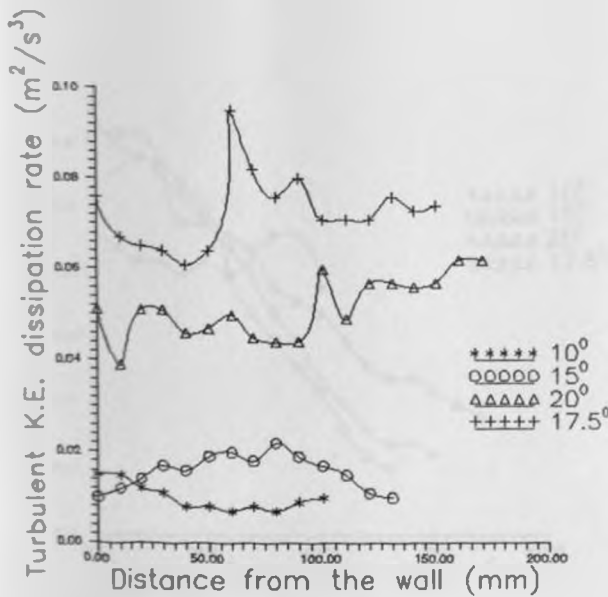
Figure 51 TURBULENT KINETIC ENERGY DISSIPATION RATE MEASURED ALONG A DISTANCE 20MM FROM THE WALL



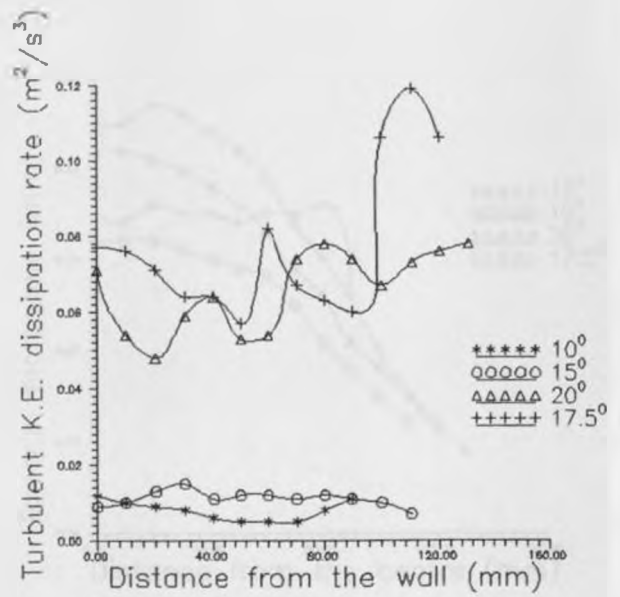
(a) At the exit plane



(b) At 100mm from the exit

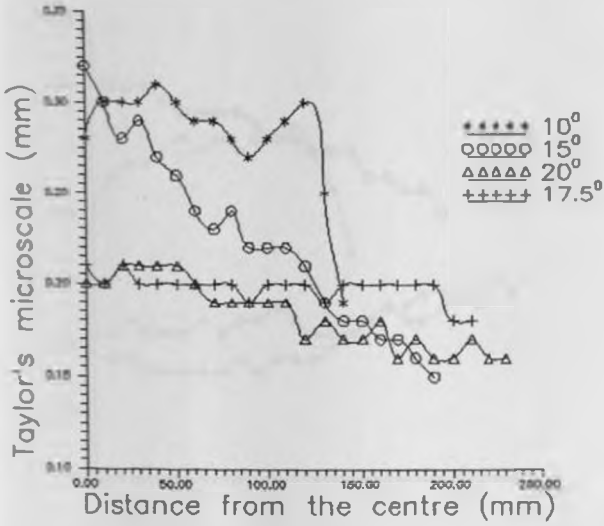


(c) At 200mm from exit

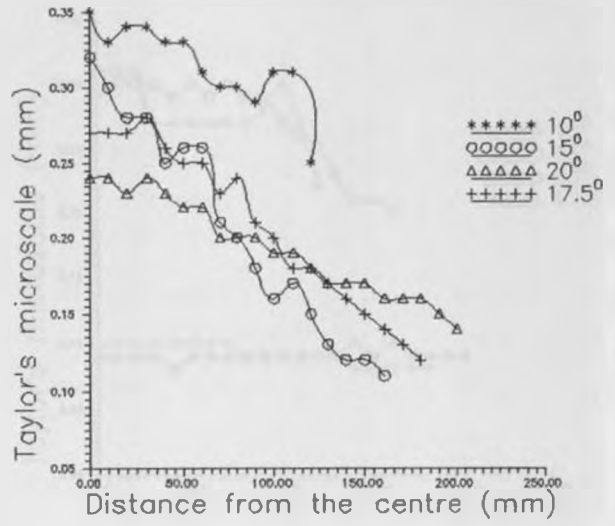


(d) At 300mm from exit

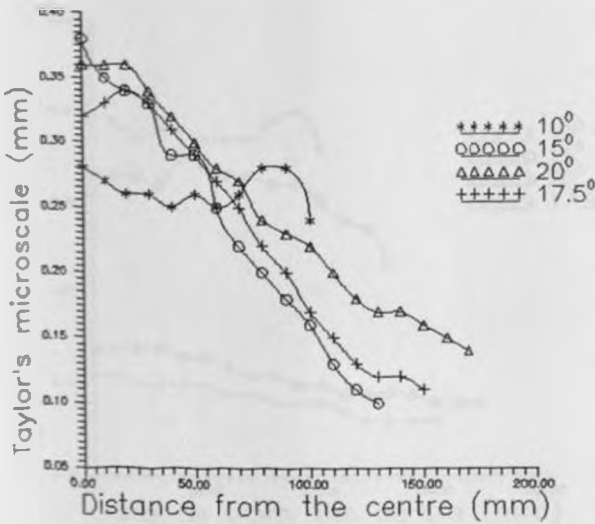
Figure 52 TAYLOR'S MICROSCALE EVALUATED ALONG THE CENTRELINE



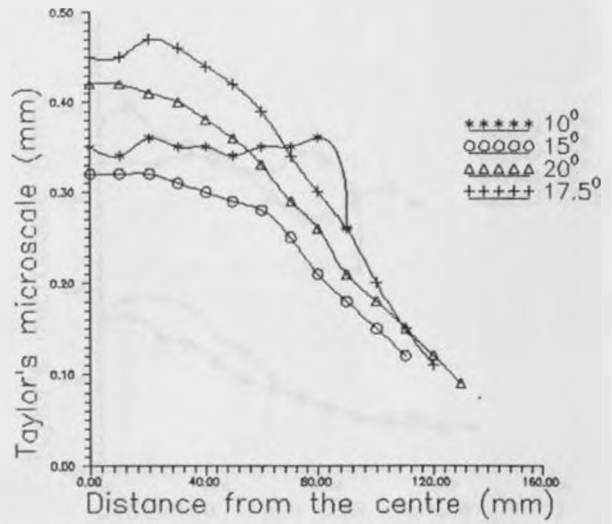
(a) At the exit plane



(b) At 100mm from the exit

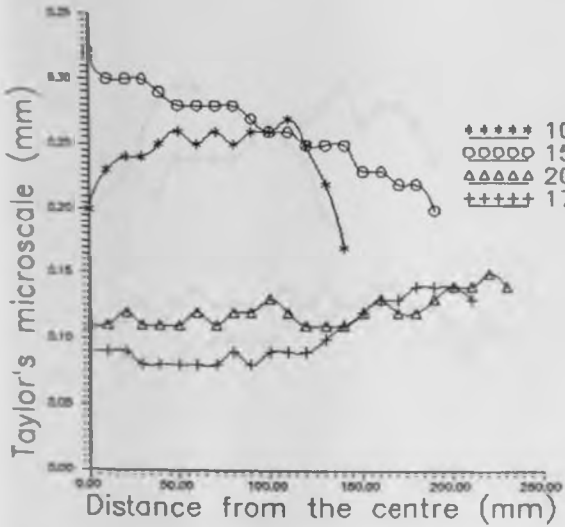


(c) At 200mm from exit

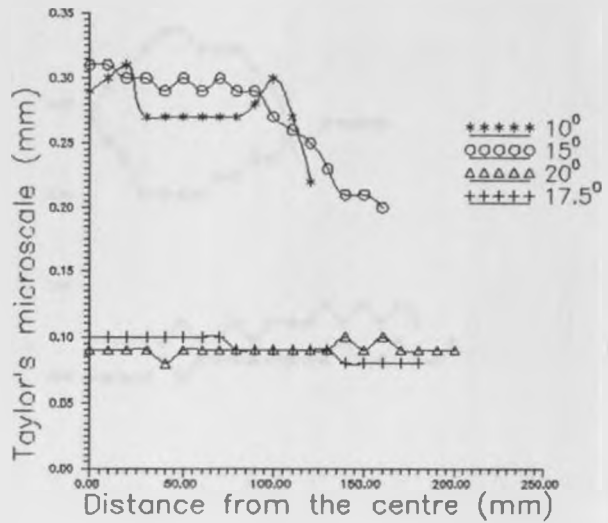


(d) At 300mm from exit

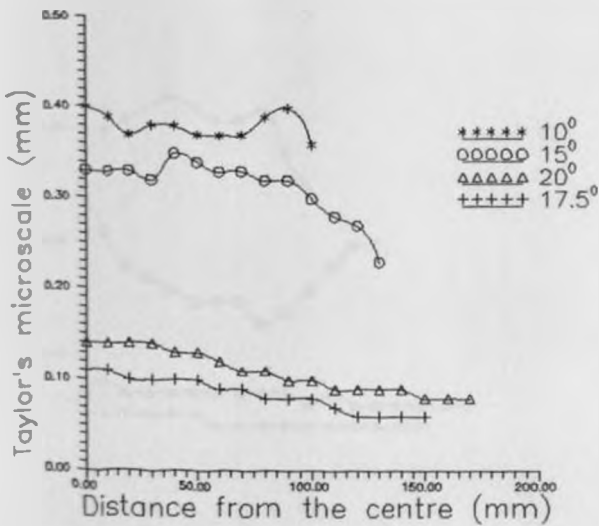
Figure 53 TAYLOR'S MICROSCALE EVALUATED ALONG A DISTANCE 60MM FROM THE WALL



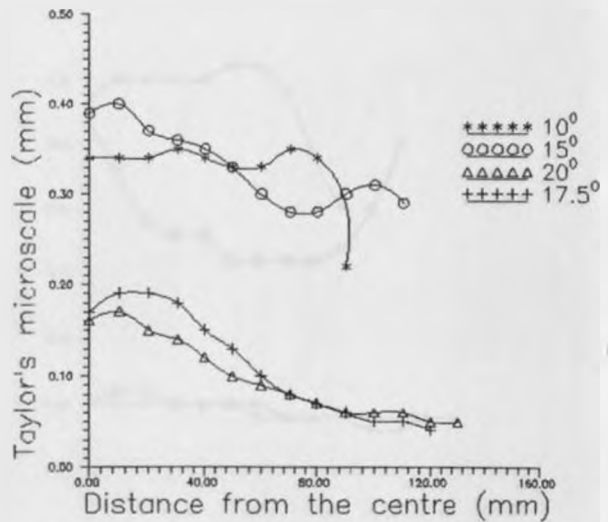
(a) At the exit plane



(b) At 100mm from the exit



(c) At 200mm from exit

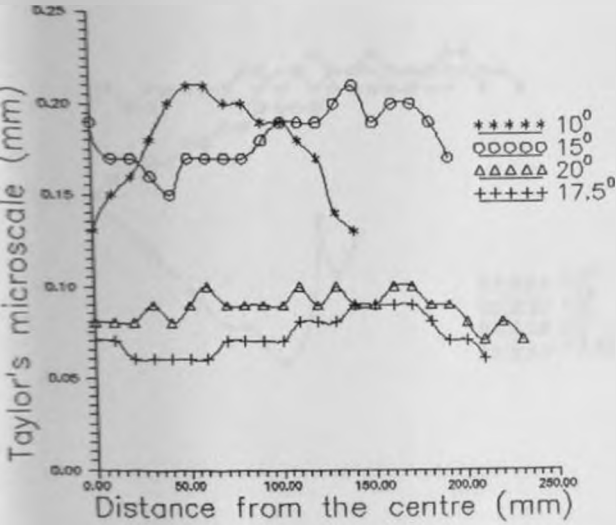


(d) At 300mm from exit

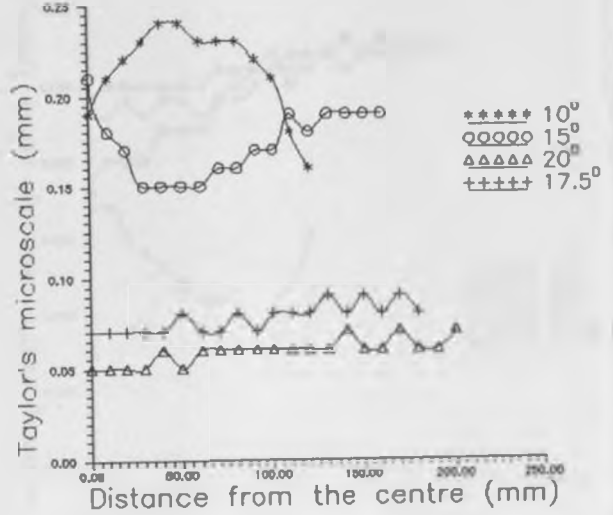


Figure 54

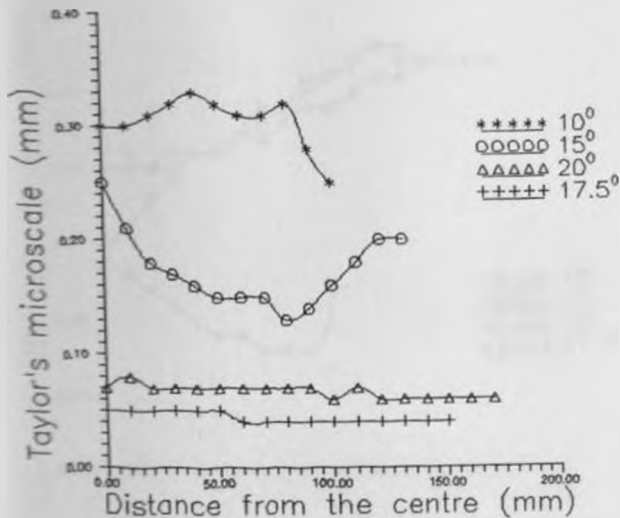
TAYLOR'S MICROSACLE EVALUATED ALONG A DISTANCE 20MM FROM THE WALL



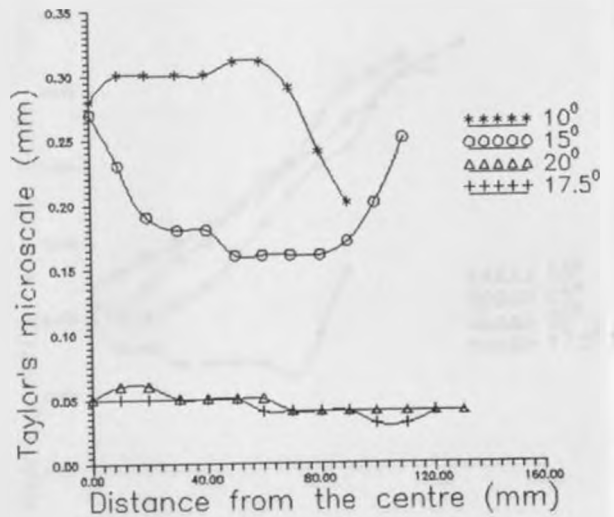
(a) At the exit plane



(b) At 100mm from the exit

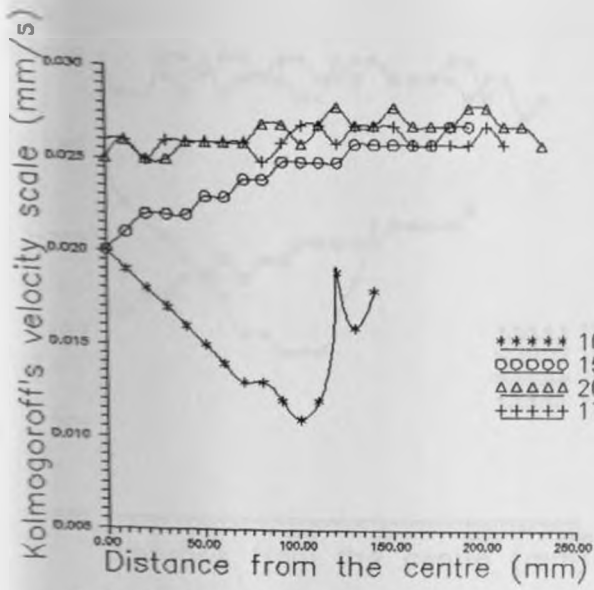


(c) At 200mm from exit

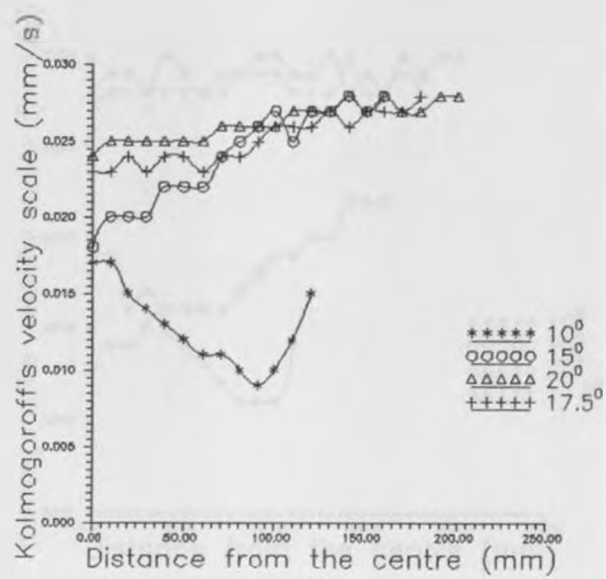


(d) At 300mm from exit

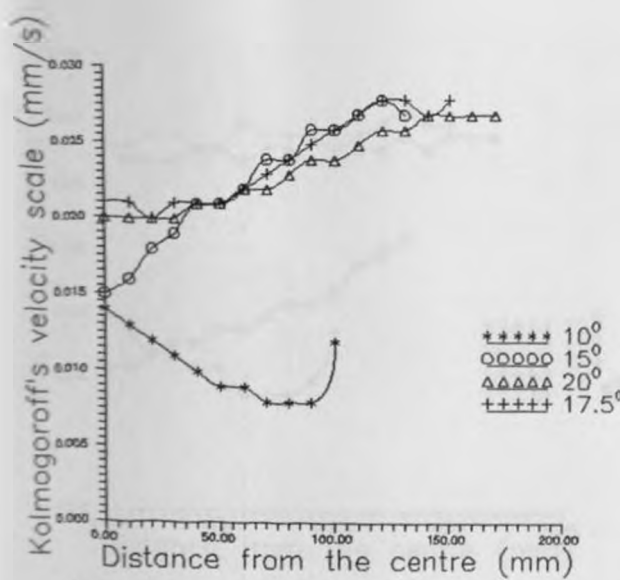
Figure 55 KOLMOGOROFF'S VELOCITY SCALE EVALUATED ALONG THE CENTRELINE



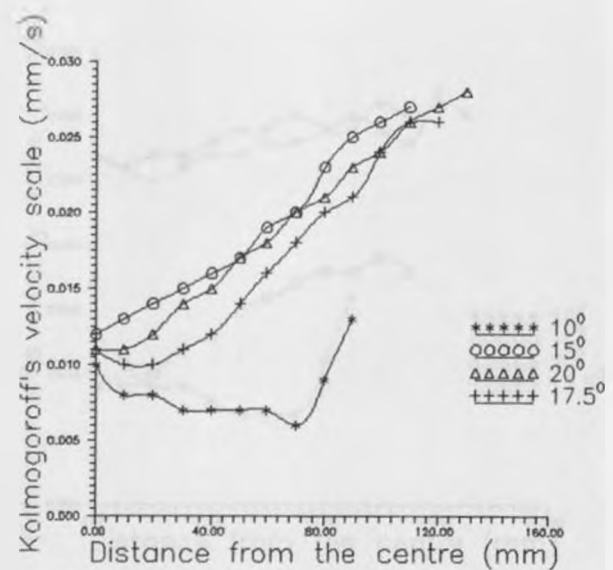
(a) At the exit plane



(b) At 100mm from the exit

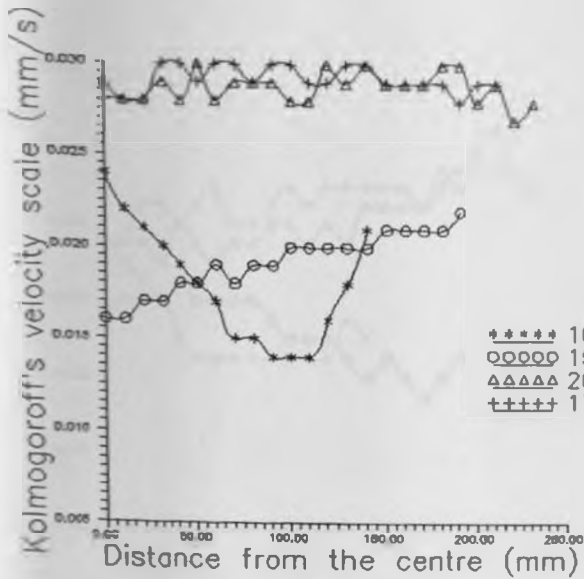


(c) At 200mm from exit

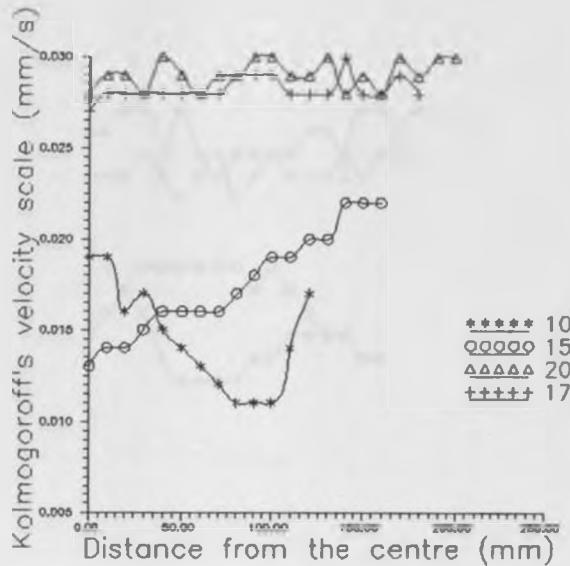


(d) At 300mm from exit

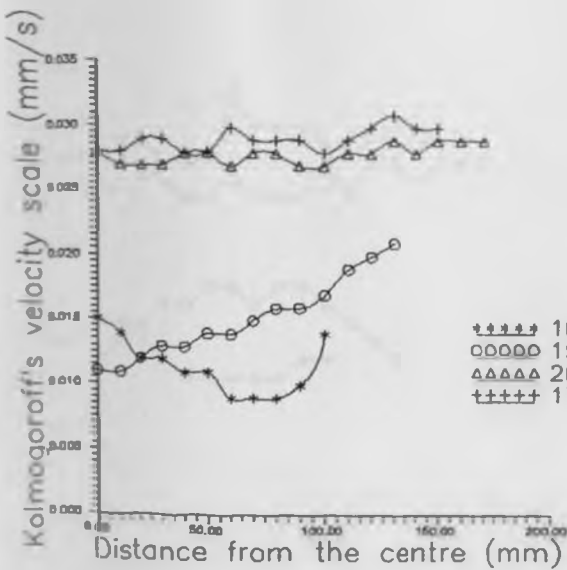
Figure 56 KOLMOGOROFF'S VELOCITY SCALE EVALUATED ALONG A DISTANCE 60MM FROM THE WALL



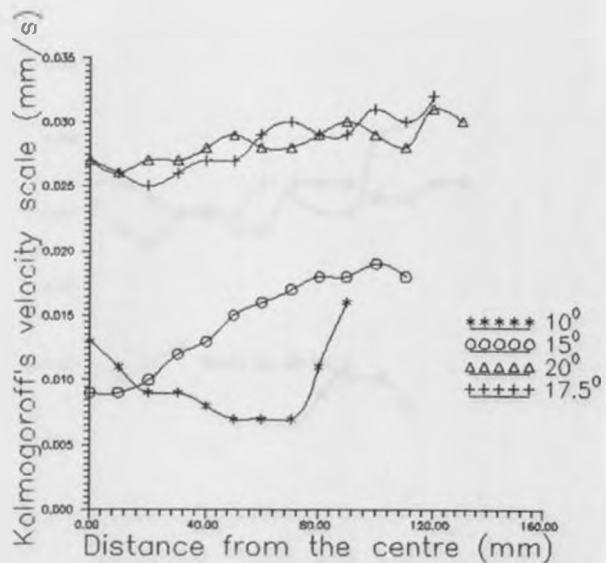
(a) At the exit plane



(b) At 100mm from the exit



(c) At 200mm from exit



(d) At 300mm from exit

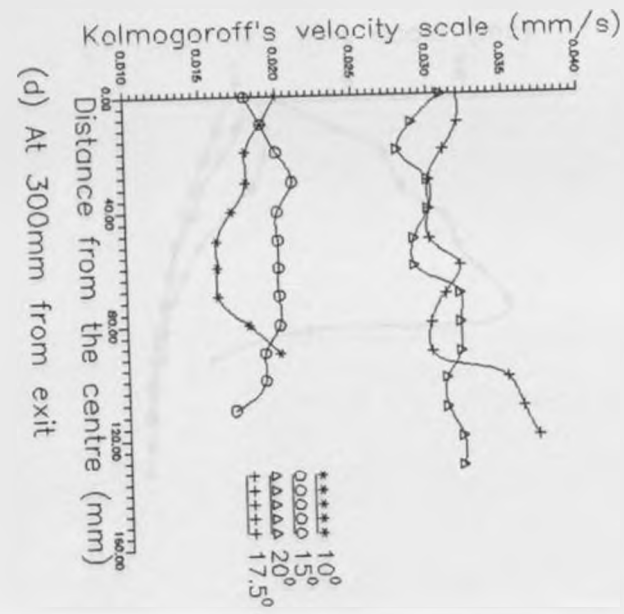
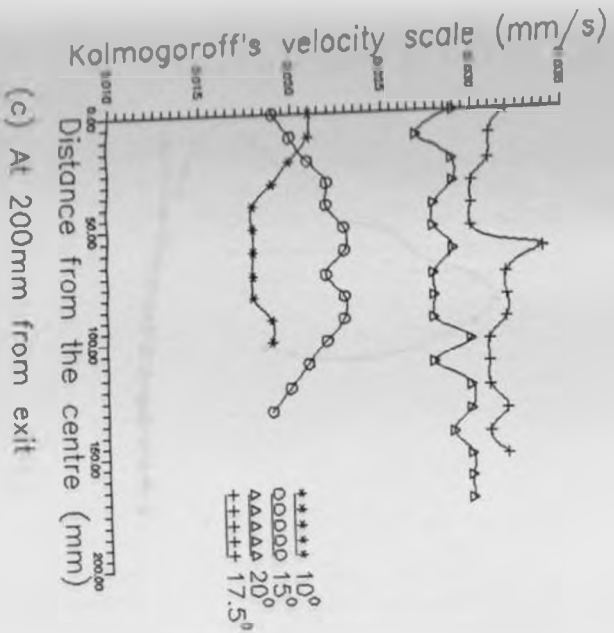


Figure 57 KOLMOGOROFF'S VELOCITY SCALE EVALUATED ALONG A DISTANCE 20MM FROM THE WALL

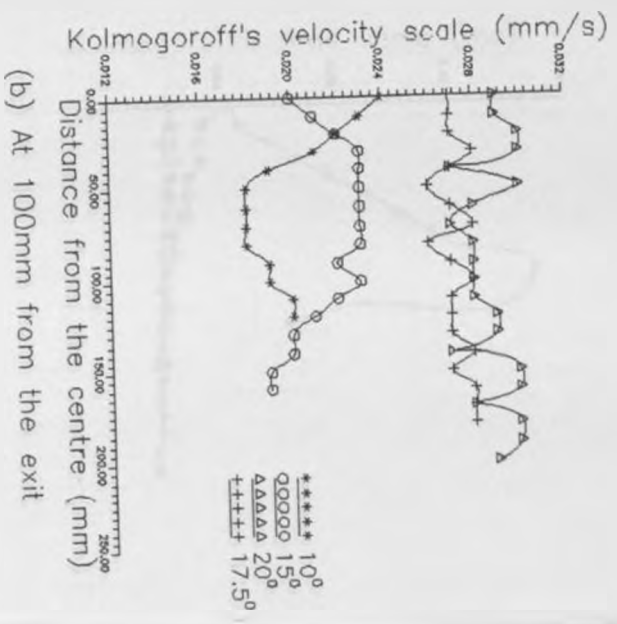
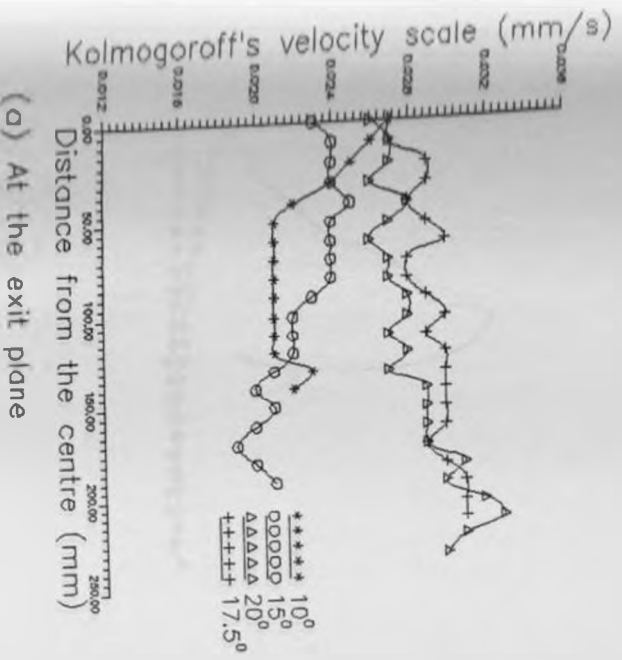
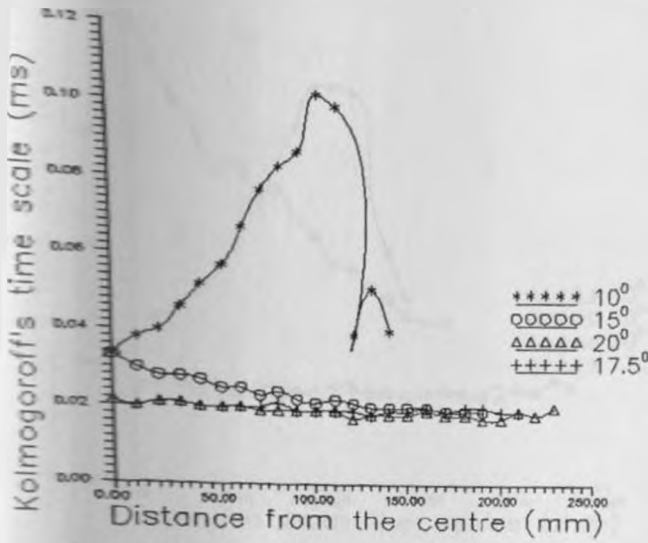
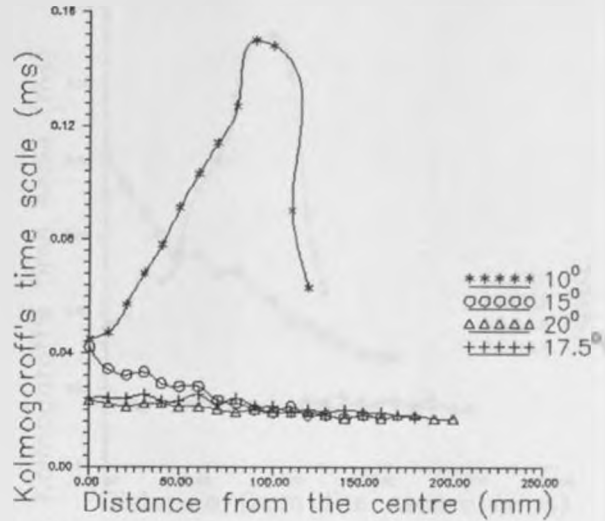


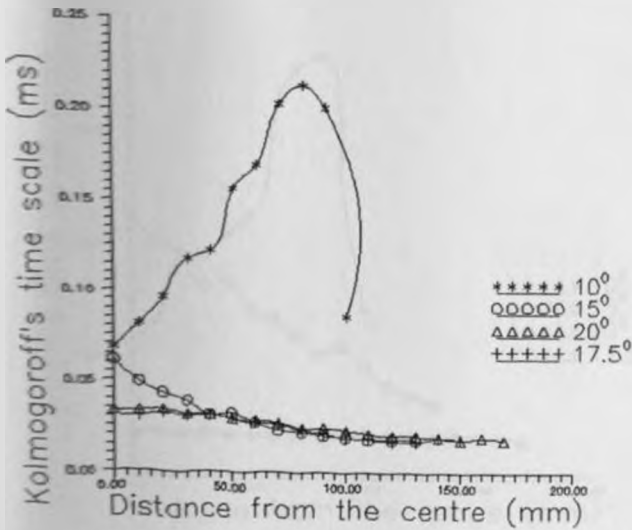
Figure 58 KOLMOGOROFF'S TIME SCALE EVALUATED ALONG THE CENTRELINE



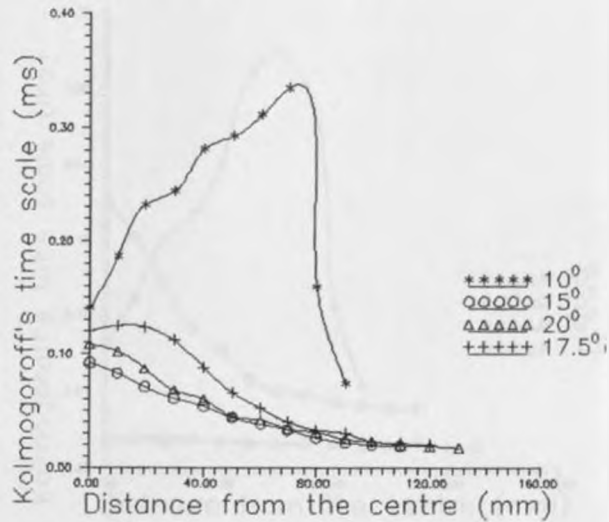
(a) At the exit plane



(b) At 100mm from the exit



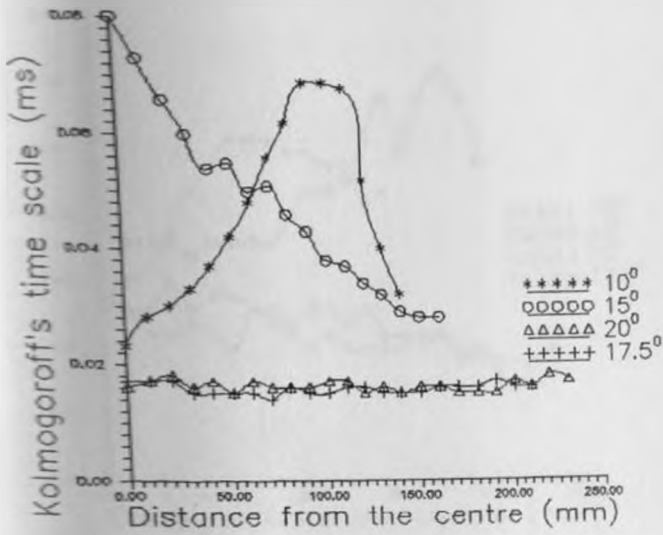
(c) At 200mm from exit



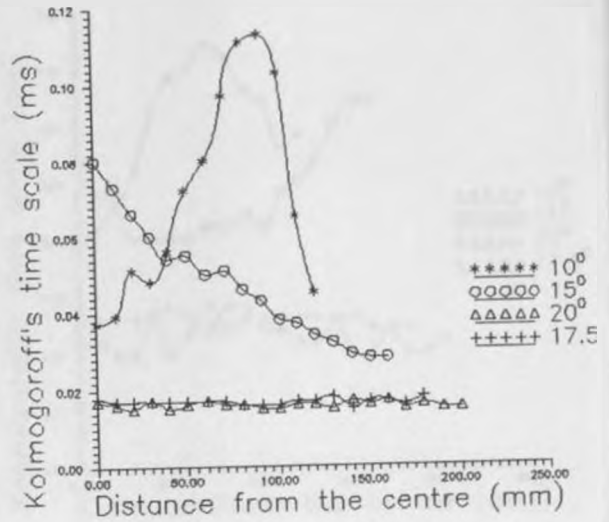
(d) At 300mm from exit

Figure 59

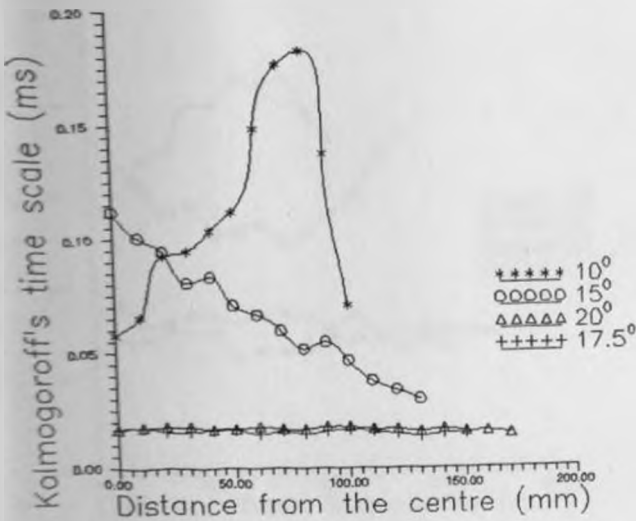
KOLMOGOROFF'S TIME SCALE EVALUATED ALONG A DISTANCE 60MM FROM THE WALL



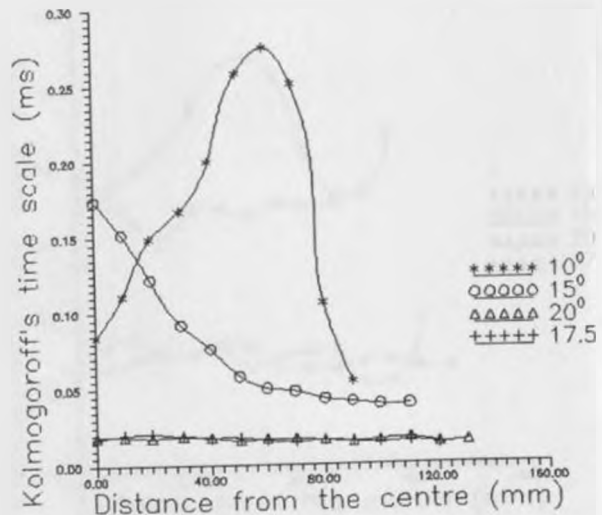
(a) At the exit plane



(b) At 100mm from the exit



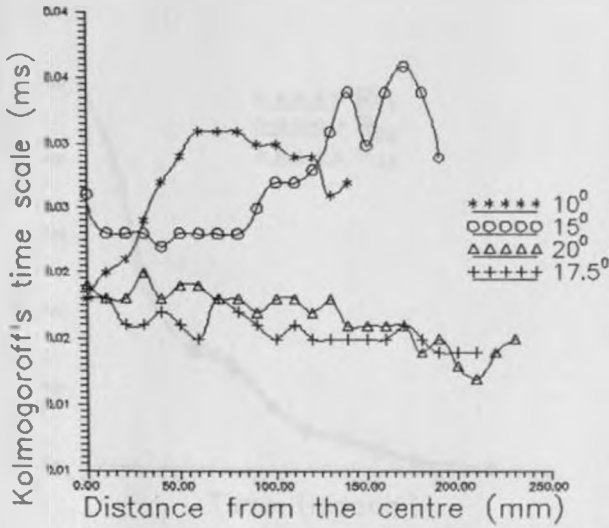
(c) At 200mm from exit



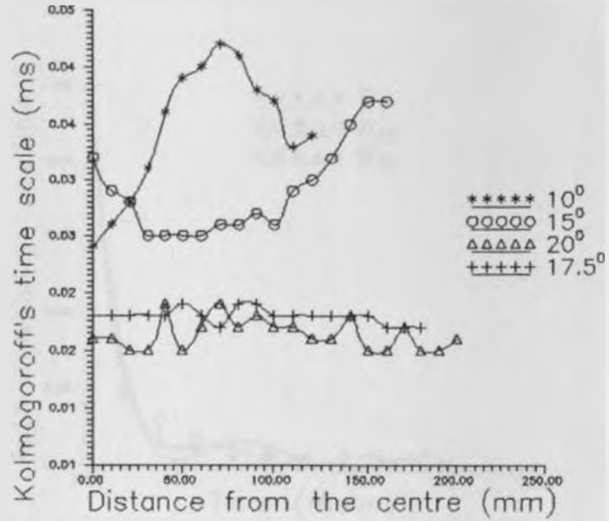
(d) At 300mm from exit

Figure 60

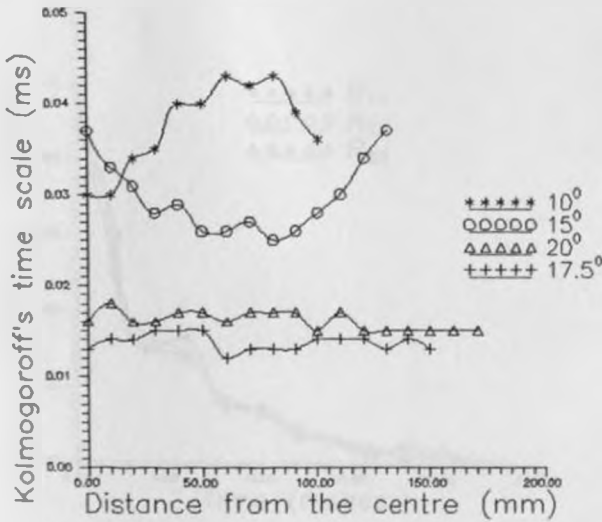
KOLMOGOROFF'S TIME SCALE EVALUATED ALONG A DISTANCE 20MM FROM THE WALL



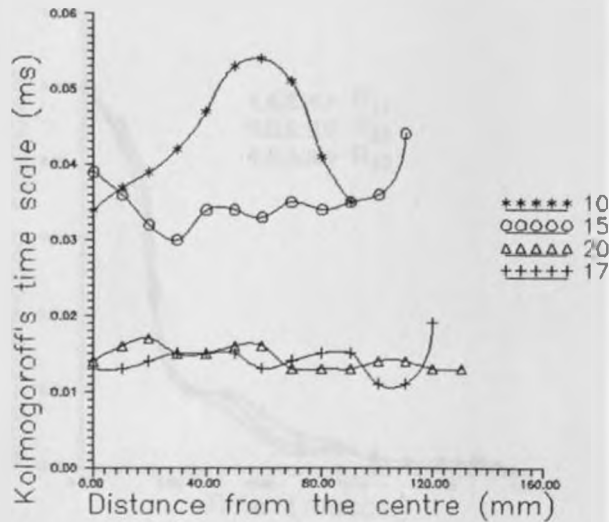
(a) At the exit plane



(b) At 100mm from the exit



(c) At 200mm from exit



(d) At 300mm from exit



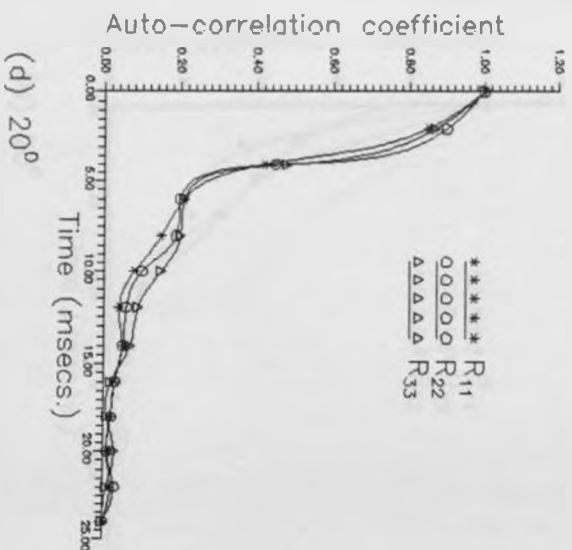
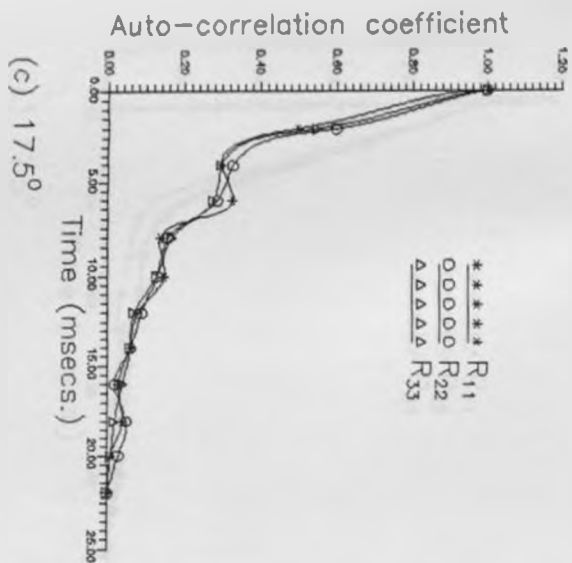


Figure 61 AUTO-CORRELATION COEFFICIENTS MEASURED ON THE EXIT PLANE AT THE CENTRE POSITION

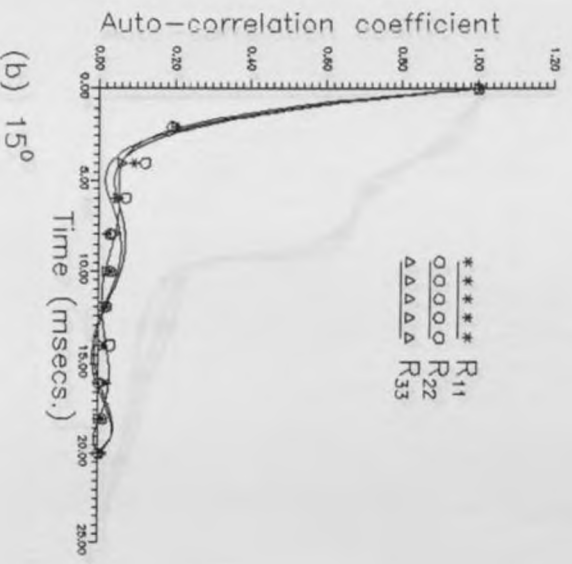
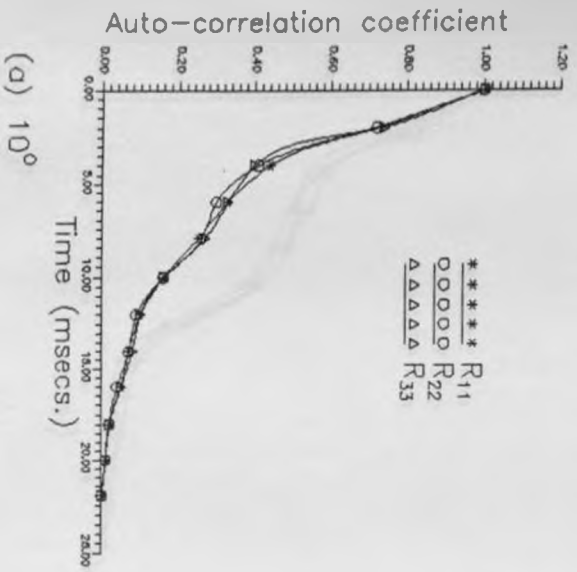


Figure 62 AUTO-CORRELATION COEFFICIENTS MEASURED ON THE EXIT PLANE AT THE CENTRE POSITION 60MM FROM THE WALL

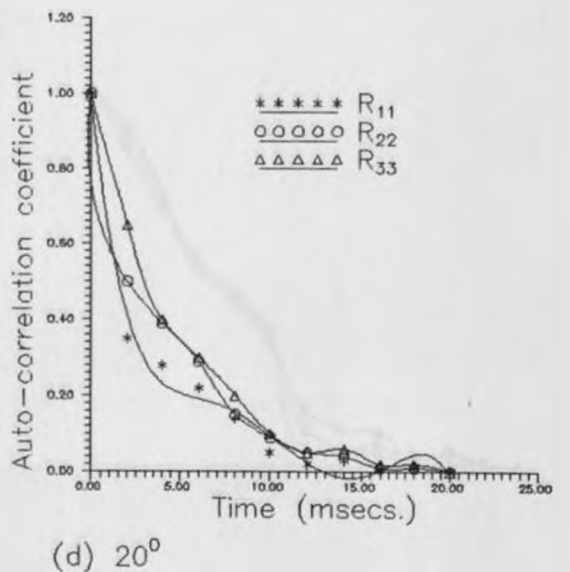
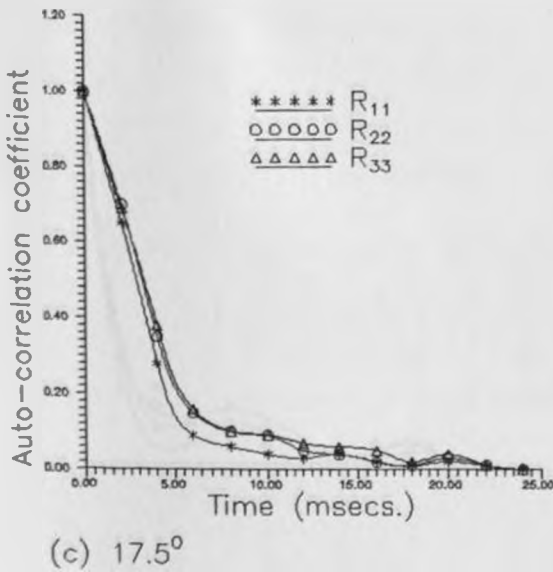
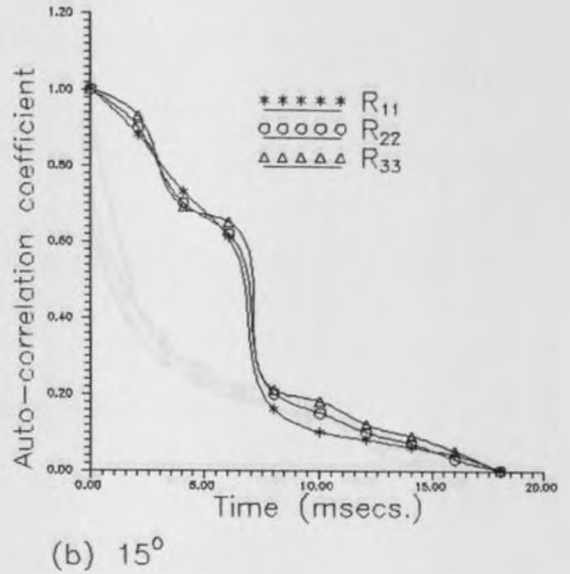
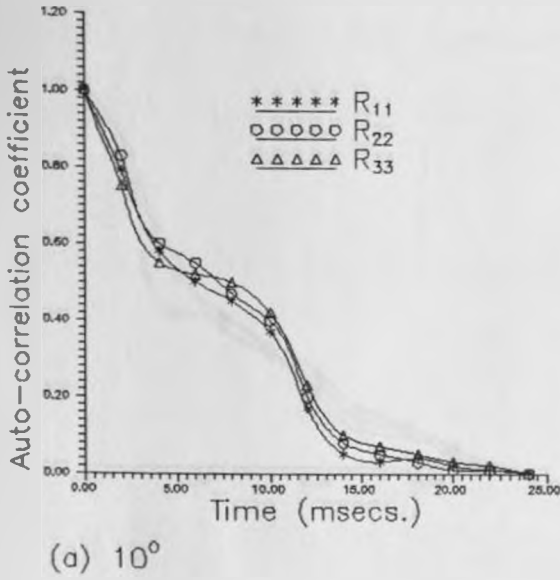
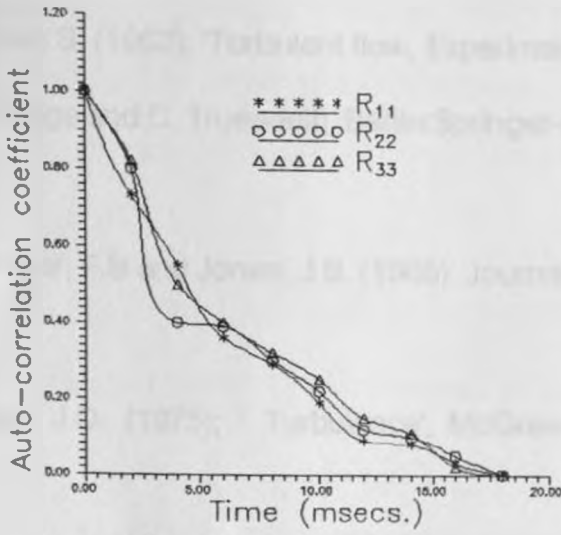
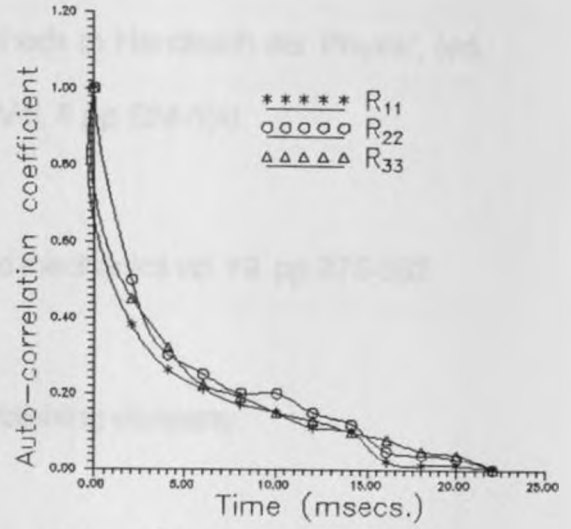


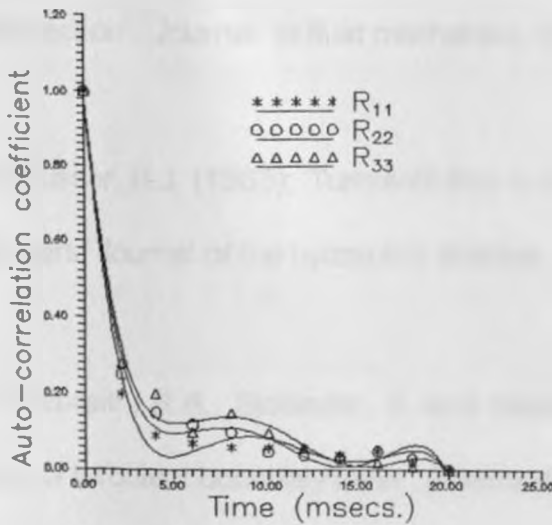
Figure 63 AUTO-CORRELATION COEFFICIENTS MEASURED ON THE EXIT PLANE AT THE CENTRE POSITION 20MM FROM THE WALL



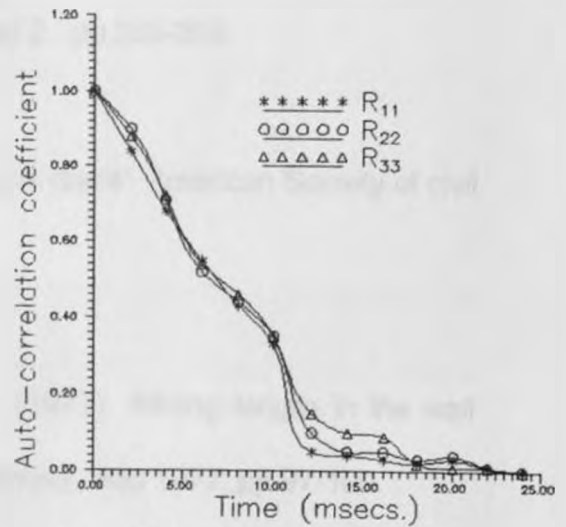
(a)  $10^\circ$



(b)  $15^\circ$



(c)  $17.5^\circ$



(d)  $20^\circ$

## REFERENCES

- Brundrett, E. and Baines, W.D. (1964); 'The production and diffusion of vorticity in duct flow', *Journal of fluid mechanics* vol. 19. pp 375-394.
- Corrsin S. (1963); 'Turbulent flow, Experimental methods in Handbuch der Physik', (ed. S. Flugge and C. Truesdell), Berlin: Springer-verlag, Vol. 8 pp 524-590.
- Gessner, F.B and Jones, J.B. (1965); *Journal of Fluid mechanics* vol 19. pp 375-392.
- Hinze, J.O. (1975); 'Turbulence', McGraw-Hill Publishing company.
- Hoagland, L.C. (1960); 'Sc.D thesis', Mech. Eng. Dept., M.I.T. press.
- Launder, B.E. and Ying, W.M., (1972); 'Secondary flows in ducts of square cross-section', *Journal of fluid mechanics*, vol.54 part 2. pp 289-295.
- Leutheusser, H.J. (1963); 'Turbulent flow in rectangular ducts', American Society of civil engineers, *Journal of the hydraulics division*. pp 89.
- McDGalbraith, R.A., Sjolander, S. and Head, M.R., (1977); 'Mixing length in the wall region of turbulent boundary layer', *Aeronautical Quarterly*, May 1977, pp 97-100.

Nikuradse, J. (1926); 'Untersuchungen über die geschwindigkeitsverteilung in turbulenten strömungen. thesis gottingen V.D.I. forsch.

Nitsche, W Nasser, M. and Bartsch, P. (1993); 'Investigation on turbulent transport processes in relaxing diffuser flows', Proceedings of the second international symposium on engineering turbulence modelling and measurements, Florence, Italy. pp 479-488.

Patel, V.C. (1965); 'Calibration of the preston tube and limitation in its use in pressure gradients', Journal of Fluid Mechanics, vol. 23 pp 185-208

Prandtl, L. (1925); 'Über den Reibungswiderstand strömender luft', Ergeb Aerodyn. Versuch., Gottingen III series.

Prinos, P., Tavoularis, S, and Townsend, R. (1988); 'Turbulence measurements in smooth and rough-walled trapezoidal ducts', Research report, University of Ottawa, Canada.

Rodet, E (1960); 'Etude de l'écoulement d'un fluide dans un tunnel prismatique de section trapézoïdale', Publications scientifiques et Techniques du ministère de L'Air no. 369.

Speziale, C.G., So, R.M.C. and Younis, B.A. (1993); 'On the prediction of turbulent secondary flows', Elsevier Science Publishers B.V.. pp 105-121.

Tennekes H. and Lumley J.L. , (1972); 'A first course in turbulence', MIT press.

Weiser, N., Bartsch, P. and Nitsche, W. (1990); 'on turbulent flow separation in axisymmetric diffusers', Engineering turbulence modelling and Experiments, Institut für Luft-und Raumfahrt, Technische, Universität Berlin, FRG. pp 227-236

## APPENDIX

```
1  REM PROGRAM *****KIBICHO.BAS*****
5  SAVE "B:KIBICHO.BAS"
10 REM ** ENTER THE GRADIENT OF THE VOLTAGE VERSUS VELOCITY
11 'CURVE OBTAINED FROM CALIBRATION CURVES FOR EACH WIRE
15 INPUT "K1"; K1
20 INPUT "K2"; K2
25 DIM S1(5000), U1(5000), V(5000)
30 DIM W(5000), UF(5000), VF(5000)
35 DIM WF(5000), UFS(5000), VFS(5000)
40 DIM WFS(5000), UV(5000), UW(5000)
45 DIM UF1(5000), UF2(5000), U2(5000)
47 DIM S2(5000), S3(5000), S4(5000)
48 REM ** INITIALIZE THE A/D CONVERTERS THROUGH THE IEEE-488 (GPIB)
49 'INTERFACE BUS
50 ISET IFC
55 ISET REN
56 REM **GIVE THE ADDRESSES OF THE TWO A/D CONVERTERS AS SET IN
57 'THE TALK ONLY MODE OF THE MULTIMETERS
58 CMDELIM = 10 : T.O = 20
59 CMDELIM = 10 : T.O = 30
60 INPUT "ENTER N"; N
61 REM **FETCH DATA FROM A/D CONVERTERS AND GET THE COMPUTER'S
62 'READING AND CONVERSION TIME AND OBTAIN U & V
63 X$=TIME
64 HR1=VAL(LEFT(X$,2))*3600
65 MIN1=VAL(MID(X$(4,2)))*60
66 SEC1=VAL(RIGHT(X$,2))
67 TIM1=HR1+MIN1+SEC1
```



```

68  FOR I = 1 TO N
70  LINE INPUT @ 20; A$
75  S1(I) = VAL(A$)
80  LINE INPUT @ 30; B$
85  S2(I) = VAL(B$)
90  NEXT I
91  Y$=TIME
92  HR2=VAL(LEFT(Y$,2))*3600
93  MIN2=VAL(MID(Y$(4,2)))*60
94  SEC2=VAL(RIGHT(Y$,2))
95  TIM2=HR2+MIN2+SEC2
96  TIM=TIM2-TIM1
97  DELT=TIM/2N
109 REM ** TO OBTAIN W
110 INPUT "ROTATE"; ROTATE
115 FOR I = 1 TO N
120 LINE INPUT @ 20; A$
125 S3(I) = VAL(A$)
126 LINE INPUT @30; B$
127 S4(I) = VAL(B$)
130 NEXT I
131 REM ** OBTAIN THE COMPUTER TIME
132 'DELT = TIME DIFFERENCE/2*N
135 SUMU1 = 0
136 SUMU2 = 0
140 SUMV = 0
145 SUMW = 0
146 REM ** CALCULATION OF THE INSTANTANEOUS VELOCITIES
150 FOR I = 1 TO N
155 U1(I) = ((S1(I)/K1) + (S2(I)/K2))/2
156 U2(I) = ((S3(I)/K1) + (S4(I)/K2))/2

```

```

160  V(I) = ((S1(I)/K1) - (S2(I)/K2))/2
165  W(I) = ((S3(I)/K1) - (S4(I)/K2))/2
170  SUMU1 = SUMU1 + U1(I)
171  SUMU2 = SUMU2 + U2(I)
175  SUMV = SUMV + V(I)
180  SUMW = SUMW + W(I)
185  NEXT I
186  REM ** CALCULATION OF THE MEAN VELOCITIES
190  UBAR = SUMU1/N
195  VBAR = SUMV/N
200  WBAR = SUMW/N
205  SUMUF = 0
210  SUMVF = 0
215  SUMWF = 0
220  SUMUV = 0
225  SUMUW = 0
226  REM ** CALCULATION OF THE FLUCTUATING VELOCITIES, RMS
227  'FLUCTUATING VELOCITIES AND THE CORRELATION COEFFICIENTS
235  FOR I = 1 TO N
240  UF1(I) = U1(I) - UBAR
241  UF2(I) = U2(I) - UBAR
245  VF(I) = V(I) - VBAR
250  WF(I) = W(I) - WBAR
255  UFS(I) = UF1(I) ^ 2
260  VFS(I) = VF(I) ^ 2
265  WFS(I) = WF(I) ^ 2
270  UV(I) = UF1(I) * VF(I)
280  UW(I) = UF2(I) * WF(I)
285  SUMUF = SUMUF + UFS(I)
290  SUMVF = SUMVF + VFS(I)
295  SUMWF = SUMWF + WFS(I)

```

```

300  SUMUV = SUMUV + UV(I)
305  SUMUW = SUMUW + UW(I)
315  NEXT I
320  UP = (SUMUF/N) ^ 0.5
325  VP = (SUMVF/N) ^ 0.5
330  WP = (SUMWF/N) ^ 0.5
335  UVP = SUMUV/N
340  UWP = SUMUW/N
341  REM ** TO CALCULATE TAYLOR'S MICROSCALES
365  MSUMU = 0
370  MSUMV = 0
375  MSUMW = 0
380  FOR I = 1 TO N - 1
400  MSUMU = MSUMU + (UF(I+1) - UF(I)) ^ 2
405  MSUMV = MSUMV + (VF(I+1) - VF(I)) ^ 2
410  MSUMW = MSUMW + (WF(I+1) - WF(I)) ^ 2
430  NEXT I
450  MU = MSUMU/((DELT ^ 2) * (N-1))
455  MV = MSUMV/((DELT ^ 2) * (N-1))
460  MW = MSUMW/((DELT ^ 2) * (N-1))
465  LU = UBAR * ((UP ^ 2)/MU) ^ 0.5
470  LV = UBAR * ((VP ^ 2)/MV) ^ 0.5
475  LW = UBAR * ((WP ^ 2)/MW) ^ 0.5
495  PRINT UBAR; :PRINT VBAR;:PRINT WBAR
500  PRINT UP; :PRINT VP;:PRINT WP
505  PRINT UVP; :PRINT UWP
515  PRINT LU; :PRINT LV;:PRINT LW
525  END

```